

COMPACT NONLINEAR OPTICAL
DEVICES IN SILICON-POLYMER HYBRID
MATERIAL SYSTEM

Thesis by
Guangxi Wang

In Partial Fulfillment of the Requirements
for the Degree of
Doctor of Philosophy

CALIFORNIA INSTITUTE OF TECHNOLOGY

Pasadena, California

2009

(Defended September 15, 2008)

© 2009

Guangxi Wang

All Rights Reserved

To my parents,

Meiqin Yu and Yawen Wang

ACKNOWLEDGEMENTS

My years at Caltech as a graduate student have been an important part of my life, during which I was taught the essence of scientific investigation and given the opportunity to explore both the intriguing physical world and the limit of myself. For much of this, I owe tremendous gratitude to my advisor Professor Axel Scherer, who has been a great academic and personal mentor to me. None of this work and my course of study would have been possible without his patient guidance and unreserved support. I simply cannot thank him enough for all this.

I would like to extend my sincere appreciation to two former group members, Professor Michael Hochberg and Dr. Tom Baehr-Jones for their longtime collaboration and generous help to me. It was an honor and a pleasure to work with passionate and talented scientists like them. I would also like to acknowledge all members of the nanofabrication group, especially Chris Walker, Mike Shearn, and Jingqing Huang, for helping in lab, carrying insightful discussions, and above all offering supportive friendships.

My heartfelt thankfulness also goes to all professors and teachers who have taught or guided me here at Caltech and in the past, particularly, to my undergraduate advisor Professor William Jemison and other professors at Lafayette College, who kindly helped me in defining my path when I first set foot in this country.

Finally, I would like to thank my parents, my fiancée Wen Li, and all other family members, for their unconditional and everlasting support to me and for them being with me through happiness and difficulty. They are my greatest treasure in life.

ABSTRACT

Recently, integrated silicon photonics has become a topic of rising interests, due to its great potential to induce significant improvements in modern communication and computation systems. While optics is often viewed as a favorable solution to many issues faced by the rapidly evolving microelectronic technology, the high cost, large physical size, and discrete configuration of conventional optics have largely restricted its applications. The introduction of silicon nanophotonics permits a new look at the idea of incorporating optics with traditional electronic integrated circuits in a sensible and feasible fashion.

In this dissertation, emphasis is placed on investigating nonlinear devices built in silicon but complemented by nonlinear polymer materials. Basic optical guiding and coupling components for silicon on insulator platform are first discussed, followed by a detailed description of the design, fabrication, and testing procedures of a Pockels effect electro-optic modulator based on nonlinear polymer-coated silicon nanostructures. Discussion is further expanded on other related devices that also make use of the second-order nonlinear effect, and designs to improve the speed and efficiency of existing devices are also elaborated. Finally, a third-order nonlinear all-optical modulation device is presented with a series of carefully designed experiments to verify its ultrafast operation.

TABLE OF CONTENTS

Acknowledgements	iv
Abstract	v
Table of Contents.....	vi
List of Figures and Tables	viii
Nomenclature.....	xvi
Chapter 1. Introduction.....	1
1.1 Background.....	1
1.2 Layout of the Dissertation.....	3
Chapter 2. Basic Concepts and Components	4
2.1 Material and Fabrication	4
2.2 Light Guiding	8
2.3 Light Coupling and Testing	12
Chapter 3. Second-order Nonlinear Slotted Ring Modulator.....	17
3.1 Nonlinear Optics.....	17
3.2 Optical Modulation.....	19
3.3 Slotted Silicon Waveguides	21
3.4 Electrical Contacting	24
3.5 Slotted Ring-based Optical Modulator	27
3.6 Testing and Data of Slotted Ring Modulator.....	37
Chapter 4. Other Second-order Nonlinear Devices	43
4.1 Optical Rectification Detector	43

4.2 Testing and Verification of Optical Rectification	46
4.3 ROADM Device.....	55
4.4 Segmented and Slotted Waveguides for Improved EO Performance..	61
Chapter 5. Third-order Nonlinear All-optical Modulator.....	73
5.1 Third-order Nonlinear Optics.....	73
5.2 Four-wave Mixing.....	75
5.3 Ultrafast All-optical Modulator	76
5.4 Testing and Data of All-optical Modulator	79
Bibliography	88

LIST OF FIGURES AND TABLES

Figure 2.1. A layered diagram of a typical SOI substrate, with the top silicon device layer selectively etched. Note that the figure is not drawn to scale.	5
Figure 2.2. Micrograph of an electron beam patterned and chlorine plasma etched device showing a curved silicon waveguide resting on an oxide base.....	8
Figure 2.3. Mode pattern and dispersion curve of a simple PMMA clad single mode ridge waveguide on SOI substrate. The mode is plotted with 10% $ E $ contour.	9
Figure 2.4. Micrograph of a ring resonator coupled to a straight ridge waveguide.....	10
Figure 2.5. Transmission spectrum of a typical waveguide coupled ring resonator showing a single resonance peak with Q factor over 160 k.....	11
Figure 2.6. Three-dimensional illustration of the optical probing process using out-of-plane fibers to couple to devices on SOI chip.....	13
Figure 2.7. Photos of the semiautomated optical/electrical probing setup in operation showing cameras, illuminators, electrical probes, and attached measurement equipments.....	14
Figure 2.8. Layout of a focusing grating coupler showing two light paths that are designed to match in phase.....	15

- Figure 3.1. Profile of a mostly in-plane polarized mode plotted with 10% contour of $|E|$ on the left panel and dispersion curve of this waveguide on the right panel..... 22
- Figure 3.2. The left panel shows a top down view of the coupling region between a straight slotted waveguide and a slotted ring resonator on SOI substrate; the right panel shows an angled view of the ring resonator with visible undercut enhancement. ... 23
- Figure 3.3. Mode conversion structure from a regular ridge waveguide to a slotted waveguide. Periodic gaps are built in to keep the two arms of the slotted waveguide electrically well-isolated..... 24
- Figure 3.4. Monte Carlo simulation results using SRIM 2008 showing the case when phosphorus ions are implanted into an SOI target with a 110 nm thick top active silicon layer at 30 keV energy and 0° incidence angle..... 25
- Figure 3.5. Ring resonator Q factors and resistivity values when doped with different implant dosages, which indicate optical losses and electrical losses in silicon..... 26
- Figure 3.6. Electrical contacts of a slotted ring resonator, where contact leads are purposefully extended out in the same direction to avoid the inside of the ring..... 27
- Figure 3.7. Typical resonance peak of a silicon ring modulator near optical C-band. 28
- Figure 3.8. Zoomed-out view of slotted ring modulator structure showing optical input and output, as well as electrical contacts on the two opposite sides..... 29

- Figure 3.9. SEM images of nonlinear polymer-coated silicon nanoslots. The top two panels show the FIB cut, and the bottom panel shows a close-up view of uniformly filled nanoslot..... 32
- Figure 3.10. Overview of a complete slotted ring modulator device showing labeled electrical pads and on-chip shunt resistor..... 33
- Figure 3.11. Typical poling current curve, measured off a 140 nm slotted device coated in dendrimer-based polymer. The device is poled at 88 °C and 10 V approximating the ideal poling field of 70 V/ μm for this material, while the breakdown field strength is about 100 V/ μm 35
- Figure 3.12. Polymer-coated rings in a column routed to a single set of buses, which allows them to be poled simultaneously and tested individually later. This set of devices is contacted at two points from one side of the ring only. 36
- Figure 3.13. Resonance shifting in the best performing dendrimer-based polymer-coated device showing $\sim 0.042 \pm 0.008$ nm/V of tuning. The device is poled at +10 V and biased at +7 and -7 V with the outer ring considered as positive. 38
- Figure 3.14. YLD/APC-coated sample showing linearly increasing tuning and FWHM (full width at half maximum) tuning with +15 V of electrical bias. The device is poled at 125 °C and +18 V for 15 minutes..... 39

- Figure 3.15. Typical low speed 1 kHz AC results of slotted ring modulator showing the yellow optical trace closely following driving signal. This device is coated with YLD/APC polymer, poled at 15 V, and has a 140 μm gap. 40
- Figure 3.16. AC test results of a slotted ring modulator at 6 MHz showing 13 dB of modulation extinction in the yellow optical trace. This device is coated with YLD/APC polymer, poled at 15 V, and has a 140 μm gap. 41
- Figure 4.1: Equivalent circuit diagram of a slotted ring modulator device exhibiting optical rectification and serving as a virtual DC voltage source that can be measured at the terminals originally used for driving the modulator..... 45
- Figure 4.2. Panel A and B show transmission spectrums of two detector devices. Panel C shows photocurrent vs. optical power for three separate measurements: series 1 is for device 1 with 1549.26 nm on-resonance input, series 2 is for device 1 with 1550.5 nm off-resonance input, and series 3 is for device 2 with 1551.3 nm on-resonance input. Panel D shows output photocurrent as a function of wavelength, overlaid with rescaled transmission spectrum showing resonance peaks. 52
- Figure 4.3. Layout of a typical ring resonator-based 1 \times 4 \times 1 ROADM with ports colored and labeled..... 56
- Figure 4.4. Layout of top and bottom electrodes, which are used to both pole polymers at high voltage and tune individual rings during ROADM operation. 57

- Figure 4.5. Linear responses of a $1 \times 4 \times 1$ ROADM coated in YL124/APC. The top curves are for individual add-drop rings, and the bottom curve is the total bus response, all measured without any tuning voltage. 58
- Figure 4.6. Tuning responses of a typical $1 \times 4 \times 1$ ROADM device coated in YL124/APC and built with a $3 \mu\text{m}$ electrode gap. The top graph shows ring number 4 being tuned with $\pm 300 \text{ V}$, and the bottom graph shows corresponding bus responses. The dotted lines drawn between the two graphs illustrate how a wavelength channel can be added or dropped. 59
- Figure 4.7. Resonance shift performance of add-drop rings from three separate ROADM devices showing linear tuning characteristics. All devices were coated with YL124/APC and poled at 210 V across a $3 \mu\text{m}$ electrode separation. 60
- Figure 4.8. Simplified diagram of slotted MZM signal arm geometry showing a single pair of electrical contacts. 62
- Figure 4.9. Diagram of a slotted MZM in polymer-silicon hybrid implementation. The green metal pads are contacting the modulation arm at a single point, while the reference arm is unaffected. Nanoslots and optical couplers are not shown for simplicity. 63
- Figure 4.10. Color rendered modal pattern of a conventional slotted waveguide with 120 nm of gap near 1550 nm . The mode is plotted with 10% contour of $|E|$ assuming 1 W of average power flow. 64

- Figure 4.11. Panel (a) shows the propagation of a mode at 1550 nm in design 1, plotted in contours of 10% in E_x assuming 1 W of average power flow. Panel (b) shows the cross-sectional modal pattern in design 1, plotted with contours of 10% in $|E|$ assuming 1 W of average power flow. Panel (c) shows the dispersion curves of the two segmented slotted designs compared with a normal slotted design. 66
- Figure 4.12. Variation of device and coupler performance (in dB/cm and dB) due to different electron beam dosages used during fabrication..... 67
- Figure 4.13. Failure modes of some segmented slotted designs and fabrication variations. The left panel shows a narrow 70 nm gap not fully etched through, and the right panel shows an overexposed sample with broken side leads..... 68
- Figure 4.14. Panel (a) shows typical normalized insertion losses of segmented slotted waveguides in comparison with a short nonslotted loop. The longest device is 8000 μm , which corresponds to more than 30,000 contact pairs. Panels (b) and (c) are SEM micrographs of a segmented slotted waveguide from different angles..... 70
- Figure 4.15. Simplified diagram of segmented slotted MZM signal arm geometry showing small parallel RC units. 71
- Figure 4.16. Diagram of a segmented slotted MZM in polymer-silicon hybrid implementation. The green metal pads are contacting the modulation arm at multiple points over a large span. Nanoslots and optical couplers are not shown for simplicity. 72

- Figure 5.1. Panel A shows the operating diagram of a traveling wave MZM that introduces phase shifting in the signal path by the Kerr effect. Panel B shows a microscope photo of the actual device overlaid with port and flow labels. Panel C shows the mode pattern of polymer clad silicon waveguides used in 10% power contours. ... 77
- Figure 5.2. The left panel shows a typical spooled waveguide MZM, and the right panel shows an enlarged view of a 50/50 directional coupler. 78
- Figure 5.3. Transmission spectrum of a typical unbalanced Mach-Zehnder interferometer characterized by intrinsic phase shifts that vary with wavelength..... 79
- Figure 5.4. Logical diagram of the gigahertz modulation experiment..... 81
- Figure 5.5. Panel A shows positive and negative results of measuring optical modulation transfer with optical S parameters. Panel B and C show the spectral contents of modulator outputs at various gigahertz-range modulation frequencies..... 82
- Figure 5.6. Logical diagram of the terahertz modulation experiment..... 83
- Figure 5.7. Panel A and B show the spectral contents of modulator outputs when it is driven by 2.6 and 0.6 THz difference frequency inputs. Panel C shows the output spectrums of the modulator driven by a 0.25 THz difference frequency input and three different source frequencies. The resulting modulation peaks maintain a constant level. 85

Figure 5.8. Top-down and three-dimensional diagrams illustrating the operation of an all-optical modulator at speeds from 60 GHz to 2.4 THz. The slight ripples and falloffs at high frequencies are due to efficiency changes in fiber amplifiers and couplers. 86

Table 4.1. Room temperature repoling results showing the dependence of steady state photocurrent on repoling biases applied to a slotted device. The device is first poled at 110 °C and -12 V.....47

Table 4.2. Thermally cycled poling and repoling results of five different devices. Measurements are in sequential time order down the list, and the only anomaly happens when the second device is thermally cycled and tested repeatedly.....49

Table 4.3. Segmented slotted waveguide designs with measured losses and estimated speed limits for 1 cm structures listed.....66

NOMENCLATURE

dB/dBo decibel/optical decibel

SOI silicon on insulator

BOX buried oxide

rpm revolutions per minute

IPA isopropyl alcohol

MIBK methyl isobutyl ketone

PMMA polymethylmethacrylate

ICP-RIE inductively coupled plasma ion reactive ion etching

SEM scanning electron microscope

PM fiber polarization maintaining fiber

TE mode transverse electric mode

EO electro-optic

Gbps gigabit (10^9 bit) per second, a measure of digital signal transmission rate

sccm standard cubic centimeters per minute, a measure of volumetric flow rate

APC amorphous polycarbonate (Poly[Bisphenol A carbonate-co-4,4'-(3,3,5-trimethylcyclohexylidene)diphenol carbonate])

FWHM full width at half maximum

Q factor quality factor

DC direct current

AC alternating current

RF radio frequency

ROADM reconfigurable optical add-drop multiplexer

WDM wavelength division multiplexing

MZM Mach-Zehnder modulator

FWM four-wave mixing

EDFA erbium doped fiber amplifier

CW continuous wave

VNA vector network analyzer

OSA optical spectrum analyzer

Chapter 1

INTRODUCTION

1.1 Background

As modern electronics is being constantly pushed forward on the frontiers of computation and communication, there have been many rising interests in the recent years to search for an alternative way to accommodate the fast growing needs for bandwidth and speed. Specifically, integrated optics has been viewed as a potential candidate that could solve some issues faced by traditional electronics. While long distance communication and the internet backbone have been dominated by fiber optics for many years, the privilege of going optical is rare to find in other levels of application. In addition to high material cost, one of the biggest hurdles present is the lack of integration and the resulting high cost in assembly and packaging. The advent of silicon photonics seems to provide an answer to all this. Traditionally an unfavorable optical material, silicon is certainly overall the most studied and most widely used semiconductor material. Given the readily available advanced fabrication techniques nowadays, it is possible to fabricate nanoscale subwavelength optical structures from silicon, which is a relatively easy to handle and inexpensive material to begin with. The prospect of integrating optics onto familiar low-cost silicon platforms compatible with existing CMOS (complimentary metal-oxide-semiconductor) technology has been powering much of the interest from academic researchers [1] as well as industry pioneers such as Intel and Luxtera [2-4].

In order to construct a useful system based on the silicon material platform, as it has been pointed out in an early review article [5], multiple building blocks have to be realized with satisfactory performance, ranging from signal guiding and encoding to signal generation and detection. The realization of these function blocks often involves nonlinear physical processes, such as the Pockels and Kerr effects. In the world of free space optics, these nonlinear effects are usually observed by means of using high-power pulsed laser sources and bulk nonlinear media. Conventional nonlinear photonic devices used in industry typically employ expensive nonlinear crystal materials, are generally bulky in size, require a significant amount of power to operate, and suffer from laborious and low yield assembly processes. Provided that nonlinear materials can be properly integrated and light signals can be efficiently coupled in and out, the idea of building as many nanoscale components as possible on a single silicon wafer implies higher modal confinement, stronger nonlinear interaction, lower power requirement, less wafer estate, easier packaging, and hence better performance at lower cost overall.

While integrated silicon photonics is still a relatively new territory, miles away from wide industrial deployment, many progresses have been made in various directions using different techniques and assisting nonlinear materials. Most devices and investigations in this dissertation are based on special nonlinear polymers that demonstrate large nonlinear coefficients, low optical losses, and ultrafast responses. Previously, these special polymers have been used as core material for building optical devices both in academic research and industry [6, 7]. Approaches described in this dissertation focus on utilizing the properties of a unique silicon-polymer hybrid material system, which has many inherent advantages over other alternatives, most notably, compactness and field

enhancement. Results presented here and published depict a promising future of using special polymers (or any suitable nonlinear material) in conjunction with common silicon nanostructures to realize critical functional components in optical communication and computation systems.

1.2 Layout of the Dissertation

This dissertation summarizes my work in the past four years on a number of projects related to building and testing nanoscale nonlinear optical devices, which are aimed to contribute to the overall initiative of realizing affordable integrated optical system as introduced in the previous section.

Chapter 2 details the process of designing, fabricating, and measuring basic optical components, such as waveguides, couplers, and ring resonators. Chapter 3 explains the basics of nonlinear optics and describes a silicon electro-optic modulation device utilizing electrically functionalized slotted waveguides and second-order nonlinear polymers. Chapter 4 describes the same modulator structure used for optical rectification based detection, followed by other related applications such as a reconfigurable wavelength filter, and finally proposes and investigates segmented structures that can help improve the performance of second-order nonlinear devices in this category. Chapter 5 introduces an all-optical Mach-Zehnder device that achieves terahertz intensity modulation utilizing third order nonlinear polymer materials. Some images and figures presented are courtesy of Axel Scherer, Tom Baehr-Jones, and Michael Hochberg.

BASIC CONCEPTS AND COMPONENTS**2.1 Material and Fabrication**

Traditionally silicon has been the material of choice for electronics. Until fairly recently it has not been considered as a good candidate for applications related to light wave generation and manipulation, most predominantly optical communication, a playground of more exotic compound materials such as gallium arsenide and indium phosphide. While silicon does not readily emit light and does not exhibit strong nonlinear optical effects, there are a few merits of the material that makes it both possible and rewarding to build optical structures in this material system. First of all, it is an inexpensive and readily available commercial material; tools and infrastructure developed around it have existed for a long time. Silicon is also known to be transparent for short-wavelength infrared, which conveniently covers the most important C-band for long-distance telecommunication [8].

Silicon bulk wafer and its more specialized variants such as SOI (silicon on insulator) and SOS (silicon on sapphire) are widely used nowadays to build electronic devices. Particularly SOI, since its debut in 1998 by IBM targeted for low-power applications [9], has become a standard platform for high-performance electronics. A typical SOI substrate with bonded top layers is shown in Figure 2.1.

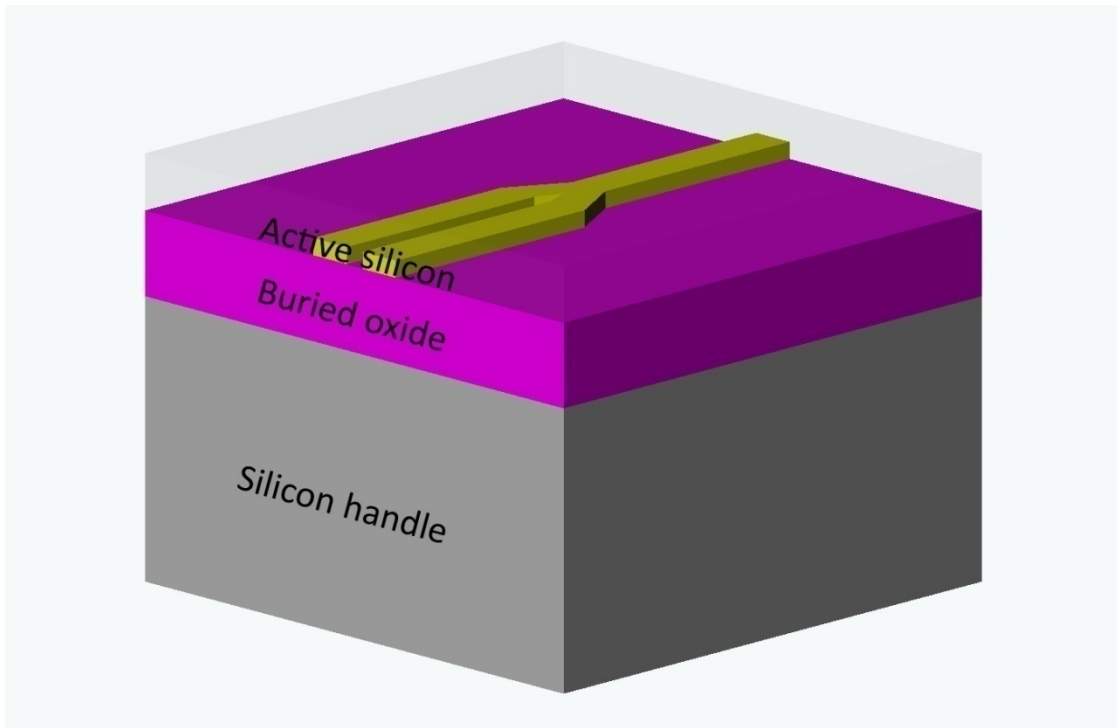


Figure 2.1. A layered diagram of a typical SOI substrate, with the top silicon device layer selectively etched. Note that the figure is not drawn to scale.

We noted that the SOI substrate has several favorable properties that make it highly suitable for building integrated photonic devices. The buried oxide layer works as a good etch stop layer, making a simple single layer fabrication process possible. Silicon dioxide is also a low optical loss and low refractive index material with a typical index of 1.46, which forms a favorable high index contrast structure with the top silicon layer. Since most polymer materials used for top cladding (shown in translucent color in Figure 2.1) have indices of refraction around 1.5, the oxide underneath is usually able to provide good index symmetry as well. Finally, the buried oxide layer works well to provide optical and electrical insulation, in that it not only prevents optical mode leakage to the silicon handle,

but it also serves as a good lateral insulating medium for in-plane structures in the active silicon layer on top.

A set of relatively straightforward lab processes were established and improved over time for fabricating optical devices on SOI substrates. In a typical workflow, we usually start with a 4-inch or 6-inch diameter commercial SOI wafer (Soitec Group, Bernin, France) that has a BOX (buried oxide) of 1.35 μm and a lightly p-doped top active silicon layer of 110 nm in thickness. Often the desired thin top layer is not directly available, in which case an additional step of controlled dry furnace oxidation and wet etch thinning is needed. Spectral ellipsometry can be used to verify the active layer thickness and uniformity after oxidation thinning. It is also later discovered that a thicker BOX of 3 μm can often help improve the loss characteristics of many structures and devices to be detailed in this dissertation. The SOI wafers used are of $\langle 100 \rangle$ crystal orientation and can be easily cleaved into square pieces for processing. Each chip is spin cleaned at high rotation speed (typically 4000 to 5000 rpm, revolutions per minute) with acetone and IPA (isopropyl alcohol). The chip needs to be baked thoroughly at 180 $^{\circ}\text{C}$ for over 20 minutes to be fully dehydrated, and then a special flowable oxide electron-beam resist XR-1541 made by Dow Corning (Midland, MI) with 2% solid content dissolved in MIBK (methyl isobutyl ketone) solution is spun on. Comparing with the more common PMMA (polymethylmethacrylate) resist, this HSQ (hydrogen silsesquioxane) resin resist is a negative resist (hardens where exposed) and has better etching selectivity in chlorine plasma, which works well for designs with low surface fill factor. The rather diluted resist is applied with low spin speed of 1000 rpm to form a 300 nm layer, and then prebaked for 20 minutes. The resist prepared chip is then pattern exposed with a Leica EBPG-5000+ 100 kV electron beam writer (Leica

Microsystems, Wetzlar, Germany). The dosage is carefully calibrated and optimized for each wafer used, and generally varies between 2500 and 3500 $\mu\text{C}/\text{cm}^2$. The exposed sample is developed in an AZ MIF-300 TMAH (tetramethylammonium hydroxide) solution for 3 minutes, and rinsed off with deionized water and isopropanol. The followed etching process is carried out with an Oxford Instruments (Oxfordshire, UK) PlasmaLab 180 ICP-RIE (ion coupled plasma reactive ion etcher), using a chlorine-based recipe: 12mTorr of chamber pressure, 800 W of ICP power and 50 W of forward RF power, for 33 seconds. More recently fluorine-based etching tools have become accessible, and the use of those can potentially further improve the etching quality and allow the use of resists that have better ultimate resolution such as PMMA. Figure 2.2 below shows the end result of an etched sample.

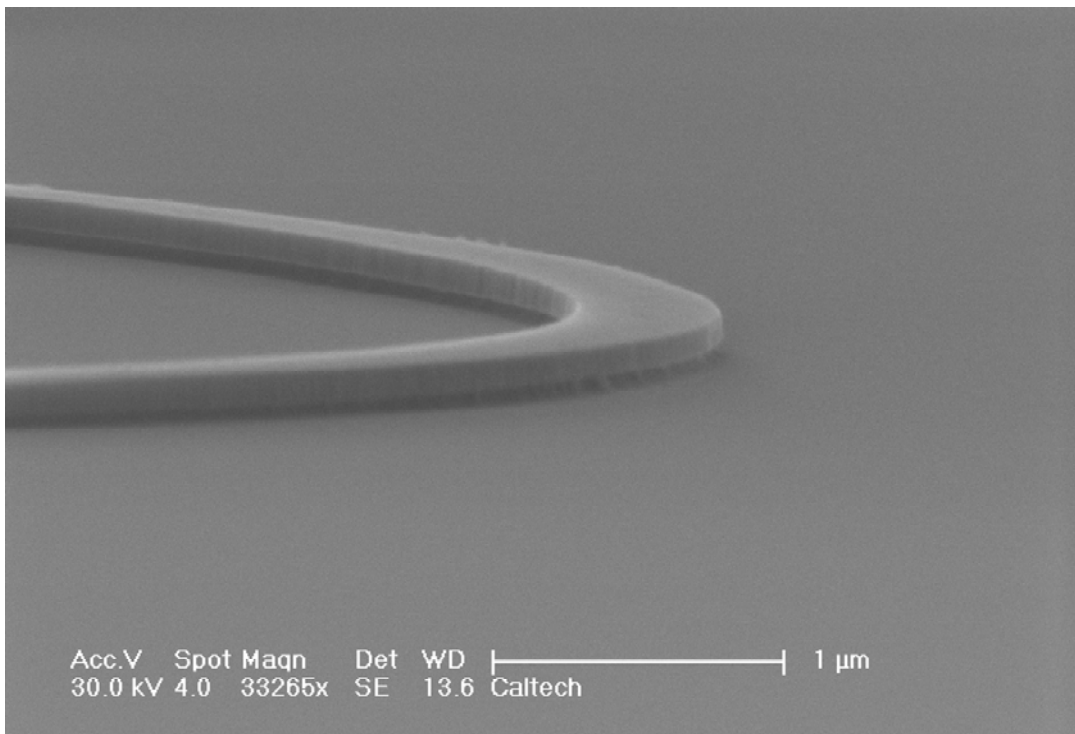


Figure 2.2. Micrograph of an electron beam patterned and chlorine plasma etched device showing a curved silicon waveguide resting on an oxide base.

In addition, a quick several second buffered HF (hydrofluoric acid) dip can effectively remove the remnant oxide resist, and a slightly longer dip can create observable undercutting as one can see from the shadows in Figure 2.2 above.

2.2 Light Guiding

With the selected substrate and established fabrication process in the previous section, a simple ridge waveguide can be defined by etching a strip of silicon that is 110 nm in height and laterally measures about 500 nm [10]. This waveguide has a mode profile as shown in Figure 2.3 below, with about 1/3 of optical power residing in the cladding region, and this overlapping ratio can be increased further by waveguide undercutting as mentioned in the previous section. It is a critical feature of this design that allows the effective index for the propagating mode to be easily modified by changes in the cladding region, a concept that is central to most devices that will be introduced in this dissertation. When clad with PMMA, the waveguide has an effective index of about 1.8, with fairly low dispersion. It is a single mode waveguide, and the supported mode near 1550 nm is primarily E_x polarized (in plane and normal to the direction of propagation).

One can predict even by assuming a simple plane wave propagating in a small confined region as in equation (2.1) that the peak electric field strength is going to be high in these structures. And indeed the simulation shows that field peaks exist at the edges and

corners of the structure, about 3×10^6 V/m for a 1 mW propagating power. The high field intensity at the interface and the mode overlap with the cladding make the structure more subjected to scattering loss due to surface roughness and surface state absorption. This problem can be mediated with better lithography and etching, as well as surface passivation techniques [11]. The best loss achieved with these waveguides is as low as -2.8 dB/cm.

$$I = \frac{1}{2} E \times H = \frac{|E|^2}{2\eta} \quad (2.1)$$

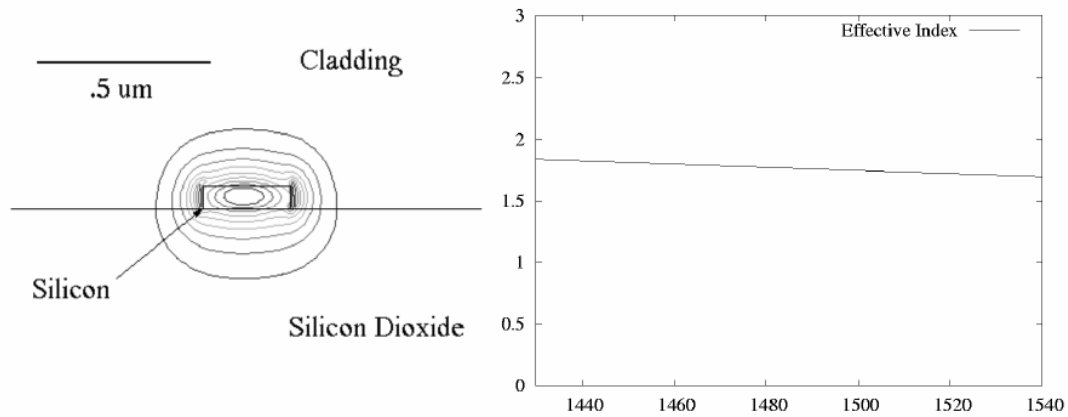


Figure 2.3. Mode pattern and dispersion curve of a simple PMMA clad single mode ridge waveguide on SOI substrate. The mode is plotted with 10% $|E|$ contour.

A simple and important device that can be made out of ridge waveguides is a circular-shaped optical ring resonator, usually coupled to a straight waveguide as shown in Figure 2.4. The mechanism and math of a waveguide resonator and its coupling are well understood [12, 13]; light propagating down the straight waveguide couples into the ring

resonator and transmission dips are formed in a spectrum sweep measurement as shown in Figure 2.5.

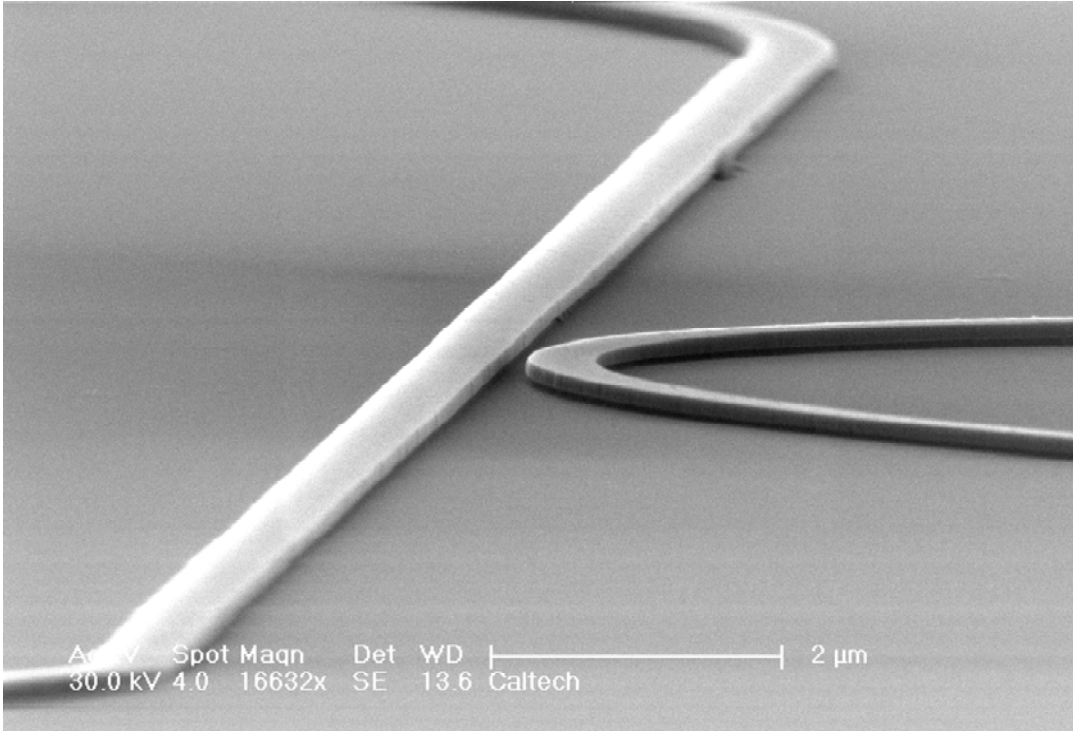


Figure 2.4. Micrograph of a ring resonator coupled to a straight ridge waveguide.

The resonator structure is not only interesting by itself, but it also provides a useful means to measure the waveguide loss figure. This method of loss measurement is superior in two aspects: first, the small sizes of the rings with low loss bend radius of $40\ \mu\text{m}$ makes it easy to build many characterization resonators and to statistically find the best Q factor (quality factor) for calculating waveguide loss, and second, a smaller footprint implies less chance for a device measurement to be skewed by fabrication defects. The Q factor of a waveguide coupled ring resonator can be express as in equation (2.2) below, where L is the circumference of the ring, α is the optical loss per traversal of the ring, and t is the

attenuation ratio at the waveguide coupling region. Note that the effective index of the waveguide is expressed in a form that takes waveguide dispersion into consideration, necessary for calculating high Q resonators in particular.

$$Q = \frac{\pi L n_{eff}}{\lambda_0 (1 - \alpha t)} = \frac{\pi L \left(n_0 - \lambda_0 \left(\frac{\partial n}{\partial \lambda} \right)_0 \right)}{\lambda_0 (1 - \alpha t)} \quad (2.2)$$

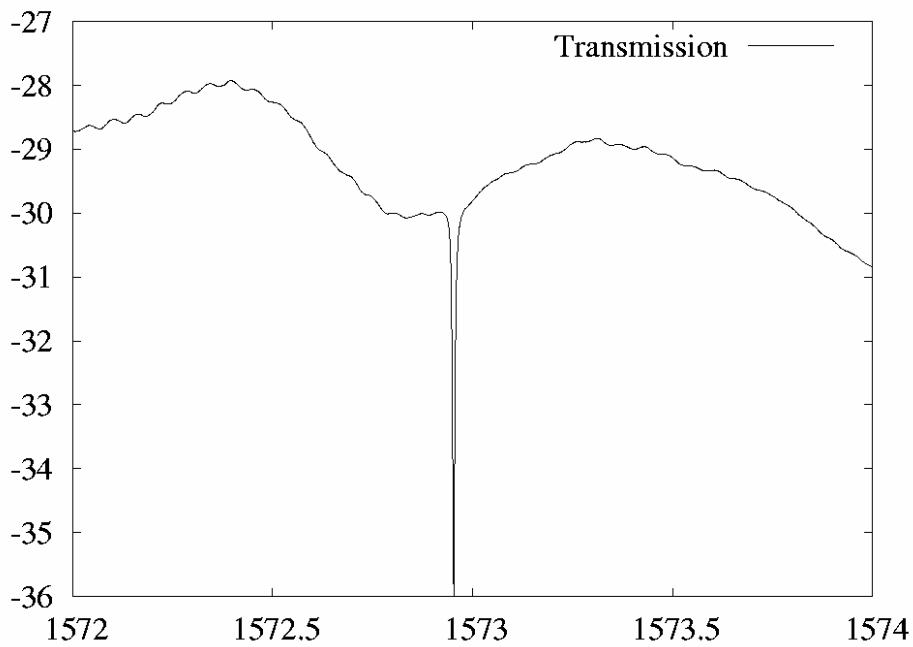


Figure 2.5. Transmission spectrum of a typical waveguide coupled ring resonator showing a single resonance peak with Q factor over 160 k.

2.3 Light Coupling and Testing

In modern communication systems, optical fibers have been steadily replacing copper wires as the main medium of signal transmission. Unlike electrical circuitry however, where a simple physical metal connection can often serve the purpose of conducting direct electrical currents quite efficiently, a major concern for integrated optical devices is to be able to couple light wave in and out of chip in an easy and low-loss fashion. Traditional ways of such coupling usually involve building tapering structures on the edge of a chip and physically lining up fiber ends to those structures [14]. While on-chip waveguides are on the order of several hundred nm in size, typical multimode fibers have core dimensions of 50 or 62.5 μm , and even for single-mode fibers that are regularly used in experimental settings, the core dimensions are typically around 8 to 10 μm . Due to this large disparity in mode sizes, these couplers are often tricky to fabricate and low in power efficiency. With some edge-coupling methods [15], many problems can be alleviated, but their convenience is still vastly compromised by the need to perform laborious manual alignments.

A more advantageous solution to this coupling problem is to use scattering gratings for out-of-plane coupling. It has been shown that with proper grating designs, low loss vertical coupling is achievable [16-18]. While good alignment is also required in this case for the couplers to work, the fact that the SOI wafers have highly uniform vertical profile facilitates the implementation of an automated process. With the assistance of a commercially available two-dimensional Aerotech linear motor stage (Aerotech,

Pittsburgh, PA) and a motorized vertical arm, we are able to perform alignment to individual coupler pairs in the fashion that is shown in Figure 2.6 below.

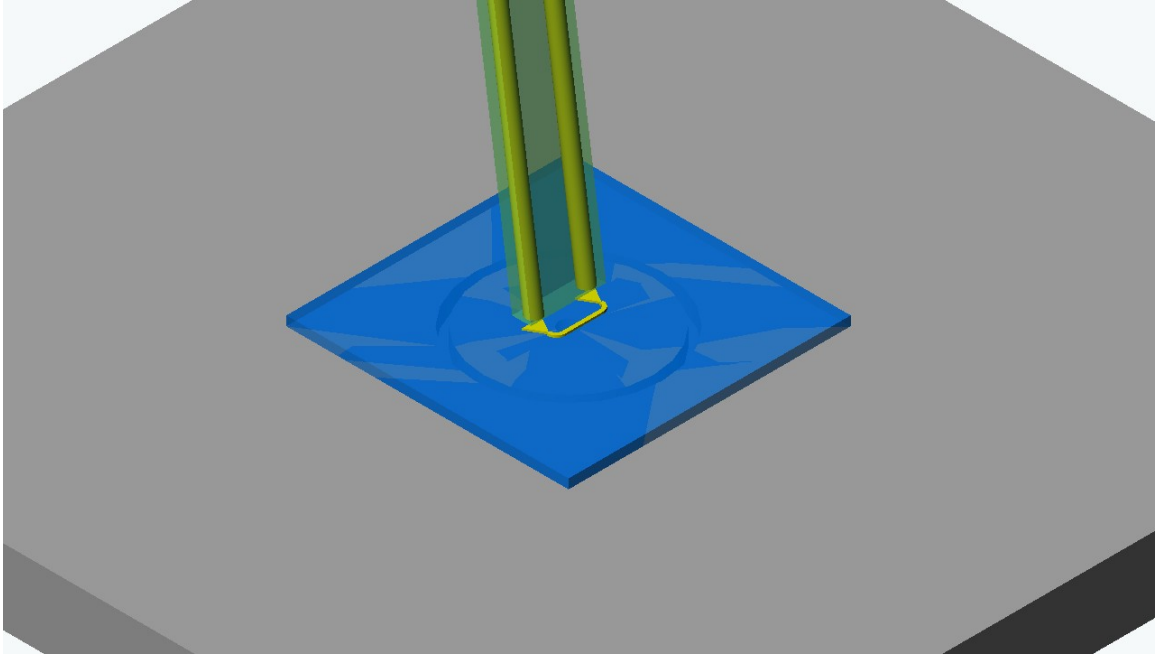


Figure 2.6. Three-dimensional illustration of the optical probing process using out-of-plane fibers to couple to devices on SOI chip.

In each case, light is coupled into the structure under test through one single-mode PM fiber and coupled out from another, where both fibers are mounted between crystal substrates with proper polarization and accurate predetermined pitch. A typical optical test consists of a swept-frequency light transmission measurement with a C-band centered tunable laser and power sensor system (e.g. Agilent 8164A). This allows a signal feedback loop to form, and using the aforementioned testing setup, it is possible to implement a semiautomated alignment by having a computer perform hill-climbing search for the local maximum. Extending this idea, whenever there is a chip holding a large number of devices

each equipped with a coupler pair, we can achieve alignment on several devices, which provides enough information to create a unique mapping between stage coordinates and chip layout. The following testing process becomes totally effortless, where the computer is able to locate each device, perform fine alignment, and record transmission data in a fully automated fashion.

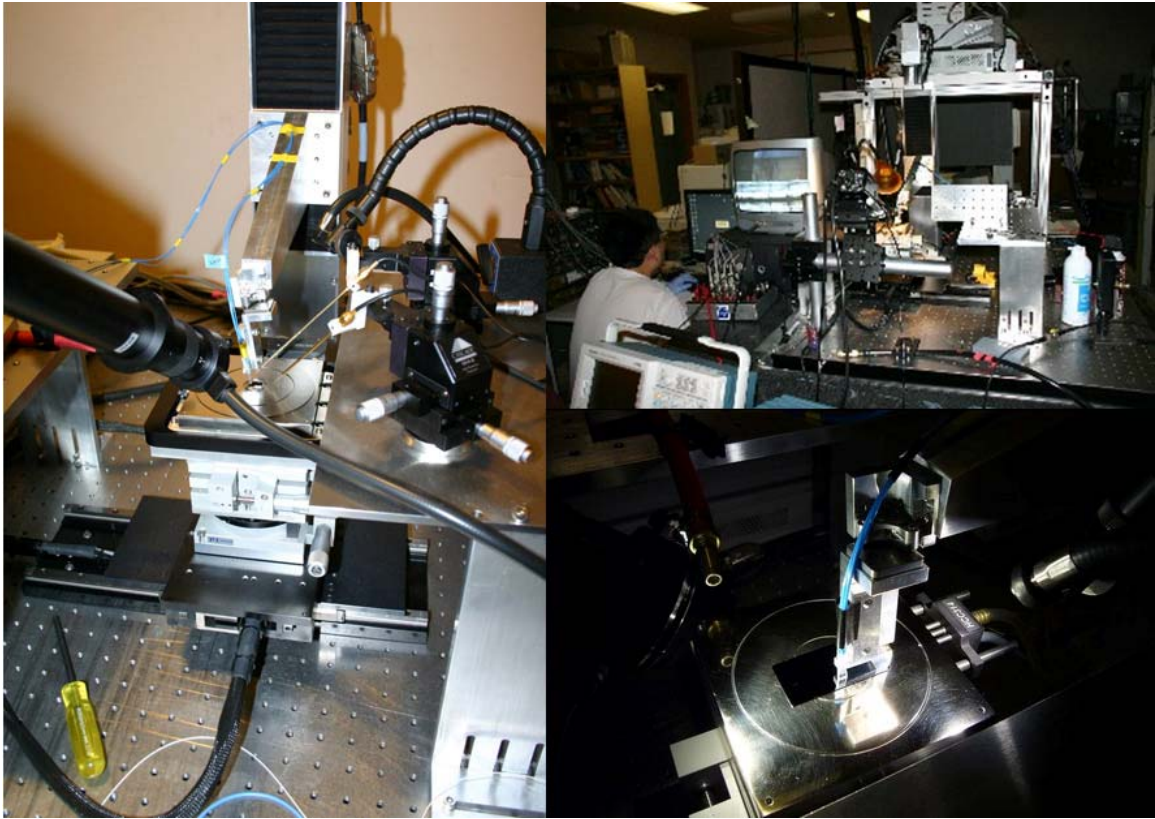


Figure 2.7. Photos of the semiautomated optical/electrical probing setup in operation showing cameras, illuminators, electrical probes, and attached measurement equipments.

A few different designs of out-of-plane couplers have been proposed in the past [16-19]. Most of them involve structures of large size, embedded reflector, partially etched gratings, or varying grating periodicity. For our particular substrate of choice, the top

active silicon layer thickness is ideal for fully etched rectangular weak scattering gratings. To achieve better mode transition to in-plane waveguides and better near-field coupling to hovering fiber, 1-dimensional curvilinear focusing gratings are used. The curvature of the focusing lens can be to the first order approximated by simple wave front matching calculation as shown in Figure 2.8, equation (2.3), and equation (2.4) below.

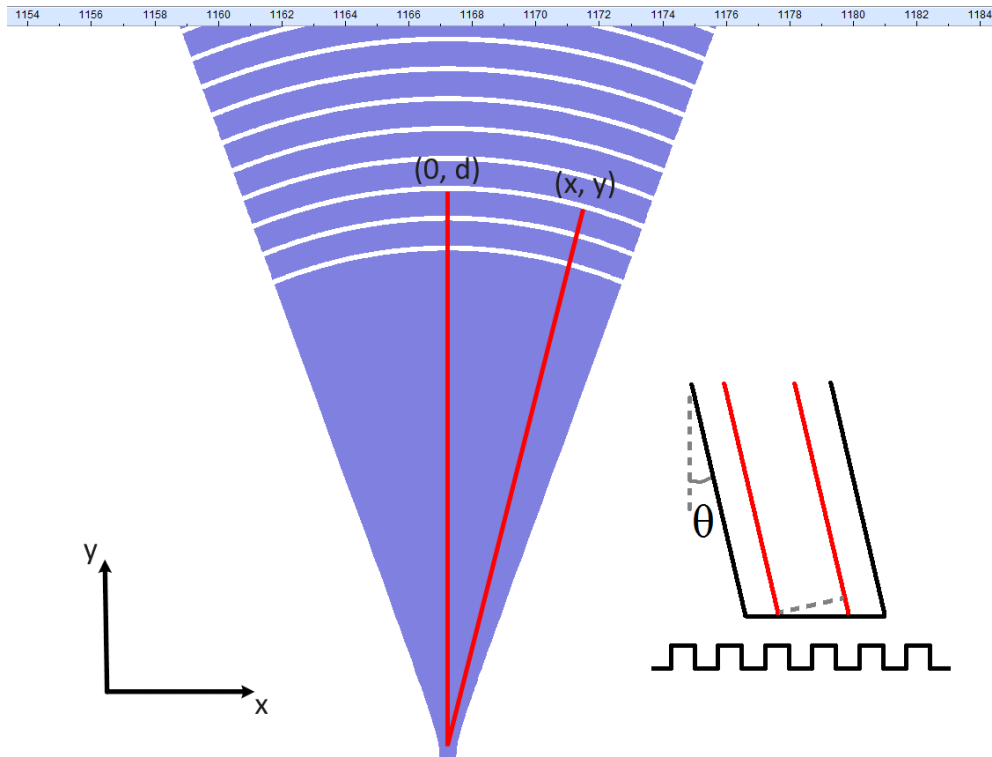


Figure 2.8. Layout of a focusing grating coupler showing two light paths that are designed to match in phase.

$$\Delta\Phi = \frac{2\pi}{\lambda} n_{fiber} \sin \theta (d - y) = \frac{2\pi}{\lambda} n_{eff} \left(d - \sqrt{x^2 + y^2} \right) \quad (2.3)$$

Here θ is the angle at which the fiber array is tilted and end polished, in this case 8 degrees is used to reduce fiber end face reflection. The in-plane distance from the tip of

coupler to the center point of a curved grate is represented by d , as shown in the figure above, and λ is the free space light source wavelength, which is C-band optical frequency around 1550 nm. The refractive index of out-of-plane coupling fibers is n_{fiber} , and n_{eff} is the effective index of the silicon-air grate structure. If a nudge factor $r = n_{fiber}/n_{eff}$ is introduced, then the equal phase condition above can be rewritten as the following:

$$\frac{x^2}{a_1^2} + \frac{(y - s_1)^2}{b_1^2} = 1 \quad \left(a_1 = \sqrt{\frac{1 - r \sin \theta}{1 + r \sin \theta}} d, b_1 = \frac{d}{1 + r \sin \theta}, s_1 = \frac{r \sin \theta d}{1 + r \sin \theta} \right) \quad (2.4)$$

Experimentally, each device wafer used can be calibrated by making a coupler farm chip that sweeps a few nudge parameters. Making use of the automated test procedure, it is quite effortless to empirically optimize the performance of these structures, and typical achievable loss figures are around -4 dB (40% efficiency), which is comparable to most published designs.

SECOND-ORDER NONLINEAR SLOTTED RING MODULATORS

3.1 Nonlinear Optics

Nonlinear optics is a very broad term; it can be used to describe many types of nonlinear process that take place in the optical domain. These nonlinear phenomena may include laser interaction, multiphoton absorption, nonlinear scattering, optical solitons, and parametric interactions. Particularly, parametric interactions are defined as nonlinear phenomena that occur in passive nonlinear medium, where no energy exchange exists with the light waves [20].

In electrostatics, the electric flux density (also called electric displacement) is a medium independent vector quantity that describes the electric field present, and it is defined as $D = \varepsilon E$, where E is the electric field intensity and ε is the dielectric permittivity [21]. This relationship can also be further rewritten in different forms as shown in equation (3.1) below, showing polarization P (C/m²), electric susceptibility χ_e , relative permittivity (also called dielectric constant) ε_r , and refractive index n .

$$D = \varepsilon E = \varepsilon_0 E + P = \varepsilon_0 E + \chi_e \varepsilon_0 E = \varepsilon_0 (1 + \chi_e) E = \varepsilon_0 \varepsilon_r E = \varepsilon_0 n^2 E \quad (3.1)$$

A dielectric medium is considered linear if the relation between the polarization and the electric field in it is linear, and nonlinear otherwise. For nonlinear media, polarization can be expressed in the form shown in equation (3.2), where χ^2 and χ^3 are second- and third-order nonlinear coefficients (typically tensor quantities), respectively [22].

$$P = \varepsilon_0 E (\chi + \chi^2 E + \chi^3 E^2 + \dots) \quad (3.2)$$

The second-order nonlinear effect is also called the linear electro-optic effect or the Pockels effect, where the change of refractive index is directly proportional to the applied electric field. The third order nonlinear effect is according named the quadratic electro-optic effect or the Kerr effect [20]. These effects can be more generally described by nonlinear susceptibility tensors to deal with anisotropic nonlinear media. In this case, the index ellipsoid is used to characterize the material, whose second-order form in the presence of an electric field is shown in equations (3.3) and (3.4) below.

$$\frac{x^2}{n_1^2(E)} + \frac{y^2}{n_2^2(E)} + \frac{z^2}{n_3^2(E)} + \frac{2yz}{n_4^2(E)} + \frac{2xz}{n_5^2(E)} + \frac{2xy}{n_6^2(E)} = 1 \quad (3.3)$$

$$\frac{1}{n_i^2(E)} - \frac{1}{n_i^2(0)} = \sum_{j=1}^3 r_{ij} E_j \quad (3.4)$$

In the above equations, E is the applied electric field with E_1, E_2, E_3 as components in x, y, and z directions, and the modified refractive indices in primary axes are notified as $n_i(E)$. A 3 by 6 matrix named r_{ij} is known as linear electro-optic coefficients, which is a standard way to characterize second-order nonlinear properties of materials, in the unit of pm/V. Concepts of these coefficients will be further explained and used through the rest of this chapter.

Parametric interactions bridge the gap between electrical signal and optical refractive index, providing the ground for building index-modulation devices. With

traditional free space optics, parametric interaction experiments are typically performed with high power pulsed laser sources and bulk size nonlinear media in order to produce measurable effects. In the context of integrated optics, however, there is the advantage of small physical sizes, and therefore allowing nonlinear effects to occur with much less total power requirement due to high local field intensity.

3.2 Optical Modulation

Optical modulators are fundamental components of optical data transmission systems and may be used to transduce electrical signals onto light waves [23], basically serving as the gateway from the electrical to the optical domain [24, 25]. A variety of physical effects are able to produce optical modulation [25], including the Pockels effect, acousto-optic effect [26], free-carrier plasma-dispersion [1], electroabsorption [27], and thermal modulation [28]. Among others, index modulation is one of the dominant ways to build optical intensity modulators. For a practical modulator that at least provides the potential to operate at high speed (>1 GHz), it must utilize mechanisms that are fast enough, most notably, such as free carrier dispersion and the Pockels effect.

It has been shown that free-carrier dispersion can rather effectively change the refractive index of silicon at a fast rate [29]. By injecting or depleting free carriers, the silicon index could vary by two orders of magnitude more than under other inducing effects like electroabsorption. Modulators based on this effect have been demonstrated to show performance of greater than 1 Gbps operation [30].

Another category of approach exploits nonlinearity not in semiconductors but in some special materials that exhibit the Pockels effect. Two common choices are nonlinear optical crystals, such as lithium niobate (LiNbO_3), and nonlinear electro-optic polymers. The former is frequently used in modulators for commercial telecommunication systems. Lithium niobate crystal shows a significant amount of nonlinearity with r_{33} of 30.8 pm/V [31], and it has been shown that modulators based on this technology are capable of achieving speeds over 10 Gbps or even 40 Gbps [32]. However, crystals are expensive and require special growing process, which drives the efforts of looking for other more flexible alternatives. Recently there has been considerable progress in the research of synthesizing engineered nonlinear polymer materials that show many favorable properties, notably ultrafast femtosecond responses [33-35]. Polymers with r_{33} values of 130 pm/V have been achieved [36], and our collaborators at the University of Washington have suggested the likelihood of going up to 500 pm/V or more, by far exceeding the state of the art. These polymers also have the potential of further improvement and cost reduction, as well as the advantages of being easy to deploy, none of which is true for traditional crystals.

Some early work in using nonlinear polymers to build modulators is from Steier and co-workers, where a large part of their multilayer devices is made with polymers, both the waveguide core and cladding, and electrodes are made with metal stood off from the optical structures [6, 37]. While these studies open up interesting path toward building polymer based devices, the limitations associated are obvious. Because of the low index contrast nature of these structures, their size and bending radius are restricted, and also the multilayer fabrication with different polymer chemistry could be difficult. The most

limiting factor here is the fundamental trade-off one has to make between optical losses and modulation efficiency. Here electric field intensity per unit of applied voltage is determined largely by the distance between the opposing electrodes. However, reduced distance of these metal structures from the optical paths in Steier's devices would mean decreased optical performance, and due to the large mode size in low contrast waveguide, the extreme field intensity achievable is limited.

Integrated silicon photonics, on the other hand, allows us to build compact high index contrast devices, which when properly designed and accompanied by nonlinear materials can concentrate both optical and electrical field to satisfy the requirement for a high-performance optical modulator.

3.3 Slotted Silicon Waveguides

The most straightforward method of integrating nonlinear polymers with silicon is to deploy them around waveguides as cladding. In a traditional silicon ridge waveguide such as the one described in the previous chapter, the propagating optical mode is reasonably well confined within silicon. The index change caused by cladding property shift in this case is present but limited, and the symmetric crystal structure of silicon prevents it from exhibiting a second order nonlinear effect. In order to efficiently utilize the nonlinear properties of organic material, the first step is to increase the overlapping of optical mode with the cladding. It has been shown that a simple modification to create a

void in regular ridge waveguide works well for the purpose of guiding light at reasonable loss and confining optical power in the void region [38, 39].

A typical slotted waveguide we fabricated has nominal dimensions of 300 nm in width by 110 nm in height in each arm, and the gap size varies anywhere from 70 nm to 150 nm (Figure 3.1 and Figure 3.2). This geometry greatly magnifies the electric field associated with the optical mode, resulting in peak electric fields in excess of 10^6 V/m for continuous-wave, sub-milliwatt optical signals [40]. While smaller gaps are favorable for producing higher electric field, fabrication becomes trickier and the sidewall quality tends to deteriorate as the gap shrinks. When clad with PMMA, we were able to achieve propagation loss figure of -10 dB/cm with a 1.35 μm thick underlying oxide layer, and high field intensity is established in the center void.

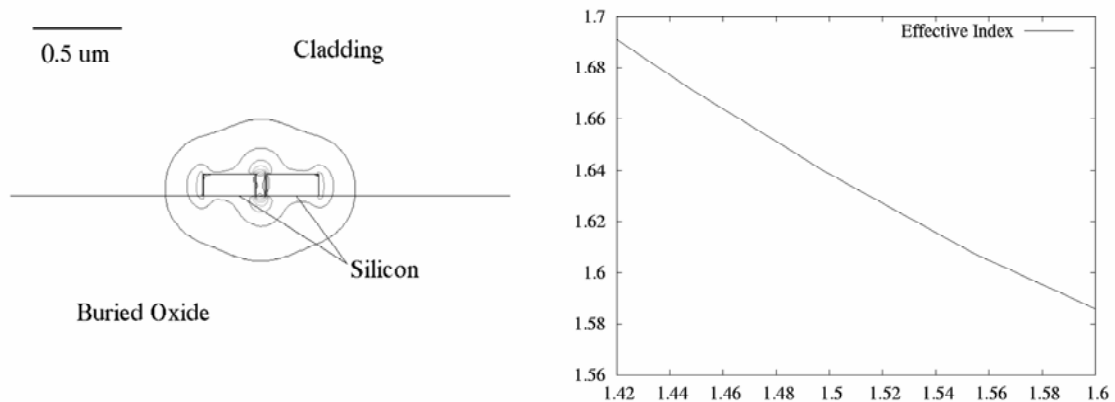


Figure 3.1. Profile of a mostly in-plane polarized mode plotted with 10% contour of $|E|$ on the left panel and dispersion curve of this waveguide on the right panel.

It is possible to construct similar optical structures with these slotted waveguides as is done with normal ridge waveguides. Micrograph of a slotted waveguide based ring resonator, for instance, is shown in Figure 3.2.

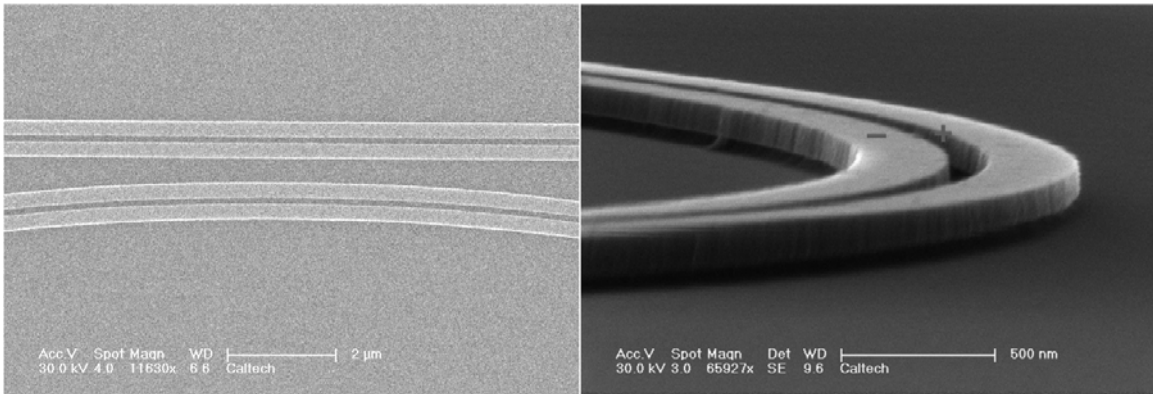


Figure 3.2. The left panel shows a top down view of the coupling region between a straight slotted waveguide and a slotted ring resonator on SOI substrate; the right panel shows an angled view of the ring resonator with visible undercut enhancement.

Coupling from normal ridge waveguides to slotted waveguides can be done efficiently with adiabatic tapering and Bloch mode like isolation gratings as shown in Figure 3.3. The loss introduced by this type of transition can be less than 0.5 dB. The reason why the complicity of gratings is involved is due to the need to electrically isolate the two arms of the slotted waveguide, whose necessity will be further explained in the following section on its electrical properties.

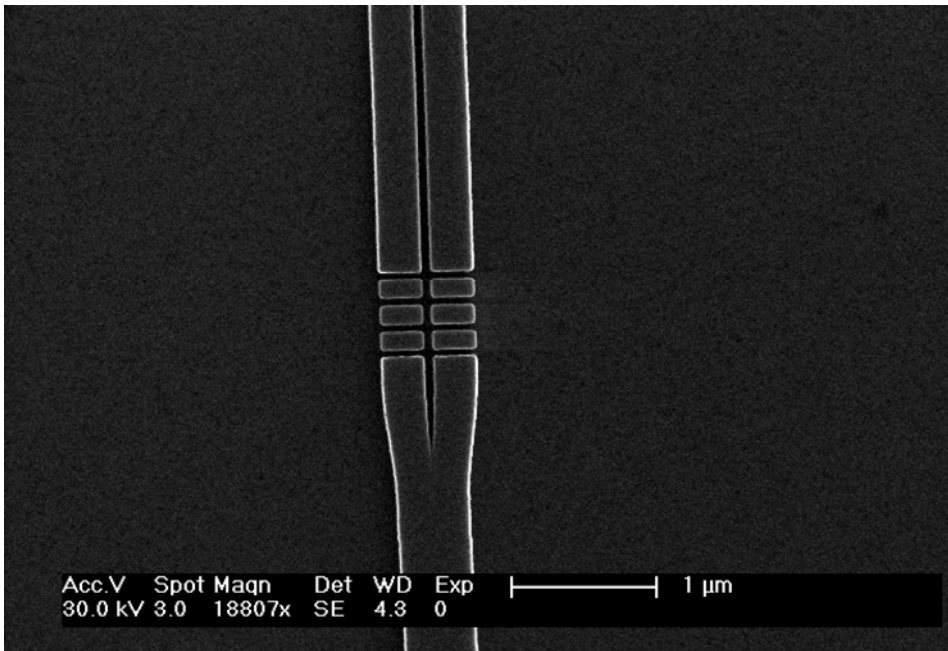


Figure 3.3. Mode conversion structure from a regular ridge waveguide to a slotted waveguide. Periodic gaps are built in to keep the two arms of the slotted waveguide electrically well-isolated.

3.4 Electrical Contacting

Intrinsic silicon has very high electrical resistivity ($\sim 4 \times 10^5 \Omega\text{-cm}$, and $\sim 15 \Omega\text{-cm}$ for typical lightly boron doped wafers), and thus unsuitable for conducting electrical signals. However, when heavily doped with p-type or n-type impurities, silicon can become very conductive. The downside of doing this is the optical loss can go up rather quickly due to free carrier absorption. We have found through careful experimentation and calibration, that certain dopants work better than others (e.g., phosphorus vs. boron), and there could be a range of doping density where a good balance is made between optical loss

and electrical loss. Take the SOI substrate described previously with a 110 nm thick top active silicon layer as an example: a Monte Carlo simulation can be performed using SRIM software to determine the optimal impurity implantation energy and depth. It is possible to estimate ion lateral spread and vertical distribution profile, which is roughly Gaussian, as shown in Figure 3.4 below.

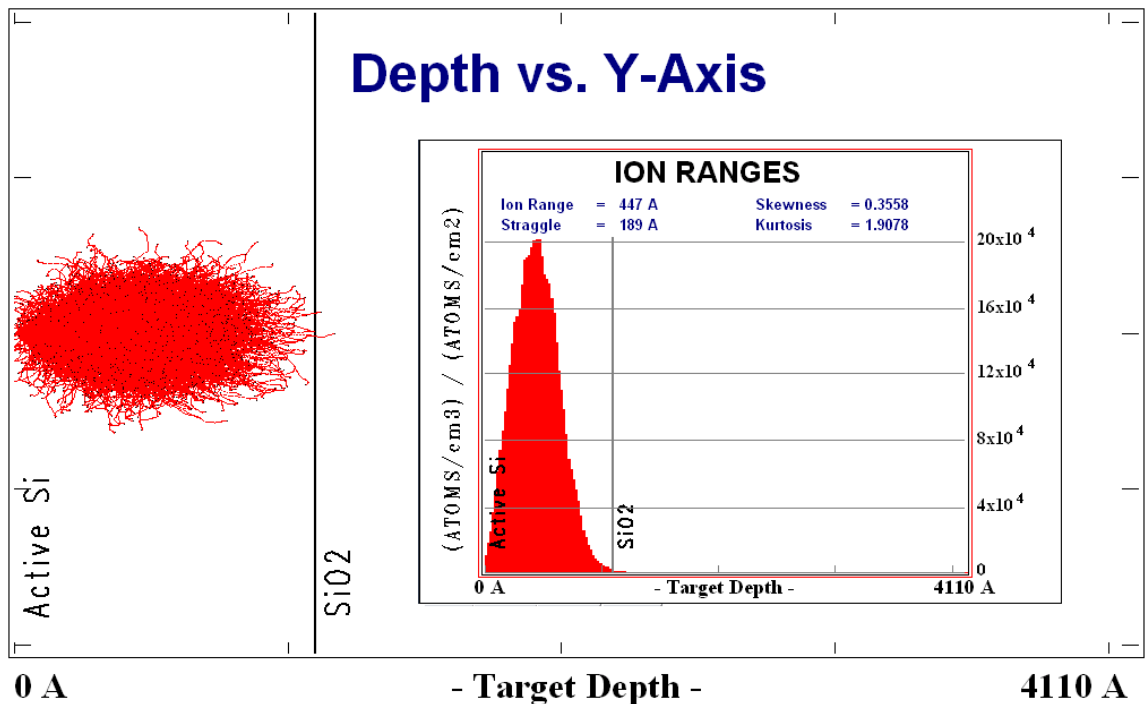


Figure 3.4. Monte Carlo simulation results using SRIM 2008 showing the case when phosphorus ions are implanted into an SOI target with a 110 nm thick top active silicon layer at 30 keV energy and 0° incidence angle.

Calibration dies are fabricated comprising both optical structures (waveguides and ring resonators) and electrical structures (resistor strips of different sizes with contact pads). These dies are then implanted with phosphorus at 30 keV, 0 degree incidence angle, and a variety of dosages, through commercial service. Testing has shown that when the

doping density is between 10^{13} atoms/cm² and 10^{14} atoms/cm² (i.e., 10^{18} atoms/cm³ and 10^{19} atoms/cm³), both electrical and optical characteristics of the silicon material become very usable (Figure 3.5).

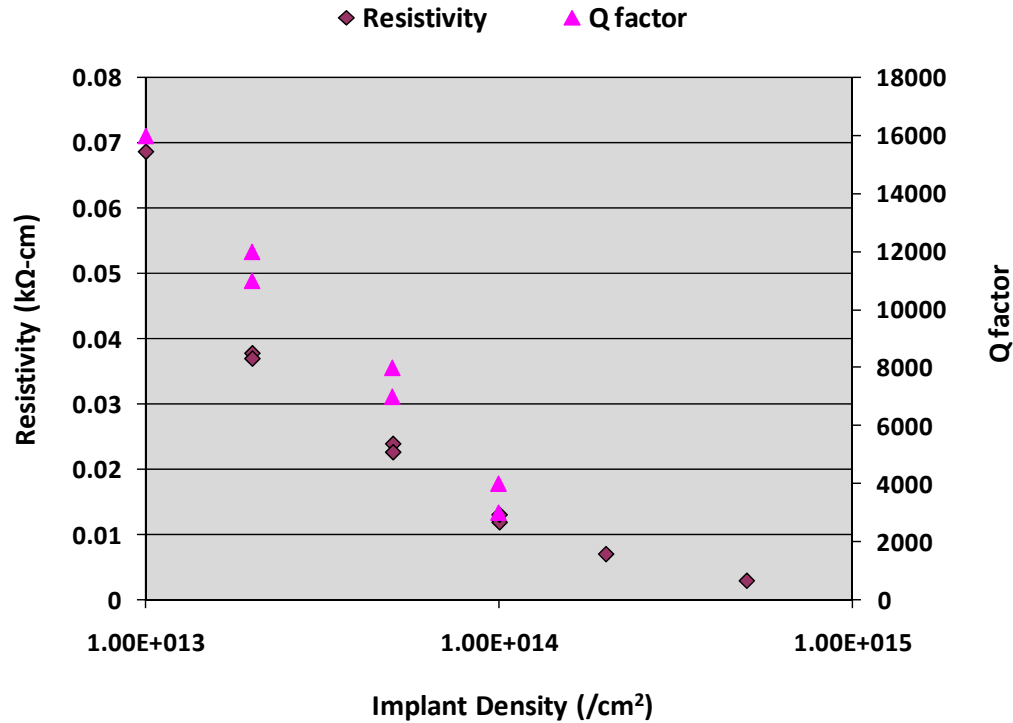


Figure 3.5. Ring resonator Q factors and resistivity values when doped with different implant dosages, which indicate optical losses and electrical losses in silicon.

This finding makes it possible to use the two arms of the slotted waveguide as conducting electrodes for setting up an electric potential difference across the narrow gap. Figure 3.6 shows how both sides of a slotted ring resonator can be contacted by building tiny contact fingers without introducing significant optical loss (~ 0.1 dB). The electric field established exists in a region where light wave energy propagates in silicon as well as

nonlinear cladding material. It should be noted that the field intensity in this case can be extremely high considering the low voltage potential that needs to be applied across the gap. Every 1 V of applied voltage will result in roughly 10^7 V/m of increase in electric field intensity in our typical slotted structure. The combination of confined optical power and close electrode proximity is desirable for exploiting nonlinear electro-optic interaction.

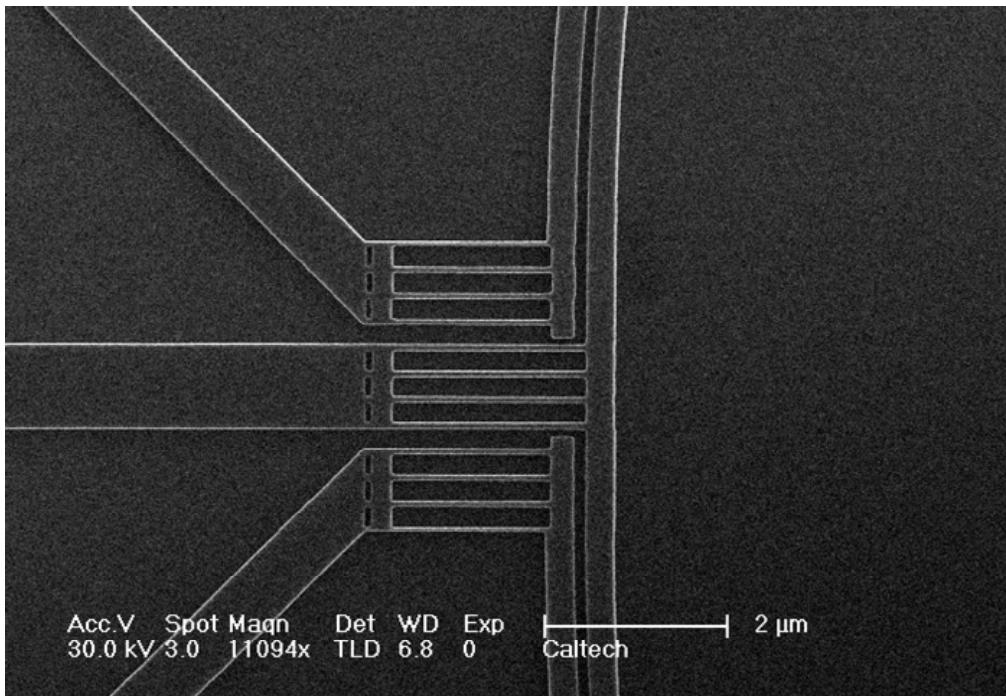


Figure 3.6. Electrical contacts of a slotted ring resonator, where contact leads are purposefully extended out in the same direction to avoid the inside of the ring.

3.5 Slotted Ring-based Optical Modulator

The previously investigated electrically activated slotted waveguide provides a path to readily incorporate nonlinear polymers for constructing optical modulators. A ring

resonator scheme is a good starting point, because its relatively short path length helps to keep both optical insertion loss and electrical capacitance under control, allowing the modulator to operate with low input optical power and at a reasonable modulation speed. Pockels effect induced index changes will result in resonance peak shifts, which can be readily exploited to create desired level shifts in output optical power. The concept of this idea is illustrated in Figure 3.7 below, in which a coherent light source is biased at a quasi-linear region to offer maximum extinction.

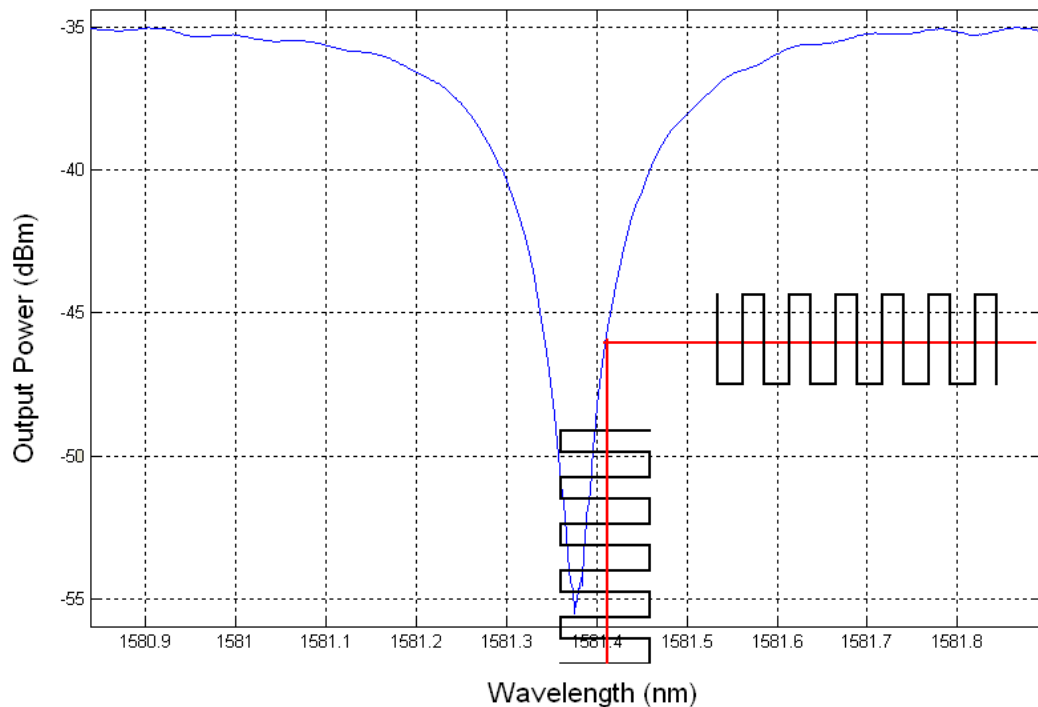


Figure 3.7. Typical resonance peak of a silicon ring modulator near optical C-band.

Below in Figure 3.8, an overall view of the modulator design is shown, where optical signal is coupled in with structures described in Section 2.3, and electrical signal is routed in with structures described in Section 3.4. On each side, three contacts are made as

shown in Figure 3.6, where the center ones are connected to the inner ring, and the ones on the sides are connected to the outer ring. A bit of redundancy is introduced here to produce symmetry, as well as to allow electrical debugging during testing.

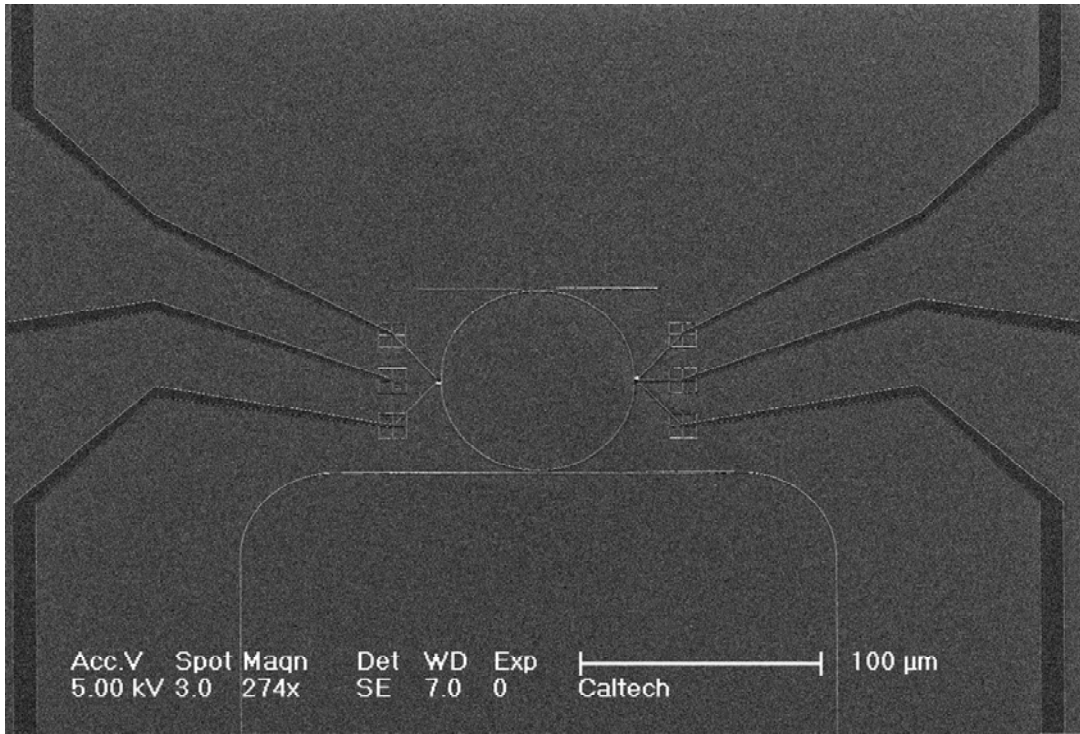


Figure 3.8. Zoomed-out view of slotted ring modulator structure showing optical input and output, as well as electrical contacts on the two opposite sides.

The fabrication process is similar to that described in Section 2.1, with the exception that the chips are sent to external service providers for phosphorous ion implantation after initial optical testing. The majority of devices fabricated are implanted at 30 keV, 0 degree incidence angle, and 10^{14} atoms/cm². The chips then have to be thermally annealed to repair the lattice damage introduced by the implanting process. A Jipelec Jetfast 150 rapid thermal annealer (Qualiflow Therm, Montpellier Cedex, France)

is used for this purpose. The annealer chamber is vacuum pumped and flushed with argon gas repeatedly for a few cycles, and then while filling the chamber with 200 sccm argon gas, the temperature is linearly ramped up to 950 °C in 15 seconds, held for 5 seconds, and cooled back down to room temperature in 30 seconds. The chips are dipped in buffered hydrofluoric acid briefly to remove surface oxide and remnant electron beam resist.

The final step involves coating the topside of the chips with nonlinear polymer material. The special polymers are designed and mostly prepared by members from Professor Larry Dalton and Professor Alex Jen's groups in the chemistry department at the University of Washington. Various types of polymers have been tested, including AJL 8, YLD 124, and dendrimer-based polymers. The design of these polymers are far from straightforward, since tweaking their structures even slightly can result in significant changes in both nonlinear strength and optical properties. Details about synthesizing and preparing these materials can be found in relevant chemistry publications [33-35, 41]. To facilitate easy deployment, further steps are needed to process the polymers. Taking one of the best-performing polymers YLD 124 as example, synthesized polymer needs to be mixed with a host polymer, typically APC (amorphous polycarbonate) with one-to-three weight ratio, and the mixture is dissolved in solvents such as cyclopentanone [40]. Since our primary deploying method is with simple nonpressurized spin-coating, the choice of solvent and solid content ratio are critical tuning factors. Solvents tend to have different surface-wetting properties, and various solid loading factors directly impact the optical properties. A 12% loading factor is used for a well-performing YLD 124 sample tested. The solution is cleansed once more with 0.2 μm filters, and then spin coated in a cleanroom environment at moderate spin speed (2000~4000 rpm typically) to produce a thin film

cladding that is roughly 2~3 μm thick. The coated chips need to be vacuum baked at roughly 80 °C for more than 10 hours to fully exhaust the solvent.

One potential issue that deserves careful investigation is how well the silicon nanoslots are filled by coated polymer, because the proposed nonlinear function of slotted waveguides is based on the assumption that both the optical mode and the applied electric field overlap well with the polymer. Any bubbling and nonuniformity will likely cause deteriorated nonlinear performance and optical loss. A direct visual proof can be obtained by using an FEI dual beam FIB (focused ion beam system), with which we can conveniently cut through a sample device and image the cross section of nanoslots as shown in Figure 3.9 below.

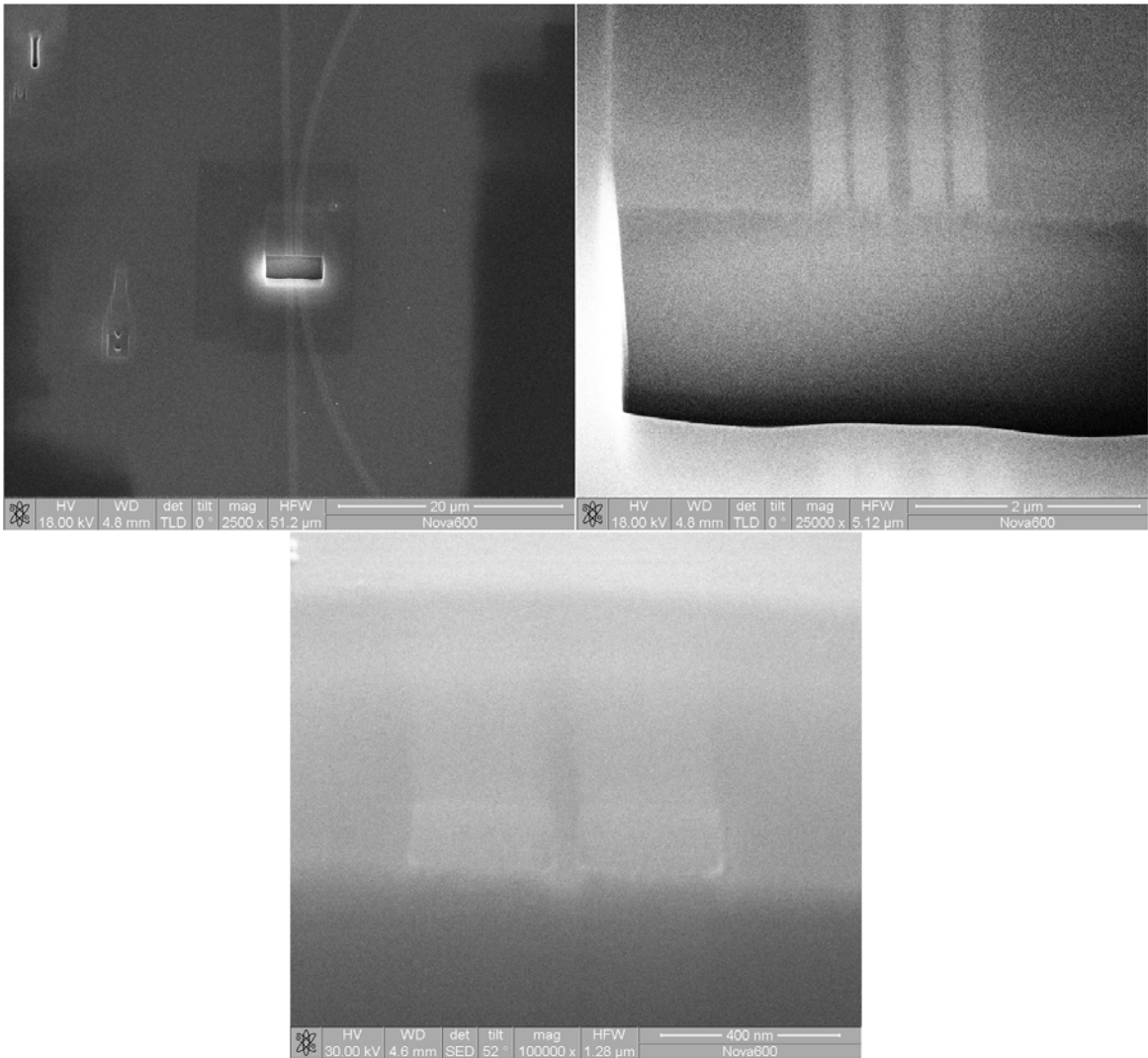


Figure 3.9. SEM images of nonlinear polymer-coated silicon nanoslots. The top two panels show the FIB cut, and the bottom panel shows a close-up view of uniformly filled nanoslot.

The entire device with electrical pads is shown in Figure 3.10. As we can see from below, two pads are connected to the inside and outside rings respectively, and there is also a shunt resistor of roughly 200 k Ω resistance connected between the positive and negative terminals. The purpose of this shunt resistor is to help verify contact quality during testing

with electrical probes, and it also helps to detect possible shorting in the slotted ring, since the inside ring is supposedly well isolated from the outside one.

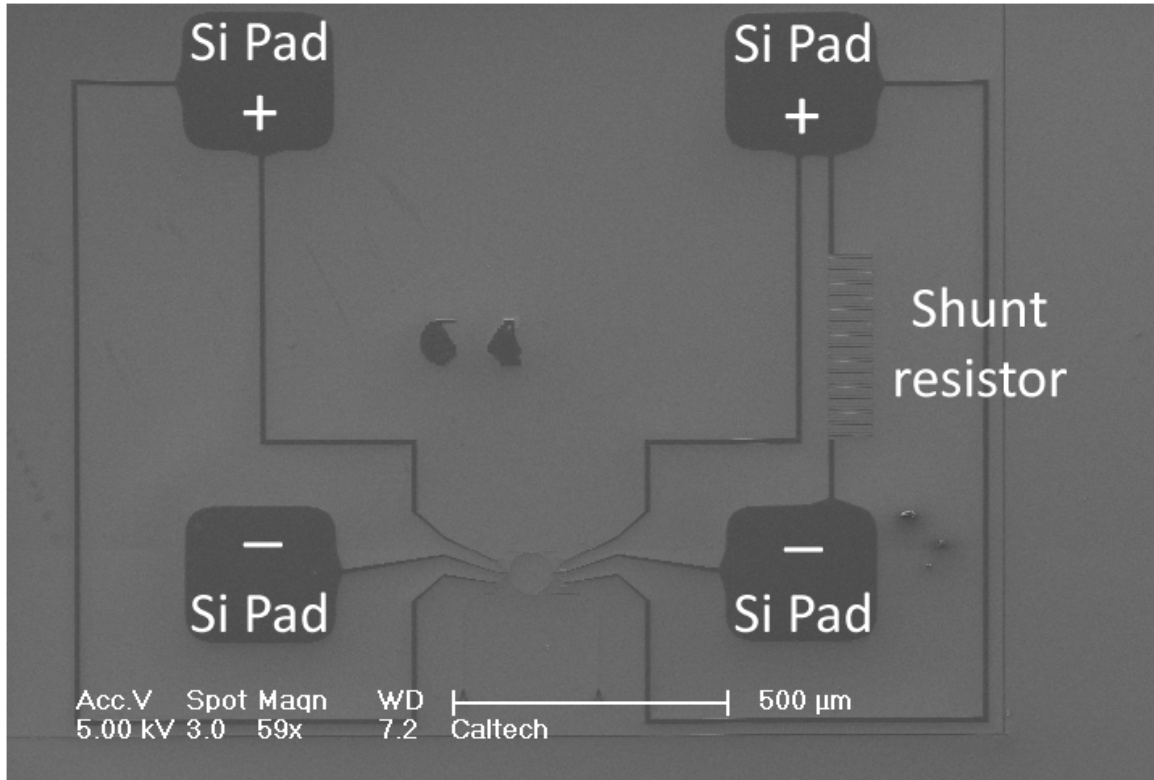


Figure 3.10. Overview of a complete slotted ring modulator device showing labeled electrical pads and on-chip shunt resistor.

Before starting the testing procedure, the polymer inside of the nanoslots must be electrically poled. A poling step is required because we are dealing with linear electro-optic effect, where the index change is proportional to the electric field applied. Therefore, the initially randomly pointing polymer molecules need to be reoriented to an orderly fashion to demonstrate macroscopic nonlinearity. This process of reorienting these NLO (nonlinear optical) chromophores is known as poling, and is often achieved with the assistance of an external poling electric field. Our design of slotted waveguide

conveniently makes in situ poling possible, and the same electrical connections for supplying modulation signals later in the experiment can be used here. A typical poling recipe will consist of the following stages:

1. A slow heat up stage, where the temperature is gradually raised (~ 10 °C/min) to slightly over the glass transition temperature of the polymer (110~125 °C).
2. A voltage ramping stage, where the applied voltage across two opposite waveguide arms is raised at intervals of 0.1 V while closely monitoring the leakage current increase.
3. A 10-minute-long holding stage once the voltage has reached the suggested optimal value or leakage current starts to exhibit sign of runaway (between 7 and 15 V in our structures, but the actual poling strength is usually on the conservative side due to voltage dropping along the resistive electrical path). Figure 3.11 includes more details about typical poling strength.
4. Finally a cool down stage, where the temperature is relatively quickly lowered while still maintain the maximum poling voltage, hence “freezing in” the chromophore orientation. After the chip is fully cooled down to less than 10 °C above room temperature, the voltage can be quickly dialed down, and that completes a full poling cycle that typically lasts 30 minutes in total.

The entire poling process should be ideally carried on with the chip in vacuum or immersed in inert gas such as nitrogen to prevent oxidation or other kinds of chemical degradation. Photobleaching and oxidation are to be avoided when storing these polymers, and in experimental settings we have found that no obvious degradation occurs over a

period of a few weeks when samples are largely preserved in low vacuum and retrieved for testing in nitrogen occasionally.

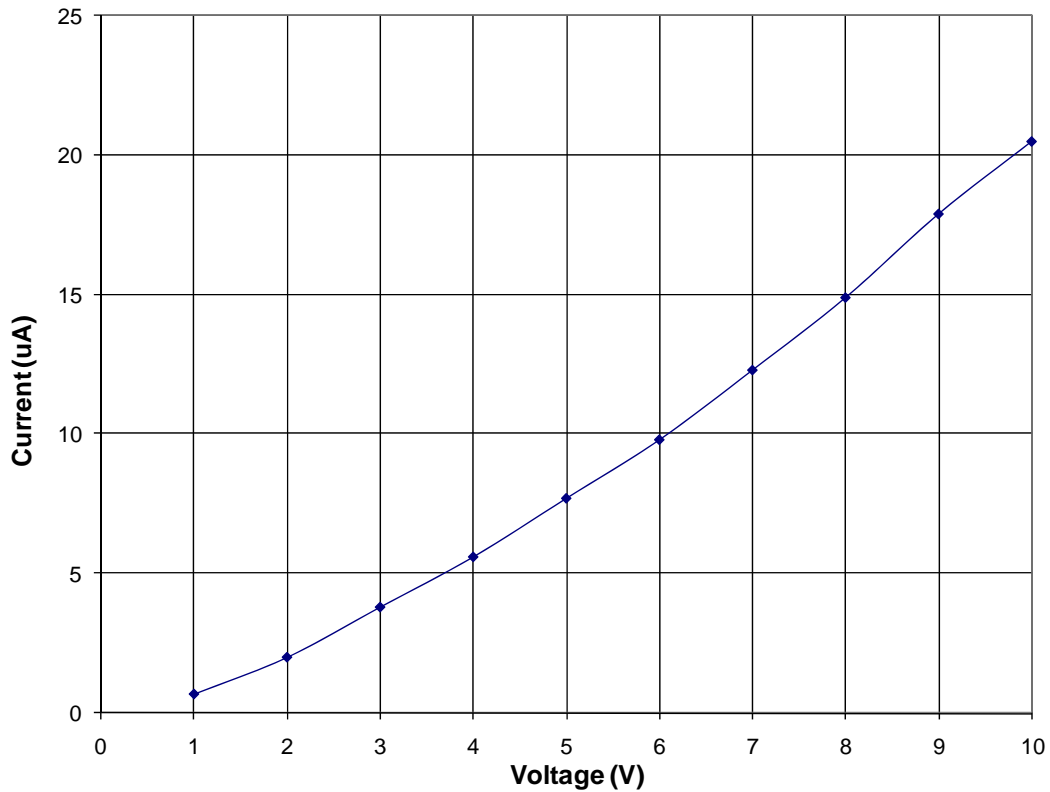


Figure 3.11. Typical poling current curve, measured off a 140 nm slotted device coated in dendrimer-based polymer. The device is poled at 88 °C and 10 V approximating the ideal poling field of 70 V/ μm for this material, while the breakdown field strength is about 100 V/ μm .

While on-chip polymer poling is by no means a quick and straightforward process, once a working recipe is established, a bus design can be utilized to batch accelerate this job as shown in Figure 3.12 below. Due to the nontrivial resistance in common electrical paths, this poling scheme is generally not compromised by individual nonworking ring

devices, such as broken or shorted slotted ring resonators, except that poling current monitoring might become inaccurate in the presence of badly shorted slotted rings.

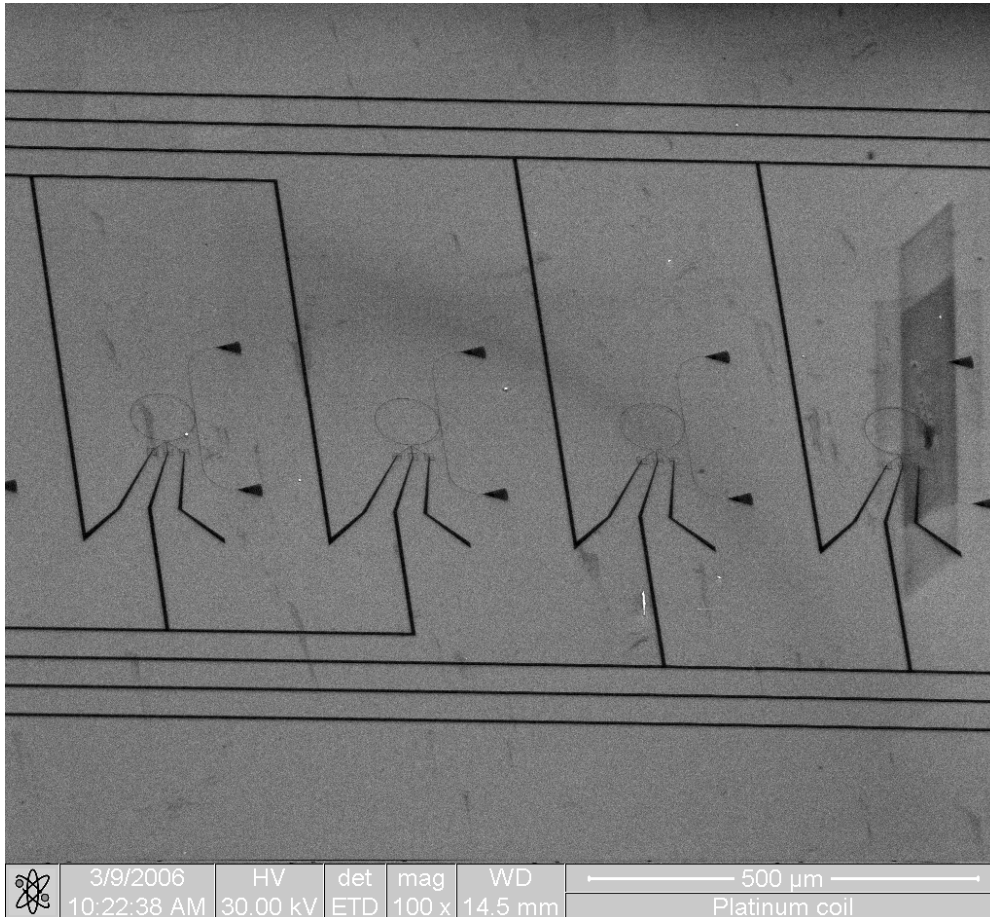


Figure 3.12. Polymer-coated rings in a column routed to a single set of buses, which allows them to be poled simultaneously and tested individually later. This set of devices is contacted at two points from one side of the ring only.

3.6 Testing and Data of Slotted Ring Modulator

The testing procedure itself is straightforward: devices are optically aligned to fibers as stated in Section 2.3, while electrical probes are secured in contact with on-chip silicon pads, and both frequency-domain and time-domain measurements are then taken with different electrical pumping.

In the case of DC tests, an optical wavelength sweep is taken first without electrical bias to record all resonance peaks of the slotted ring resonator. Then, a set of positive or negative (with respect to the poling polarity) DC biases of different magnitudes are applied to the device, and an optical wavelength sweep is taken at each bias. These scan traces are then overlaid on a single graph to find resonance peak shifts, as shown in Figure 3.13 and Figure 3.14. An important measure to quantify modulation effect is the amount of shifting per volt of applied voltage in the frequency domain, and in this case the best result achieves about 0.042 nm/V, or 5.2 GHz/V, which corresponds to a material r_{33} of 22 pm/V. This number was, at the time of publication [40], the best known result, representing a more than 6-fold improvement over the 0.8 GHz/V result previously reported in all polymer materials [6]. Many data points are often taken in random time sequences over a lengthy period, to obtain a statistically meaningful number with two-dimensional linear regression that rules out any possible thermally induced time varying drift.

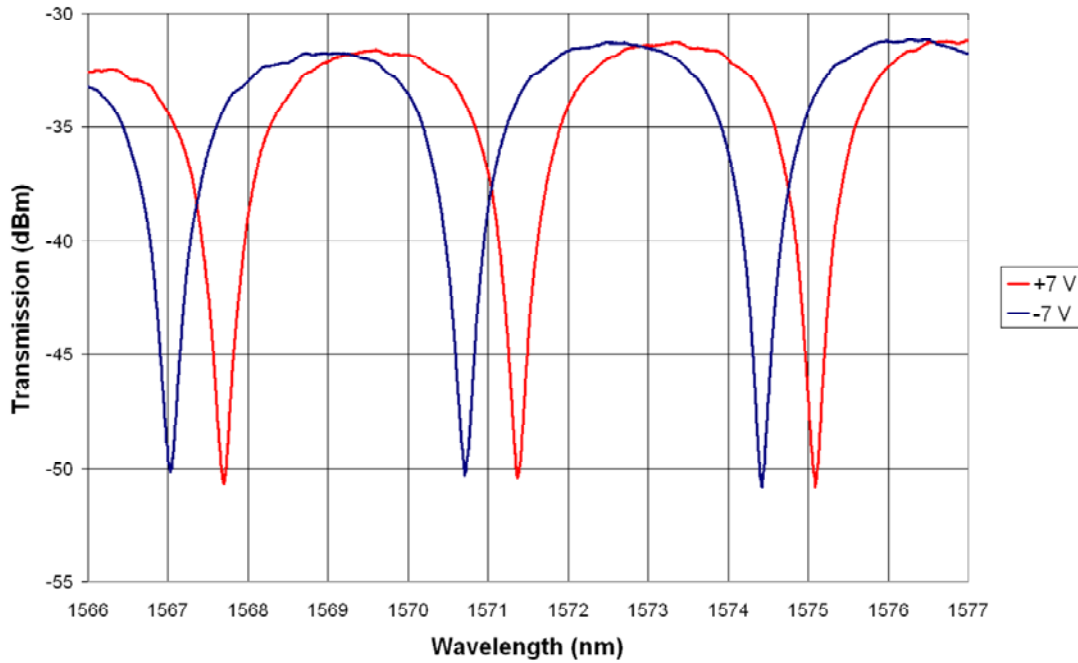


Figure 3.13. Resonance shifting in the best performing dendrimer-based polymer-coated device showing $\sim 0.042 \pm 0.008$ nm/V of tuning. The device is poled at +10 V and biased at +7 and -7 V with the outer ring considered as positive.

Another measure that is appropriate to use here for describing the modulation effect is FWHM (full width at half maximum) tuning voltage, which is determined both by the resonance shifting amount and the resonator Q value. A sample device in Figure 3.14 shows a FWHM tuning voltage of 15 V. The figure also shows traces at intermediate biases, and a linear relationship is apparent.

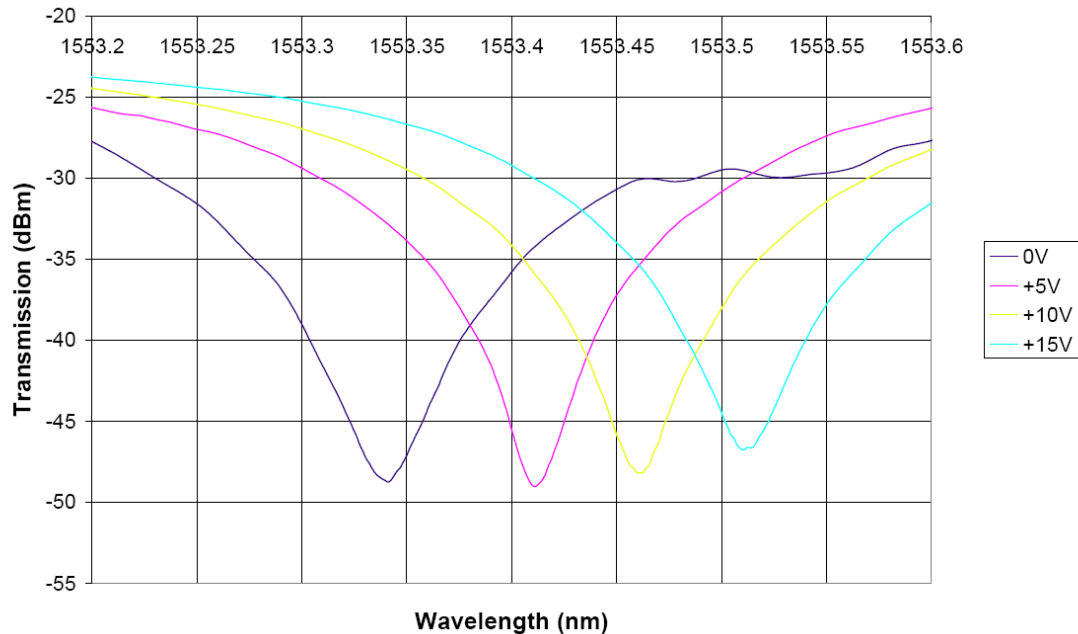


Figure 3.14. YLD/APC-coated sample showing linearly increasing tuning and FWHM (full width at half maximum) tuning with +15 V of electrical bias. The device is poled at 125 °C and +18 V for 15 minutes.

For AC tests, a function generator is used to drive the device with a square-wave input signal. Ideally the monochromatic optical input should be tuned to the quasi-linear slope of the resonance peak for the largest output swing, and this is approximated in the experiment by slowly dialing the optical pump wavelength until maximum extinction is observed. Retrofitting the output optical modulation level to the original optical wavelength sweep taken with zero bias will allow us to calculate the tuning efficiency similar to what is done in the DC tests above. A typical time-domain test is run at a speed of 1 kHz square wave, as shown in Figure 3.15, where both the driver signal and optical response are clean and crisp, with little sign of falloff.

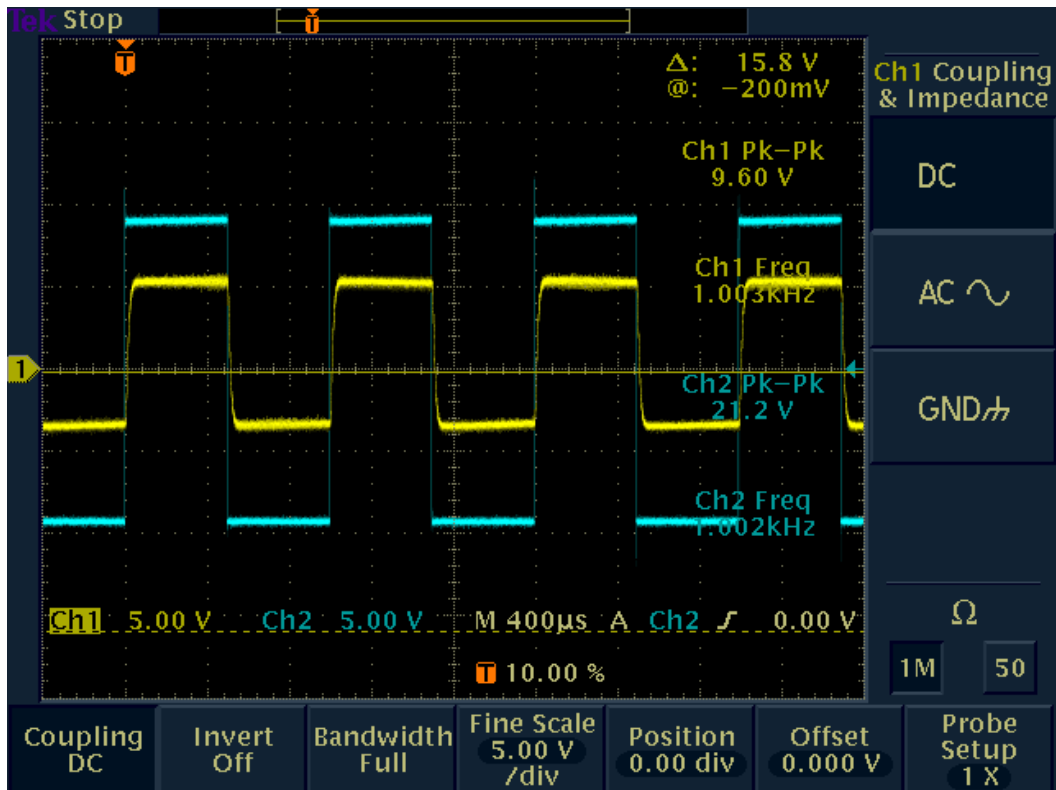


Figure 3.15. Typical low speed 1 kHz AC results of slotted ring modulator showing the yellow optical trace closely following driving signal. This device is coated with YLD/APC polymer, poled at 15 V, and has a 140 μm gap.

As the speed of modulation is raised, the electrical parasitics in the system start to kick in causing both the driver signal and the optical response to degrade showing significant delay and falloff. This falloff, however, is solely due to equipment limitation and the electrical properties of the devices, not the limitation of electro-optic polymer response time. Figure 3.16 below shows the same modulator device driven to a reasonable speed of 6 MHz. Notice the difference in optical response levels in the two figures is mostly due to different gain and speed settings on the New Focus 2011 photodetector (New Focus, San Jose, CA) used.

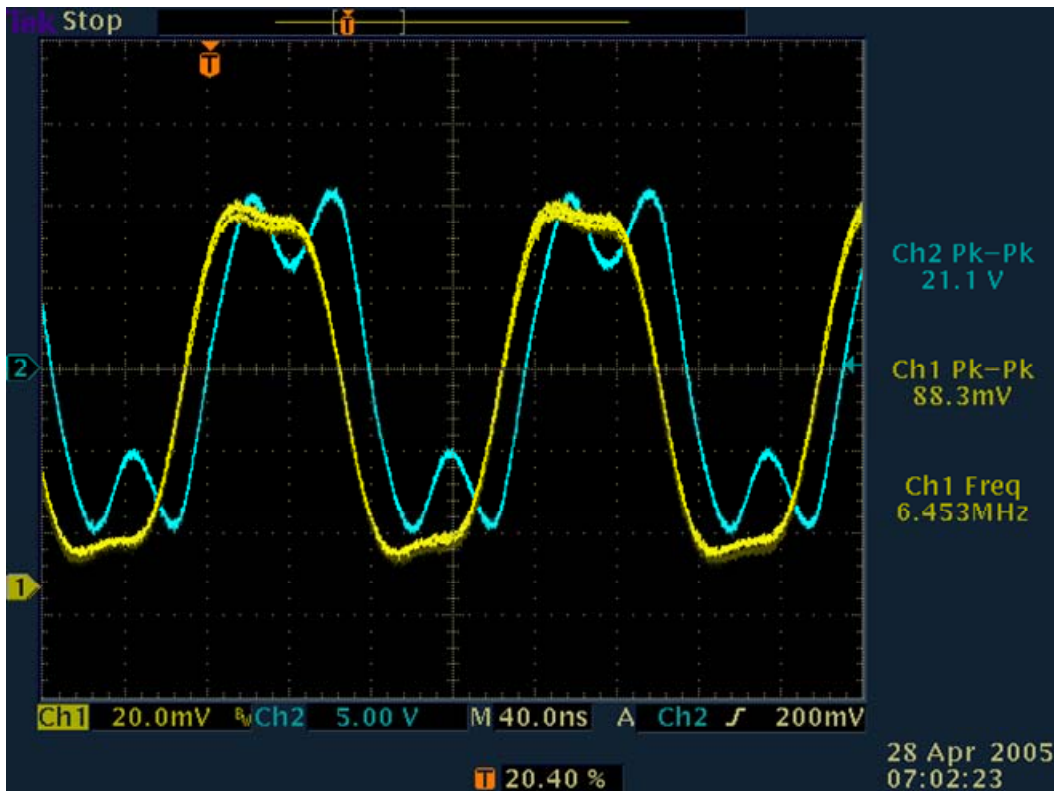


Figure 3.16. AC test results of a slotted ring modulator at 6 MHz showing 13 dB of modulation extinction in the yellow optical trace. This device is coated with YLD/APC polymer, poled at 15 V, and has a 140 μm gap.

In summary, these proof-of-concept modulation results obtained with slotted ring resonators have shown the potential of incorporating nonlinear polymer with silicon to build highly compact modulators that can achieve high tuning efficiency and have significant advantages over some other approaches that typically have much less confined optical mode and larger physical sizes. The compact size, confined mode, and high electric field intensity in combination contribute to the leading performance of these polymer-silicon hybrid structures. The results documented in this chapter have also shown a comparable material nonlinearity in the form of r_{33} as traditional lithium niobate material.

A few conceivable direct improvements include increasing resonator Q factor that will allow better modulation extinction with the same tuning range, and improving nonlinear performance by using better polymer material or enhancing poling efficiency. It is noted that the 22 pm/V r_{33} value achieved here is only a fraction of the bulk material value measured off this dendrimer-base nonlinear polymer variant. Also, for practical considerations it is desirable to further lower the driver signal voltage and to improve the high-frequency response of these modulator devices. Discussions will be expanded on these topics as well as other related nonlinear devices and experiments in the following chapter.

OTHER SECOND-ORDER NONLINEAR DEVICES

4.1 Optical Rectification Detector

During the testing of slotted ring resonator-based modulators as described in the previous chapter, an unexpected finding was discovered when the rings were pumped with a coherent optical source without any electrical bias: tiny current flows were observed. This resembles the operation of an optical detector that uses photocurrent, and the phenomenon was further investigated and proven to be a well-known ultrafast effect, called optical rectification.

Referring back to Section 3.1, combining equations (3.1) and (3.2), we get the second order nonlinear relationship as shown in equation (4.1) below. The nonlinear term in this case is related to any sort of electric field, not limited to DC or slow RF signals. There is no reason to doubt that a similar process can also happen with an optical signal, which is capable of producing an ultrafast varying electric field. This generality is what differentiates parametric interaction of this kind from other nonlinear effects. In the literature, optical rectification is usually referred to as the generation of a DC electric polarization by an intense and constant power optical beam propagating in a nonlinear medium [22].

$$D = \varepsilon_0 (\varepsilon_r E + \chi^2 E^2 + \dots) \quad (4.1)$$

During modulation experiments, external DC or RF field applied is typically far in excess of the electric field from the optical signal, and the term that produces the material birefringence is the only term of importance in the above equation. Our slotted waveguides, however, have a very large electric field as most of the radiation is confined to a $0.01 \mu\text{m}^2$ cross section. The electric field in these waveguides is approximately uniform in the transverse direction, with a magnitude of $10^8 \sqrt{P}$ V/m. Here, P is the optical power in standard unit watt. When external electric field is missing and optical field is large, the nonlinear term resulted by optical signal becomes dominant. Assuming a coherent light source pumps a slotted ring resonator structure, at a given point along the ring, the optical field can be written as below.

$$E_{optical}(t) = A \cos(\omega t + \theta) \quad (4.2)$$

Therefore, the E^2 term in equation (4.1) can be expanding into the following.

$$E_{optical}^2(t) = [A \cos(\omega t + \theta)]^2 = \frac{A^2}{2} \cos(2\omega t + 2\theta) + \frac{A^2}{2} \quad (4.3)$$

One can notice from above that on top of the frequency doubled term, there is also a non-time-varying term, which essentially serves as a DC term. This explains the origin of optical rectification in a nonlinear medium, which has been demonstrated in the past in bulk semiconductor materials [42]. If this is indeed what generates the trickle photocurrent observed in our slotted ring resonators, then the closely positioned electrodes (essentially the two arms of slotted waveguide) are sitting right at the edge of the optically induced field, and establish a virtual DC voltage source by converting a small slice of the optical

power into electrical current, through the effect of optical rectification. A set of experiments are designed and carried out to verify this conjecture, and to investigate this possible correlation both quantitatively and qualitatively. Figure 4.1 below illustrates an equivalent circuit model that depicts how a slotted ring modulator device can be operated reversely to produce measurable electrical signals related to the power level of optical pumping.

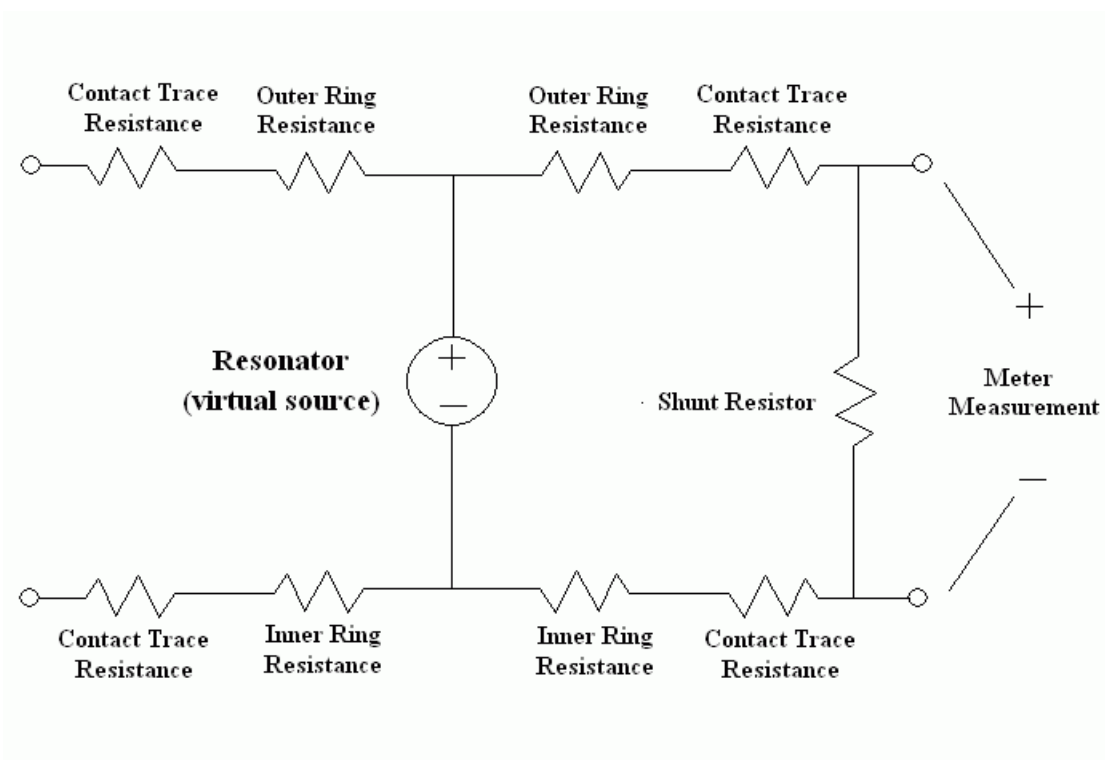


Figure 4.1: Equivalent circuit diagram of a slotted ring modulator device exhibiting optical rectification and serving as a virtual DC voltage source that can be measured at the terminals originally used for driving the modulator.

4.2 Testing and Verification of Optical Rectification

The test setup is very similar to that of the modulation test in the previous chapter. Coherent optical source is coupled in and out of devices with an insertion loss of approximated 8 dB. Optical signal is provided by an Agilent 81680A tunable laser module (Agilent Technologies, Santa Clara, CA) and in some cases an EDFA (erbium doped fiber amplifier) from Keopsys Corporation (Lannion, France). A continuous optical signal inserted into a poled polymer ring results in a measurable current established between the two pads, which are electrically connected through a picoammeter.

The fact that there is no external bias applied to this system or indeed any energy source, other than the optical signal, leads to the implication that power has to be converted from the optical signal. To conclusively establish that the conversion mechanism is actually optical rectification instead of some slower or nonpolar mechanisms such as heating, a number of additional experiments need to be thoughtfully designed and performed. In the first set of experiments, we make use of known instability in some polymers tested previously for modulation. Namely, when a strong enough steady bias approaching the original poling voltage is applied to a poled structure at room temperature for a prolonged period, the existing poling effect can be either weakened or enhanced. Substantial changes in the photoresponse of the device are observed during this experiment when photocurrent is intermittently measured as strong biases are applied in rotation, and the trend of change depends on the polarity of the bias voltages. The outcome is consistent with the expected influence of repoling of the device in place at room temperature except in one case. Specifically, if the external bias is applied opposing the original poling direction,

conversion efficiency will generally decrease, while an external bias in the same direction as original poling field will increase conversion efficiency. It should be noted that the actual optical power reaching slotted rings in these experiments is usually less than 1 mW due to coupling loss.

Table 4.1. Room temperature repoling results showing the dependence of steady state photocurrent on repoling biases applied to a slotted device. The device is first poled at 110 °C and -12 V.

Action performed	New steady state current (6 dBm input)
Initial state	-5.7 pA
+10 V for 2 minutes	0 pA
-10 V for 2 minutes	-7.1 pA
+10 V for 2 minutes	-4.4 pA
+10 V for 4 minutes	-6.1 pA
+10 V for 4 minutes	-4.5 pA
-10 V for 2 minutes	-14.8 pA

For the nonlinear polymers we work with, it is known that the direction of χ^2 as defined in equation (4.1) is aligned with the poling electric field [41, 42]. Given this information, a closer look at the physics of propagating optical field reveals that the direction of optical rectification current should be opposite to the χ^2 vector, and hence in the same direction as electrical poling. The reasoning for this conclusion is briefly

explained here, and more details can be found in [40]. Assuming light is polarized in plane along x-axis perpendicular to nanoslots and propagates along the z-axis, then the DC field induced should also be in the x direction having a constant magnitude C . The optical field can be written as:

$$E_{optical} = Ae^{i(kz-\omega t)} + Ae^{-i(kz-\omega t)} \quad (4.4)$$

Further assuming that χ^2 is reasonably small, and the induced DC electric field only exists in the slots and is roughly uniform, then the DC term of displacement electric field right at the interior edges of slotted waveguide arms should satisfy the continuity condition as stated in equation (4.5) below:

$$D^- = 0 = D^+ = \epsilon_0 \left(\epsilon_r C + \chi^2 C^2 + 2\chi^2 |A|^2 \right) \quad (4.5)$$

It is fair to assume that optical field intensity in most cases is much greater than the induced DC field, and thus we can arrive at this final opposite polarity relationship:

$$C = -\frac{2\chi^2}{\epsilon_r} |A|^2 \quad (4.6)$$

The second set of experiments serves the purpose to further understand the polarity issue of this photoconversion mechanism, based on the theoretical reasoning above. Specifically, five separate devices are measured after being poled in various directions, and in some cases thermal cycled or repoled. Every initial poling response detailed in Table 4.2 is consistent with the theory deduction. In fact, all but one repoling case are in favor of our conclusion, showing a strong correlation of photocurrent existence and direction with the

poling condition of polymers in nanoslots. The outlier is likely due to the fact that some polymer species decay rapidly through the course of testing, particularly when higher optical power is fed through the materials, which in many cases results in a much weaker reverse response after repoling compared with initial poling response.

Table 4.2. Thermally cycled poling and repoling results of five different devices. Measurements are in sequential time order down the list, and the only anomaly happens when the second device is thermally cycled and tested repeatedly.

Device	Action	Current polarity of optical rectification
1	Positive poling	Positive
1	Thermal cycling to poling temperature with no voltage	Rapid fluctuation, did not settle
1	Negative poling	Negative
2	Negative poling	Negative
2	Thermal cycling to poling temperature with no voltage	None observable
2	Positive poling	Negative
3	Negative poling	Negative
4	Positive poling	Positive
5	Negative poling	Negative

The third set of experiments is targeted toward producing negative results and excluding the possibility of a mistaken measurement of photocurrent. The optical power

input to devices can be turned on and off by simply moving the fiber array away from the chip mechanically, without changing the circuit electrically or in any other fashion at all, and the on and off switching in electrical output signal is indeed observed as expected. A chip is also coated with PMMA and tested in the exact same way, resulting in no observable photocurrent. In addition, some detector devices shown in It should be noted that the actual optical power reaching slotted rings in these experiments is usually less than 1 mW due to coupling loss.

Table 4.1 and Table 4.2 were tested prior to any poling or heating event is performed, and again no current was observed. It should be noted that the actual optical power reaching slotted rings in these experiments is usually less than 1 mW due to coupling loss.

Finally, in order to establish a quantitative relationship between the laser power in the electro-optic polymer and the photocurrent, lock-in measurements can be performed by slowly modulating the laser optical output power (using the internal modulation function on the Agilent 81680A system) up to 1 MHz. By using a lock-in amplifier a noise floor of about 0.2 pA can be achieved. This results in a reasonable dynamic range for the typical 10-200 pA photocurrent readings. Figure 4.2 panel A and B show optical transmission curves for two typical devices. Figure 4.2 panel C shows several traces of output current vs. input laser power, and a fairly linear relationship is observed. This linear relationship can be written as $I = cP$, where I represents the output photocurrent and P is the input laser power. The proportionality constant c ranges from 88 ± 10 pA/mW at a 1 kHz lock-in measurement when the optical wavelength is on resonance, changing to a lower value of

58 ± 8 pA/mW off resonance for our best device. This change in current observed is indeed as expected since more optical power resides in the ring resonator when it is on resonance. Specifically, because the generated photocurrent is supposed to be quadratic in electric field intensity from equation (4.1), it is naturally expected to be linearly proportional to the optical input intensity, which is in accordance with our observations. More convincingly, Figure 4.2 panel D depicts another demonstration of the detector's dependence on optical input power. Basically, multiple current measurements are taken with input laser wavelength being tuned over a 7 nm range. An overlaid rescaled transmission trace illustrates the resonance characteristics of the ring resonator tested. As can be seen clearly in the graph, the amount of output current increases as the laser is tuned onto a resonance peak and decreases otherwise. This again indicates that the overlap between the electro-optic polymer in the resonator and the optical mode is responsible for the photocurrent. It should not be surprising that a small photocurrent is still measured even when the laser is off resonance, since the amount of radiation in a low-Q ring resonator is non-negligible even off resonance. This detector function is measured at speeds up to our equipment limitation of 1 MHz, without observable falloff, which is yet another sign of consistency with the optical rectification mechanism. Another reason for not being able to go even higher in test speed is that the substantial output impedance prevents these ring resonator devices from being measured at higher speeds.

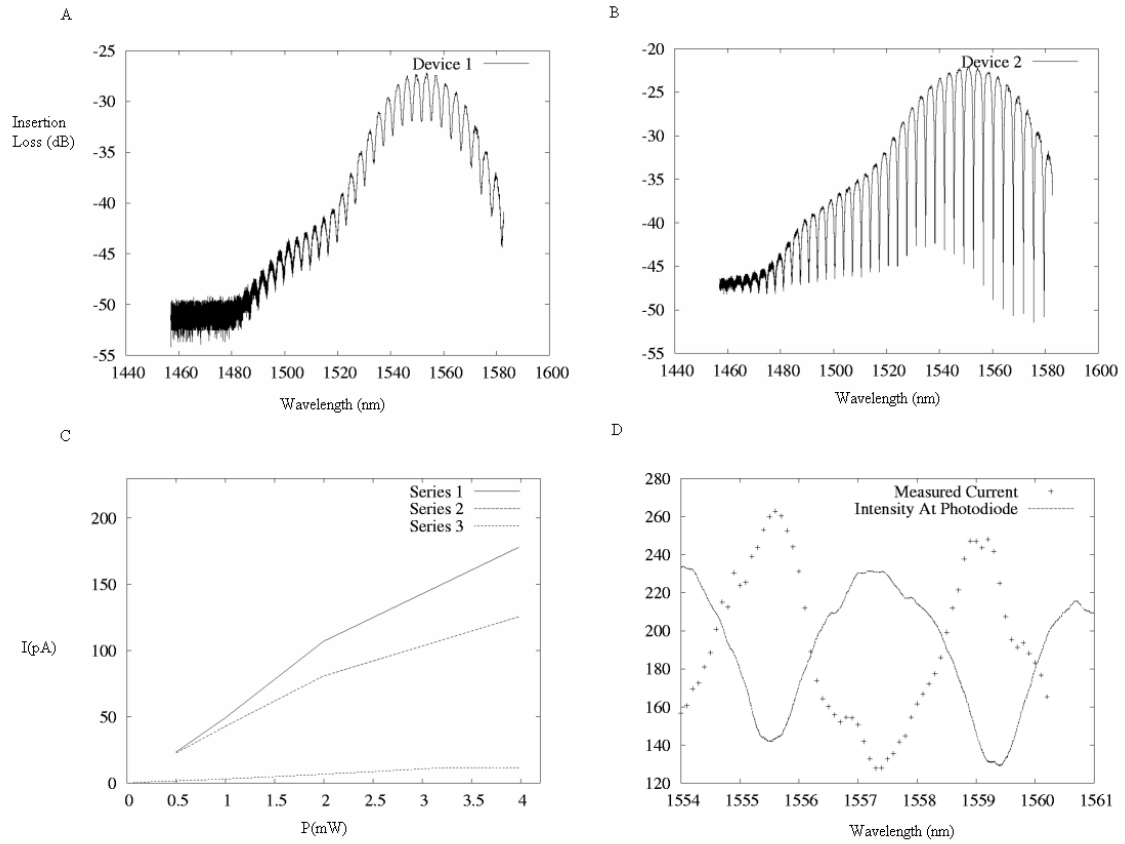


Figure 4.2. Panel A and B show transmission spectrums of two detector devices. Panel C shows photocurrent vs. optical power for three separate measurements: series 1 is for device 1 with 1549.26 nm on-resonance input, series 2 is for device 1 with 1550.5 nm off-resonance input, and series 3 is for device 2 with 1551.3 nm on-resonance input. Panel D shows output photocurrent as a function of wavelength, overlaid with rescaled transmission spectrum showing resonance peaks.

It is worth mentioning that in all test cases, while lock-in measurements provide cleaner and more accurate recording, photocurrents can always be readily observed with merely a picoammeter, or by simply connecting an oscilloscope to the output terminal and real-time monitoring the optically induced voltage deflection.

In the most sensitive device coated with YLD/APC, a DC current of ~ 1.3 nA was observed, indicating an electrical output power of $\sim 10^{-9}$ of the optical input power (5×10^{-6} mW of output for approximately 0.5 mW coupled into the chip). Control devices, in which PMMA or unpoled electro-optic material were substituted as stated above, show no photocurrent. With resonator Q factors ranging from 3k to 5k, and assuming approximately 7 dB of input insertion loss, in the best case as much as 0 dBm might be circulating in a resonator on resonance. This implies a peak electric field due to the optical signal of approximately 3.1×10^6 V/m. The induced static nonlinear polarization field is then nearly 1000 V/m, which amounts to a voltage drop of 1.4×10^{-4} V across a 140 nm gap. If this voltage is assumed to be perfectly maintained, and the load resistance is assumed to be $2 \text{ M}\Omega$, then 70 pA would be generated, within a factor of 5 of the typical measurement of 350 pA for 6 dBm of input. The conversion efficiency from these first-generation devices is certainly far from the ultimate limit, and can be explained by the high insertion losses in our system. The current couplers only pass on a small fraction of the total input power from fiber onto chip, and the low-Q resonators also limit the path length of light circulating in the ring and interacting with electro-optic material. Furthermore, a significant amount of light is also dumped to an output port by design.

It is important to note that the current generation mechanism is not yet fully understood. In particular, it is not clear what provides the mechanism for charge transport across the gap. The APC material in which the nonlinear polymer is hosted is in theory insulating, and though it does exhibit photoconductivity effect under visible light, it is unclear whether it can for near-infrared radiation. Photoconductivity due to second harmonic generation may play a role in this effect, but it is certainly true that current flows

through the nanogaps, the only region in the entire system where an electromotive force exists. However, photoconductivity alone is not adequate to explain the reversal of photocurrent observed in these detector devices when poling direction is reversed, as well as the conversion of the optical input into directed current in general. The only mechanism known to our knowledge that can adequately explain this data is optical rectification.

The path toward improving the detector for practical use is very similar to that of a modulator described in the previous chapter: higher Q, better loss figure, improved polymer and poling performance, and enhanced high speed characteristics. If a 10-fold improvement in the Q factor of resonator can be achieved while still maintaining reasonable extinction, then the intensity circulating in such a ring would be about 13 dB up from the intensity of the input wave. By comparison, a Q of about 1K and high extinction would yield a peak circulating intensity roughly the same as the intensity in the input waveguide. It is reasonable to expect that such a design trade-off can be achieved to get at least 10 dB of improvement in circulating optical intensity, which translates to overall conversion efficiency. The optical losses of the polymer materials could turn out to be a limiting factor for building high-Q devices. In the current generation of devices, since the polymer coating does not cause dramatic deterioration to the relatively low Q factor rings, it is fair to estimate a loss upper bound of -10 dB/cm. A series of high-Q ring measurements can be worked on to further examine the polymer losses. It should be noted that not only is the induced DC voltage linear to optical input intensity and quadratic to electric field intensity, the extracted electrical power is actually proportional to the voltage

squared. This indicates a dramatic E^4 dependency of harvested power, which means any improvement of electric field will likely lead to a vast detector performance boost.

In summary, the same slotted ring resonator used as an optical modulator has been used to demonstrate a photocurrent generation process that can be explained by optical rectification theory. As first-generation devices, these rings provide a convenient and compact solution for observing this effect, and one can see them being used for practical detection with improvement performance. Two distinct and potentially interesting advantages of optical rectification-based detection as shown are the high-frequency nature of the mechanism and the lack of dark current compared with a traditional photodiode detector. Of course, similar to the modulators in the previous chapter, electrical speed limitation and poling efficiency remain two major issues that call for attention in future design improvement.

4.3 ROADM Device

Besides utilizing second-order nonlinear effects for optical modulation, the idea of tuning polymer coated silicon ring resonators can be extended into building devices that achieves actively tunable wavelength filtering. Such a device is usually called a ROADM, reconfigurable optical add-drop multiplexer, which allows individual wavelengths carrying data to be “added” into or “dropped” out from the main optical transport path. The capability of being tunable and performing wavelength channel operation completely in the

optical domain makes ROADMs a much needed component in a modern WDM (wavelength division multiplexing) optical communication system.

A collaboration project was carried out with researchers at Boeing Phantom Works in Seattle to build a single input/output channel ROADM with 4 add ports and 4 drop ports, also known as a $1 \times 4 \times 1$ ROADM, using silicon ring resonators. Most design work and part of fabrication and measurement were done here at Caltech. Figure 4.3 below shows a schematic of the system overlaid with device layout. Four rings each with input and output ports are used for adding and dropping wavelengths that correspond to their resonance peaks.

Ports for $1 \times 4 \times 1$ ROADM

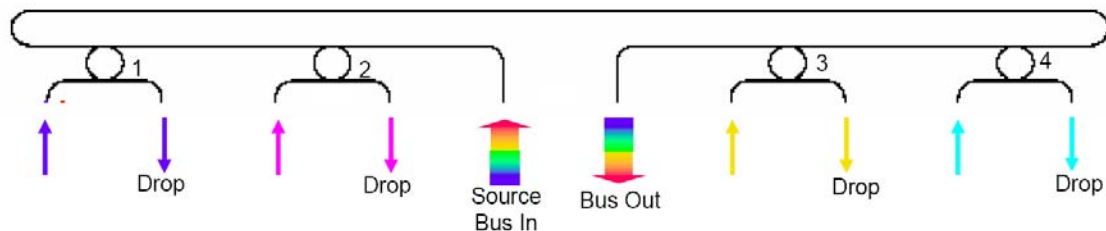


Figure 4.3. Layout of a typical ring resonator-based $1 \times 4 \times 1$ ROADM with ports colored and labeled.

At the time of execution, slotted waveguide structures, while working well for individual add-drop ring resonators, had too much loss to perform consistently well for a long bus signal path needed. Instead, an approach using regular ridge waveguide based

ring resonators was adopted. Naturally, the benefit of having electrodes in close proximity without hurting optical transmission is lost in this case, and more complicated multilayer fabrication has to be performed in order to build top and bottom metal electrodes as shown in Figure 4.4. The electrodes are used to both pole and tune the rings.

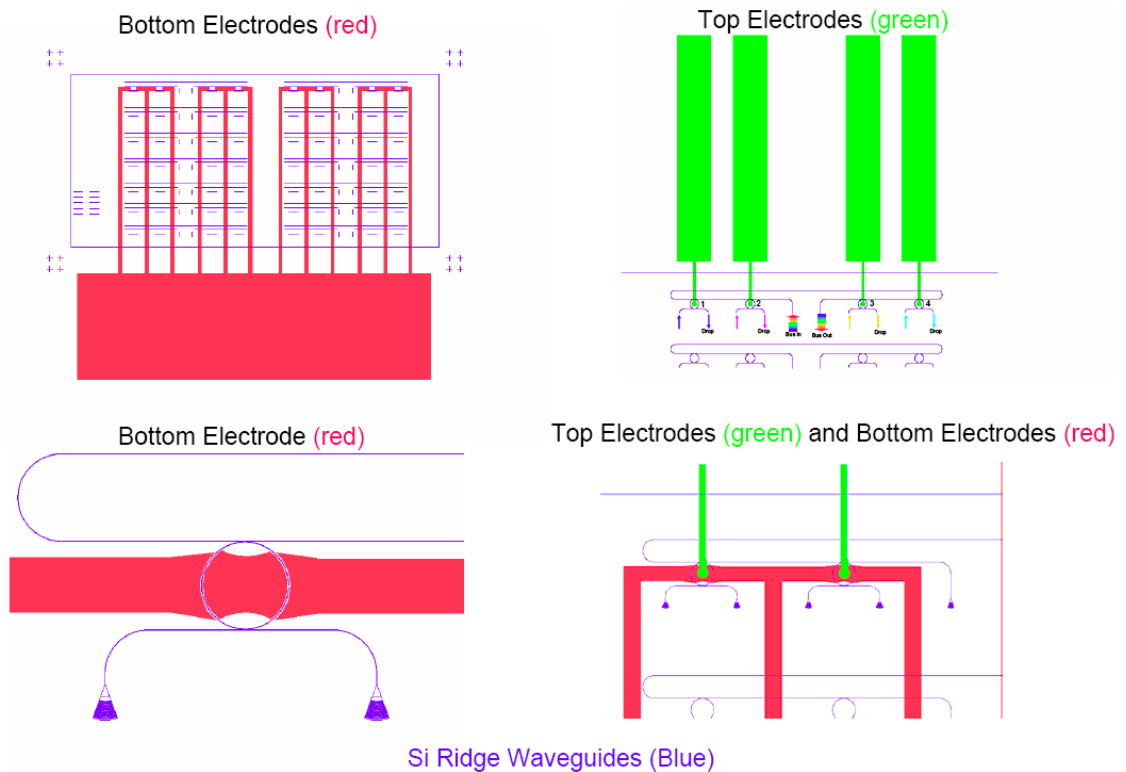


Figure 4.4. Layout of top and bottom electrodes, which are used to both pole polymers at high voltage and tune individual rings during ROADM operation.

As it has been pointed out in Section 3.2, design schemes that involve external electrodes that stand off from the optical waveguides are usually vulnerable to this inevitable compromise of lower electric field intensity, due to the limitation of distance between electrodes. This rule holds true here as well with these ROADM devices. A

typical electrode gap size used is 3 μm , a stunning difference of more than 20 \times from a typical slotted waveguide device. The fact that the poling electric field direction is also not aligned with optical field polarization (which is in plane) further reduces the system efficiency, resulting in a two-thirds reduction in nonlinearity usually. As it will become evident by looking at data figures below, the required poling and operating voltages are much higher in this case; hundreds of volts are often used. Here in Figure 4.5 and Figure 4.6, measurements are taken from the add-drop ports as well as the bus ports, exemplifying how wavelength filtering and reconfiguration work in our ring resonator based ROADM devices. The typical tuning efficiency as shown in these figures is about 0.001 nm/V (0.12GHz/V), and in some better-performing devices the number can go up to 0.004 nm/V, still a full order of magnitude lower than slotted ring implementation as predicted.

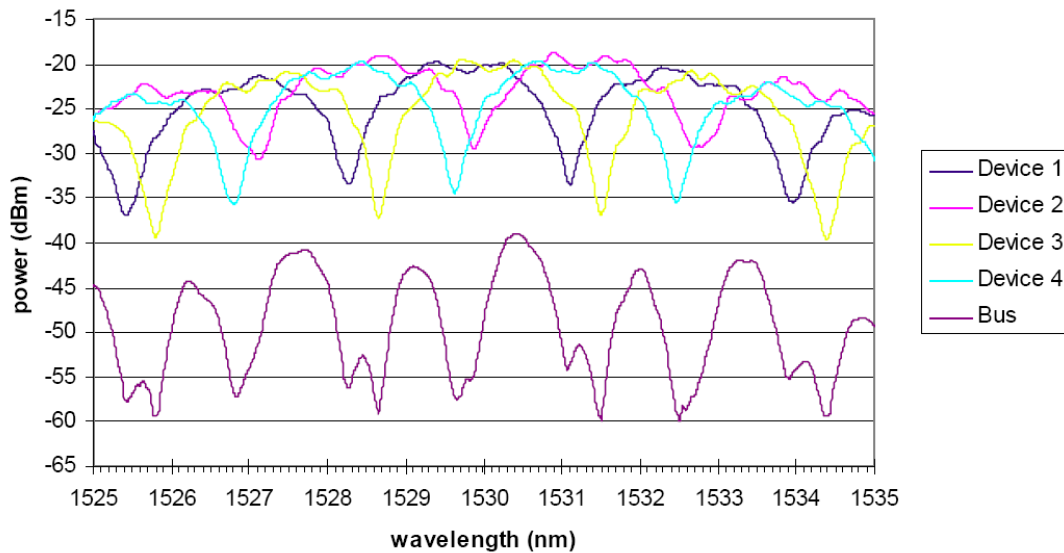


Figure 4.5. Linear responses of a 1 \times 4 \times 1 ROADM coated in YL124/APC. The top curves are for individual add-drop rings, and the bottom curve is the total bus response, all measured without any tuning voltage.

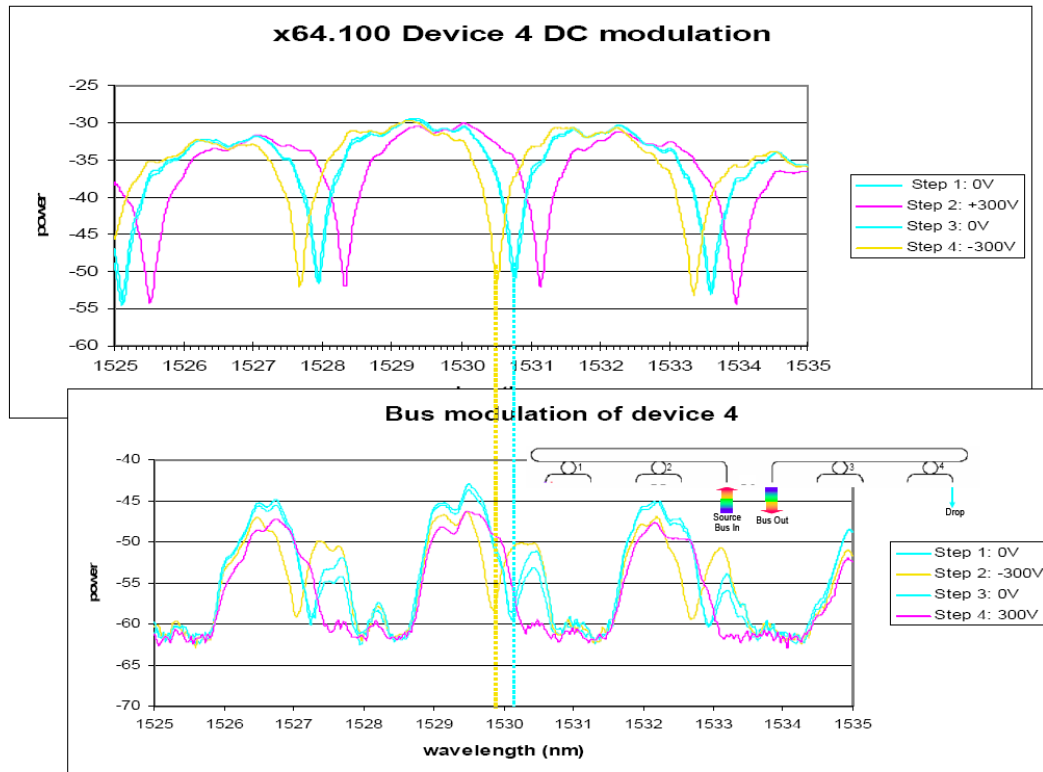


Figure 4.6. Tuning responses of a typical $1 \times 4 \times 1$ ROADM device coated in YL124/APC and built with a $3 \mu\text{m}$ electrode gap. The top graph shows ring number 4 being tuned with $\pm 300 \text{ V}$, and the bottom graph shows corresponding bus responses. The dotted lines drawn between the two graphs illustrate how a wavelength channel can be added or dropped.

Despite the lower performance of these metal electrode equipped solid ridge waveguide devices, the linearity is shown to be rather close to ideal as in Figure 4.7. This is consistent with theoretical prediction, and a good indication that the polymer is acting properly as a second-order nonlinear medium.

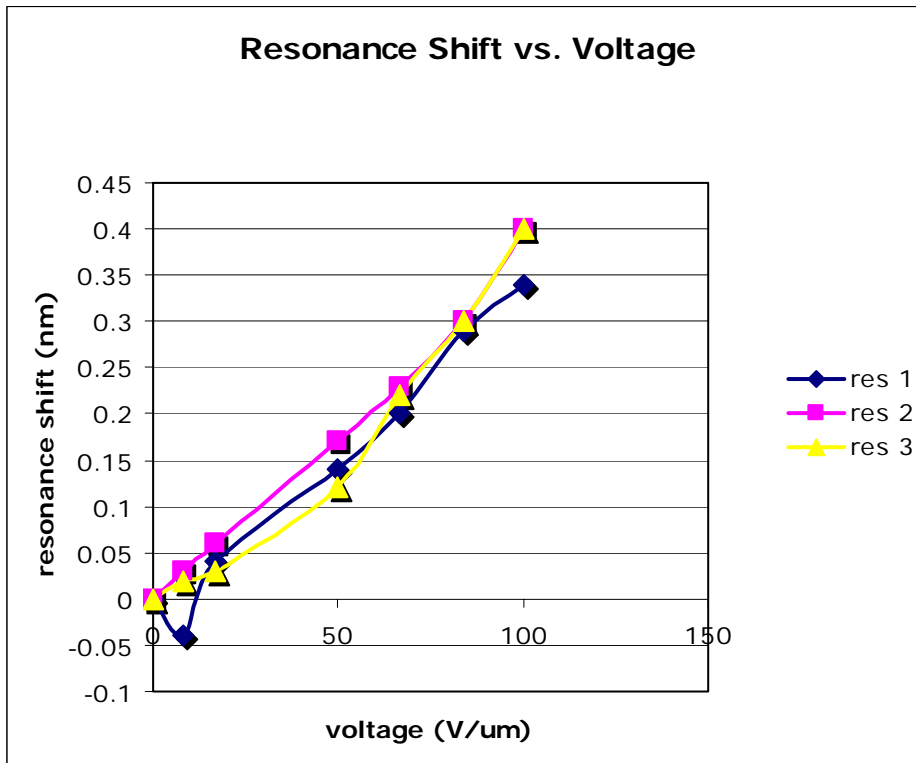


Figure 4.7. Resonance shift performance of add-drop rings from three separate ROADMs devices showing linear tuning characteristics. All devices were coated with YL124/APC and poled at 210 V across a 3 μm electrode separation.

The outcomes of this project have shown another very promising perspective of using polymer-silicon hybrid platform for practical optical communication needs. Though the current generation of ROADMs devices is suboptimal in performance and greatly limited by large electrode separation, it is nevertheless a meaningful first step as a proof-of-concept endeavor. In comparison with slotted devices, it is a great lesson about how much performance difference a change in structural design can bring about, even in highly similar material platform using comparable fabrication techniques. Besides the obvious upgrade to slotted waveguide geometry, most improvement paths mentioned in the previous part of

this dissertation during the discussions on slotted ring modulator and detectors are also relevant and valid.

4.4 Segmented and Slotted Waveguides for Improved EO Performance

The use of second-order nonlinear materials provides an attractive method for achieving modulation or any electro-optic effect based functions at telecommunication wavelengths. As it has been mentioned above and recently demonstrated [33-35, 40], the χ^2 moment of nonlinear polymers is ultrafast, raising the prospect that extremely high speed devices, most predominantly modulators, can be realized, limited only by the performance of the supporting passive electronics. In fact, practical modulators with speeds on the order of 165 GHz have recently been demonstrated [43].

In a hybrid slotted waveguide-polymer system discussed in the previous text, the silicon waveguide acts as a microscale transparent contact and the extremely narrow slot provides for a very high electric field per volt. This system compares favorably to modulators in which the electrodes are stood off from the waveguide and do not touch the optical mode, due to the smaller gap sizes involved and the commensurately larger electric fields per volt. As mentioned, even using slots on the order of 100 nm or more in width, more than five times enhancements in effective index shift have been obtained with slotted waveguides for identical modulation materials and driving voltages, when compared with external-electrode approaches [6, 37, 40]. This significant inherent advantage, however, does not come without a price. The major challenge here lies in the fact that for slotted

waveguides, the waveguide core must be electrically conductive. Section 3.4 describes an empirical process to electrically activate cores made of silicon by introduce a well-controlled dose of impurity doping. While this is good enough for supporting DC or even slow AC signal over a reasonable distance, it turns out to be insufficient for radio or millimeter-wave propagation. Doping with 2×10^{18} atoms/cm³ (a less aggressive doping scheme that was later adopted in lieu of 1×10^{19} atoms/cm³ for better optical characteristics) of phosphorus, for example, leads to a resistivity of 0.04 Ω -cm, but increases waveguide loss by about -10 dB/cm. For some applications, it might be necessary to dope with an even lower concentration to avoid this loss penalty. To appreciate the limitation that this relatively large resistivity implies, consider a most common modulator, a Mach-Zehnder implemented in slotted silicon waveguide on oxide as shown in Figure 4.9. Assuming the reference arm and the sample arm (the arm that is modulated) are both around 1 cm in length, which is a moderately low number for a typical integrated MZM (Mach-Zehnder modulator) structure, the sample arm slotted waveguide geometry can be simplified as the diagram shown in Figure 4.8.

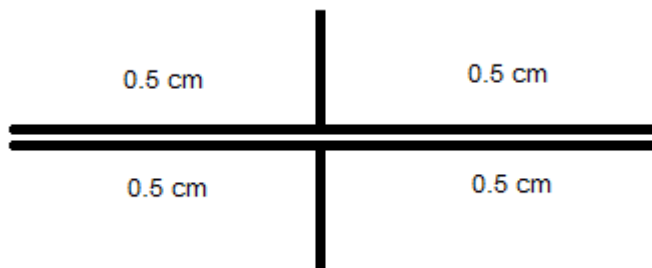


Figure 4.8. Simplified diagram of slotted MZM signal arm geometry showing a single pair of electrical contacts.

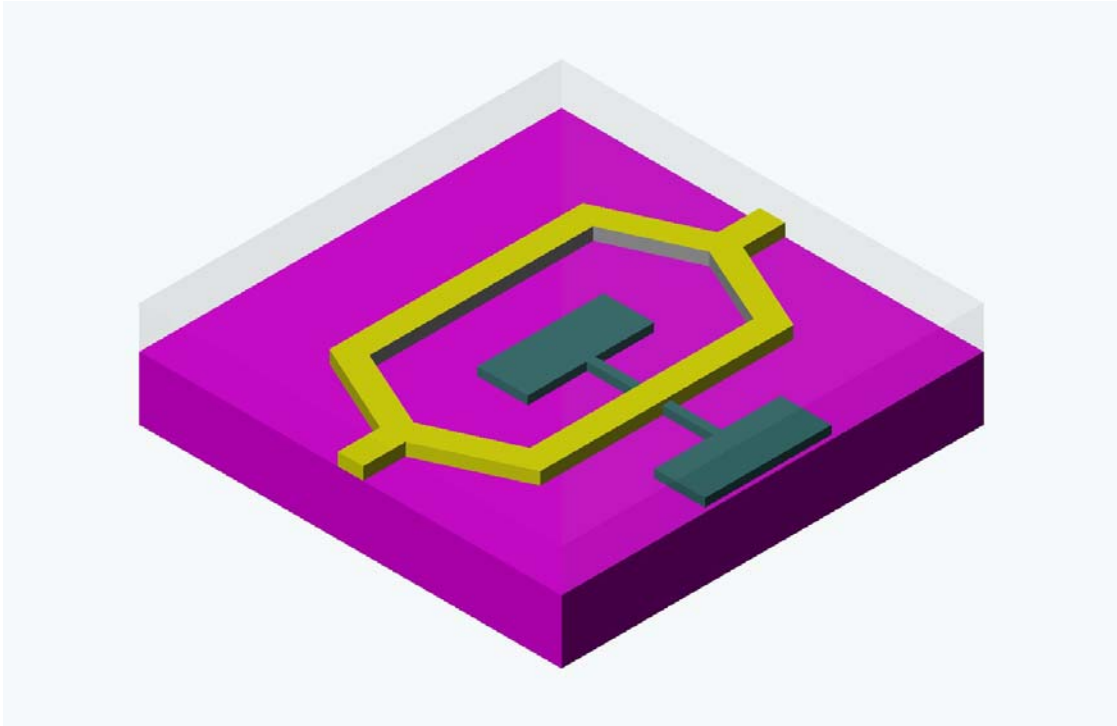


Figure 4.9. Diagram of a slotted MZM in polymer-silicon hybrid implementation. The green metal pads are contacting the modulation arm at a single point, while the reference arm is unaffected. Nanoslots and optical couplers are not shown for simplicity.

Further assume the design to be similar to that used before for ring resonator modulators, with edge height of 110 nm, split arm size of 300 nm on each side of a 120 nm slot, and doped with phosphorus as discussed above. It is possible to get a first-order approximation of the turn-on time using a simple parallel plate capacitance model. The series resistance of the slotted waveguide in this case is linearly distributed along the optical path, and is the dominating factor. The RC based time constant turns out to be approximately 11 μ s, leading to a speed limit for the Mach-Zehnder of 14 kHz. Clearly, such a slow turn-on time would pose itself as the system speed bottleneck and largely negate the benefit associated with the ultrafast performance of the nonlinear polymers.

Previously, segmented waveguides have been used to provide electrical contacts to non-slotted waveguides [44]. Marginal waveguide losses were achieved for these structures, in the best case -16 dB/cm. Such losses were acceptable for the application in question, which required only very short segmented regions. Here, a similar idea can be applied to slotted waveguides. We start with the aforementioned standard slotted waveguide [38, 39], 110 nm thick with 300 nm sides separated by 120 nm, as shown in Figure 4.10. Note that for regular slotted waveguides like this on a similar substrate, we have previously obtained waveguide losses [45] of -10 dB/cm. This waveguide is also clad with PMMA with an optical index of about 1.5 [46, 47].

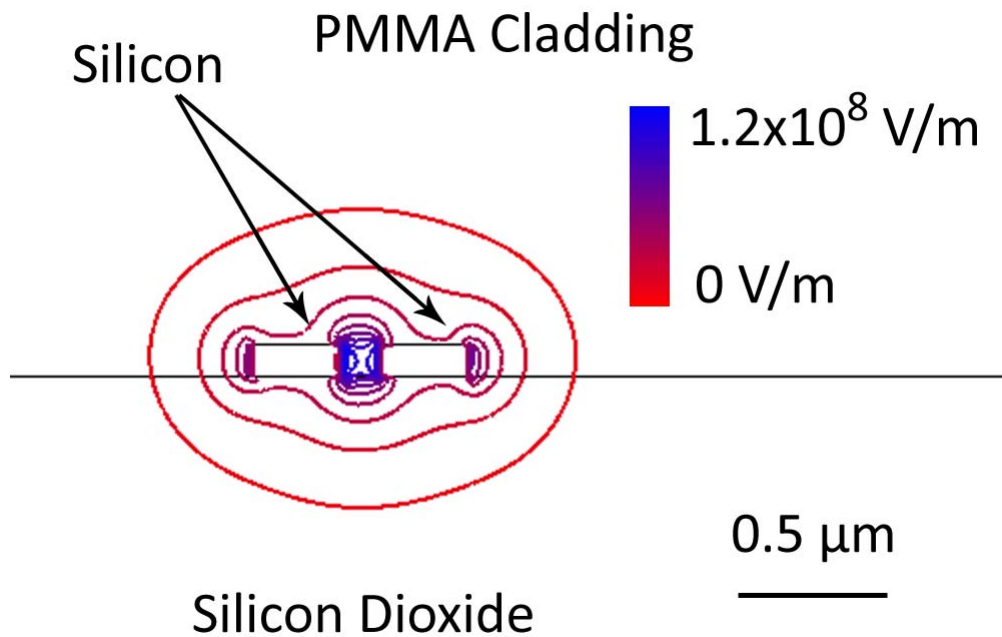


Figure 4.10. Color rendered modal pattern of a conventional slotted waveguide with 120 nm of gap near 1550 nm. The mode is plotted with 10% contour of $|E|$ assuming 1 W of average power flow.

By introducing subwavelength nano-sized silicon leads that are periodically segmented on the two sides of a standard slotted waveguide above, it is possible to find well-propagating Bloch mode at a given wavelength, such as around 1550 nm. Two designs listed in Table 4.3 are closely investigated with both simulations and experiments. Maxwell's equations are computationally solved in the frequency domain to simulate these structures. As we can see from Figure 4.11(b), that the cross section of the optical mode at the segmentation solved by a conventional mode solver [10] is very similar to a normal slotted waveguide mode, with reasonably good confinement. By observing the propagation of the slotted mode in a 5 μm long three-dimensional simulation, we were able to determine the dispersion diagram of the slotted mode, shown in Figure 4.11(c). Note that the waveguides are very broadband, having relatively linear dispersion over the course of many tens of nanometers of spectrum. They also show very close effective indices to a regular slotted waveguides, which allows an easy launch of the segmented slotted mode, because the butt-coupling insertion loss between a normal slotted waveguide and a segmented slotted waveguide is found to be negligible. The segmentation leads extend for about 4 μm laterally in each direction from the central waveguide, which is sufficient to achieve optical isolation. In a high speed device, it is anticipated that constructing a transmission line with metal contacts standing off laterally by this distance from the center will not interfere with the optical propagation in the waveguide core.

Table 4.3. Segmented slotted waveguide designs with measured losses and estimated speed limits for 1 cm structures listed.

	Contact size (nm)	Contact periodicity (nm)	Measured loss achieved (dB/cm)	Intrinsic speed limit (GHz)
Design 1	40	200	-4.62 ± 0.11	60
Design 2	50	250	-4.00 ± 0.26	60

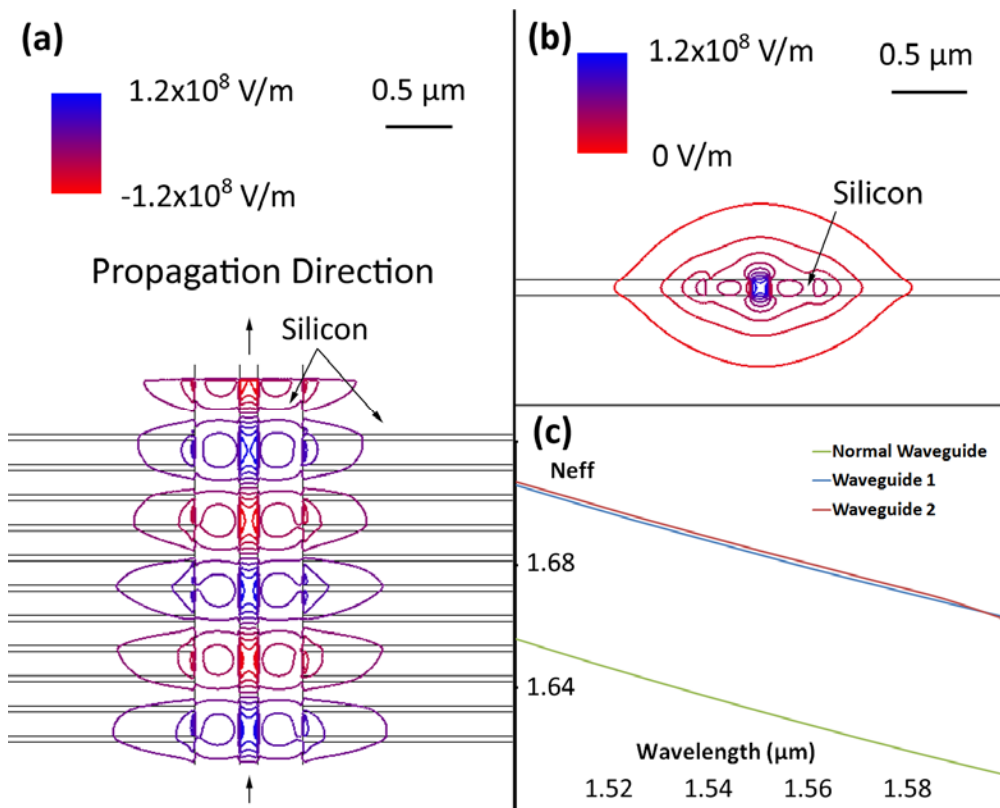


Figure 4.11. Panel (a) shows the propagation of a mode at 1550 nm in design 1, plotted in contours of 10% in E_x assuming 1 W of average power flow. Panel (b) shows the cross-sectional modal pattern in design 1, plotted with contours of 10% in $|E|$ assuming 1 W of average power flow. Panel (c) shows the dispersion curves of the two segmented slotted designs compared with a normal slotted design.

The fabrication procedure for these waveguides is similar to that used for other SOI devices described previously in this dissertation. Except in this case, since the structure is supported by oxide, a slightly thicker buried oxide layer (increased from 1.35 μm to 3 μm) proves to be very effective in improving propagation losses. Also, the lithography process is carefully calibrated with different electron beam dosages as shown in Figure 4.12. A large number of devices of different length and configurations are tested optically for transmission spectrum using the method described in Section 2.3. Devices consist of simple loops involving a varying length of segmented slotted waveguides, as well as various calibration structures for determining transition and coupling losses. The results turn out to be largely improved over the past segmented and even nonsegmented loss performance.

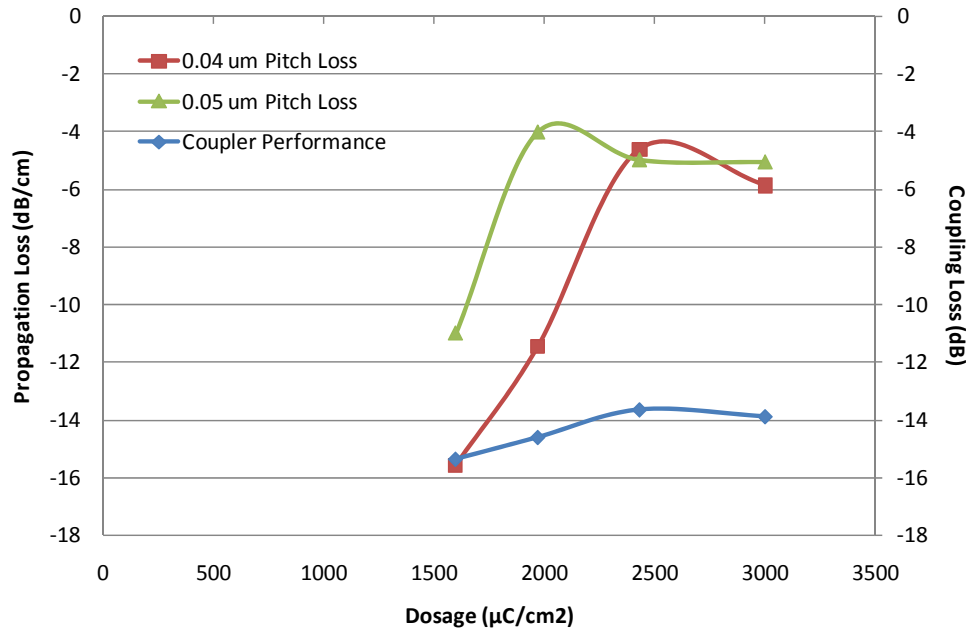


Figure 4.12. Variation of device and coupler performance (in dB/cm and dB) due to different electron beam dosages used during fabrication.

For each design and process variation, the devices are closely examined by cutting through the segmented cross section with the help of a focused ion beam system. In the left panel of Figure 4.13, we can see a 70 nm gap design failing due to suboptimal etching and resist conditions, hence exhibiting rough and slanted inner sidewalls that eventually close down to a V-shaped joint. In the right panel, one can see the outcome of an inappropriate lithography dosage, unnecessarily widening the gap and damaging the segmentation structure.

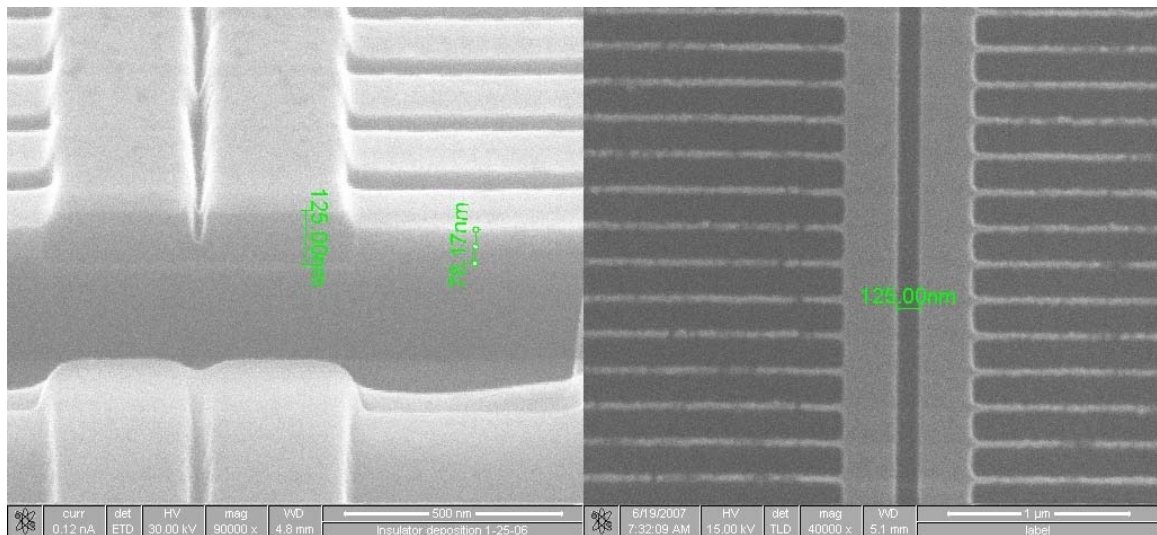


Figure 4.13. Failure modes of some segmented slotted designs and fabrication variations. The left panel shows a narrow 70 nm gap not fully etched through, and the right panel shows an overexposed sample with broken side leads.

Approximately 50 devices of each waveguide type were tested. Devices with segmented slotted waveguide lengths from 33 to 8000 μm were tested. The values reported in Table 4.3 and Figure 4.12 are determined by performing a linear regression on the results. The dominant loss mechanisms in this waveguide system are edge roughness and

surface state absorption [11]. Further development of the lithographic and etching processes, as well as surface treatments, can be expected to decrease the loss even further [11, 48]. Insertion losses from the normal slotted waveguides to the segmented and slotted waveguides were negligibly small. Figure 4.14 shows the typical normalized insertion loss for a number of devices. The difference between a simple loop and the segmented slotted devices includes the losses due to the mode conversion from normal ridge waveguides to slotted waveguides, which were measured to be approximately 2 dB per transition. More efficient ridge to slotted mode converters have recently been designed [49] that exhibit losses better than 0.25 dB, implying that this loss is not a fundamental limitation to a segmented and slotted waveguide based device. The curved frequency band is due to the bandwidth limitation of the couplers, and with the grating coupler input curve subtracted, the performance of our waveguides as a function of wavelength is relatively flat. The fine fringes that are visible come from two sources: first, return loss of the grating couplers, and second, the accumulation of loss from weak scatterers, which is visible as narrow loss peaks on the longer devices. SEM images shown in Figure 4.14 illustrate clearly defined nanoslots in well-fabricated devices with smoother sidewalls that also have much better vertical profile overall.

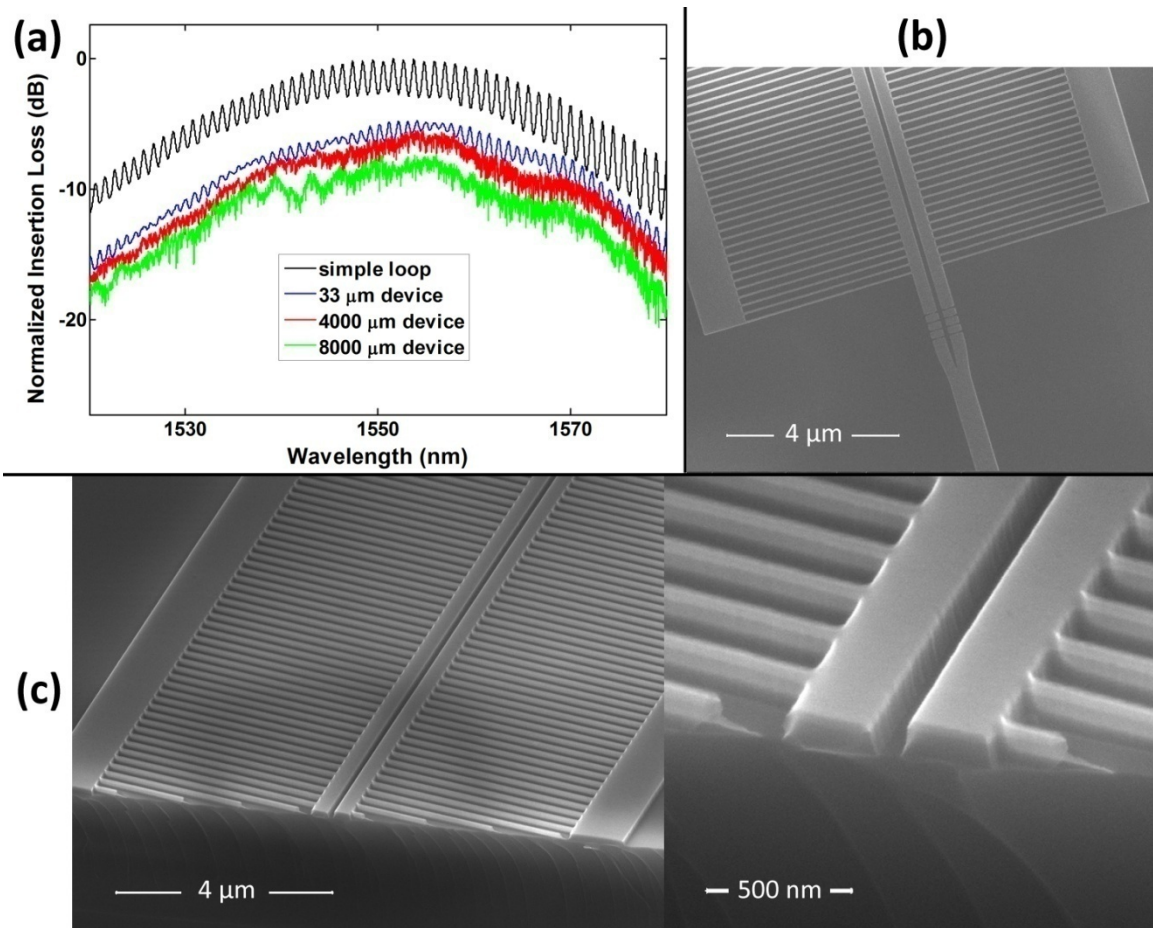


Figure 4.14. Panel (a) shows typical normalized insertion losses of segmented slotted waveguides in comparison with a short nonslotted loop. The longest device is 8000 μm , which corresponds to more than 30,000 contact pairs. Panels (b) and (c) are SEM micrographs of a segmented slotted waveguide from different angles.

Although it is likely that these waveguides will need to be coupled to transmission lines in practical devices (typical modulator lengths are on the order of millimeters to centimeters), it is possible to make some basic arguments about high-frequency performance for these waveguide geometries. Whatever the geometry of the driving RF transmission line, the unit-cell RC circuit implied in the segmented geometry must be

charged. The waveguides tested here are fabricated with SOI wafers that are slightly boron doped to 10^{15} atoms/cm³, with resistivity of 20 Ω -cm. Hypothetically, the devices can be doped with phosphorus in the same fashion as described in the previous chapter to achieve a resistivity of 0.04 Ω -cm, while introducing unacceptable optical loss. Then, we can calculate the charging time to be 2.7 ps for both designs 1 and 2 according to the simplified model illustrated in Figure 4.15 and Figure 4.16: this corresponds to a speed limit of around 60 GHz [50], as shown in Table 4.3. Though this is only an order-of-magnitude estimate, it provides a strong indication that these designs will be suitable for building devices at 10GHz and above. In this case, it is reasonable to anticipate that the additional optical losses introduced will be comparable to the loss increase seen in doping normal slotted waveguides [40], which is about -10 dB/cm.

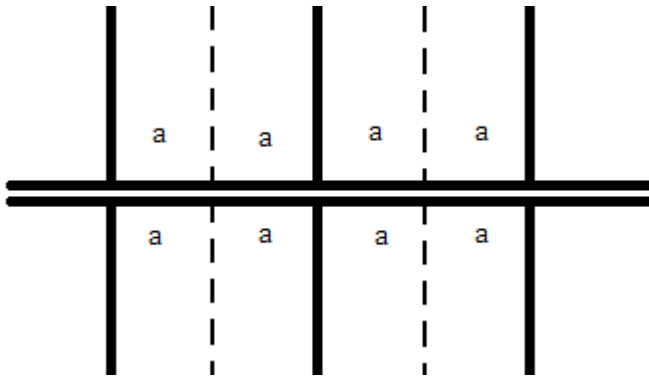


Figure 4.15. Simplified diagram of segmented slotted MZM signal arm geometry showing small parallel RC units.

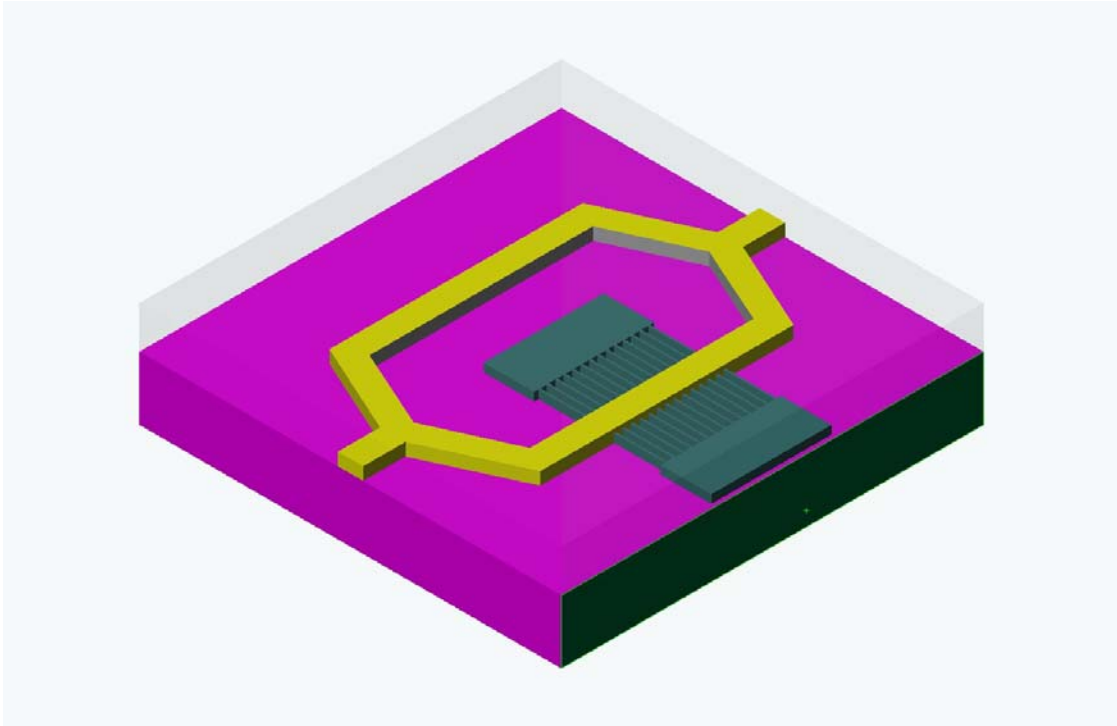


Figure 4.16. Diagram of a segmented slotted MZM in polymer-silicon hybrid implementation. The green metal pads are contacting the modulation arm at multiple points over a large span. Nanoslots and optical couplers are not shown for simplicity.

In addition to reducing the intrinsic turn-on time of a slotted structure, this segmented design also shows potential in improving its capability to pole and drive nonlinear polymer claddings. With the distributed electrode design, it is imaginable that the polymer deposited along the slot can be more uniformly poled and driven, and will suffer less from the inevitable series voltage roll-off associated with a single point contact design.

THIRD-ORDER NONLINEAR ALL-OPTICAL MODULATOR

5.1 Third-order Nonlinear Optics

As we have noted, in the fast developing history of modern communication system over the past few decades, optical components have taken up many important roles. However, the involvement of optics has by and large been limited to carrying signals across, while the majority of processing tasks are still performed by transistor-based electronics. For a while, this was a good working combination, but as the hunger for bandwidth kept increasing and electronics kept marching forward with Moore's scaling law, the cost and complexity of building high-speed low-latency electronic circuits quickly turn themselves into a hurdle. While improvements obtainable from software and system architecture optimization are receiving more and more attention, alternatives at physical level, such as the use of optics, are also back in play for functions like interconnects, basic signal processing, and potentially optical logic [51]. In fact, the exploration of optics as more active system components has been of interest even from the early days of modern communication evolution [52], but the lack of economic demand and appropriate integrated platform has largely limited its development. Particularly, when nonlinearity is needed to realize some functionality, it becomes more difficult, since the nonlinear properties of many materials are either relatively weak or slow.

With the ascent of silicon photonics and the advancement of compatible nonlinear media such as polymer materials, it has become conceivable to build compact nonlinear

devices aimed for practical use. In the previous two chapters, we have shown multiple devices and applications based on second-order parametric interaction that serve to interface between the electrical and optical domains. Now, given the ultrafast nature of the nonlinear polymers in use, there is little reason to doubt that nonlinear effects can also be induced by optical signals, electromagnetic waves of very high frequencies essentially. By writing out more terms in equation (4.1), we obtain equation (5.1) below showing a third-order nonlinear term χ^3 , which quantifies index of refraction changes that scale with electric field strength quadratically.

$$D = \epsilon_0 E (\epsilon_r + \chi^2 E + \chi^3 E^2 \dots) \quad (5.1)$$

Optical waves fall into the category that can utilize this third-order nonlinearity effect, since they consist of oscillating electric field with fast switching orientations. The third-order nonlinearity is small in silicon itself (reported to have a Kerr coefficient of $4 \times 10^{-18} \text{ m}^2/\text{W}$, roughly equal to a χ^3 of $4 \times 10^{-21} \text{ m}^2/\text{V}^2$ [53-56]), but it is possible to specially engineer nonlinear polymers to demonstrate enhanced third-order nonlinear properties [57, 58]. We have previously seen from Figure 2.3 that a simple silicon ridge waveguide is capable of confining optical mode and hence significantly enhancing the corresponding electric field intensity. As noted earlier, in a typical single mode waveguide design with dimensions of 500 nm in width and 100 nm in height, about one-third of the mode energy resides in the top cladding region, allowing more interaction with possible nonlinear claddings as shown in Figure 5.1 panel C.

5.2 Four-wave Mixing

To test out the third-order nonlinear properties of the proposed nonlinear polymer clad silicon ridge waveguides, a straightforward experiment can be performed to demonstrate FWM (four-wave mixing). Four-wave mixing is essentially an interaction process between light waves of four different frequencies in a third-order nonlinear medium, satisfying frequency and phase matching conditions. In our waveguides particularly, where dispersion is small in the vicinity of 1550 nm, inputting two signals of reasonably high power at wavelength ω_1 and ω_2 could potentially create observable signals at $2\omega_1 - \omega_2$ and $2\omega_2 - \omega_1$, basically two evenly spaced side peaks. The particular device under tests is a long run-out waveguide about 7 mm in length, coated and measured with various polymers for both optical loss and nonlinearity characteristics. Seed signals of two closely spaced wavelengths are separately generated and fed through a fiber coupled 50/50 beam splitter before being amplified by a Keopsys EDFA to about 0.65 W. In the best case, 1% conversion efficiency is achieved, corresponding to an effective χ^3 of $1 \times 10^{-20} \text{ m}^2/\text{V}^2$, with a decent waveguide loss performance of better than -6 dB/cm , among which less than -1 dB/cm is caused by polymer clad loss. The χ^3 exhibited by the polymer is about three times larger than that of silicon itself.

5.3 Ultrafast All-optical Modulator

Given that the third order nonlinearity is significant enough in a hybrid silicon polymer structure, the natural following step is to build an intensity modulator. In this case, since the goal is to demonstrate ultrafast nonlinearity in the optical domain, a broadband traveling wave scheme has to be adopted. The ring resonator approach used previously is not suitable here due to its narrow band and thermally sensitive nature. Here, a three-port Mach-Zehnder device is proposed, whose logic and layout is shown in Figure 5.1. A source signal is fed into the device and divided into two waveguide arms through a 3 dB directional coupler junction. A high power gate signal is fed into the device and couples into the signal arm of the device also through another 3 dB coupler. For the sake of maintaining power balance between the two arms, the reference arm also contains an additional 3 dB coupler, but no merging signal. Suppose the gate signal is intensity modulated as shown in Figure 5.1 panel A, it will induce effective index changes in the signal waveguide arm, and hence creating a corresponding phase modulation to the branch of source signal that propagates in the same arm. When the two branches merge back together near the output drain port, the phase modulation effect is turned into an intensity modulation of the source signal by superposition.

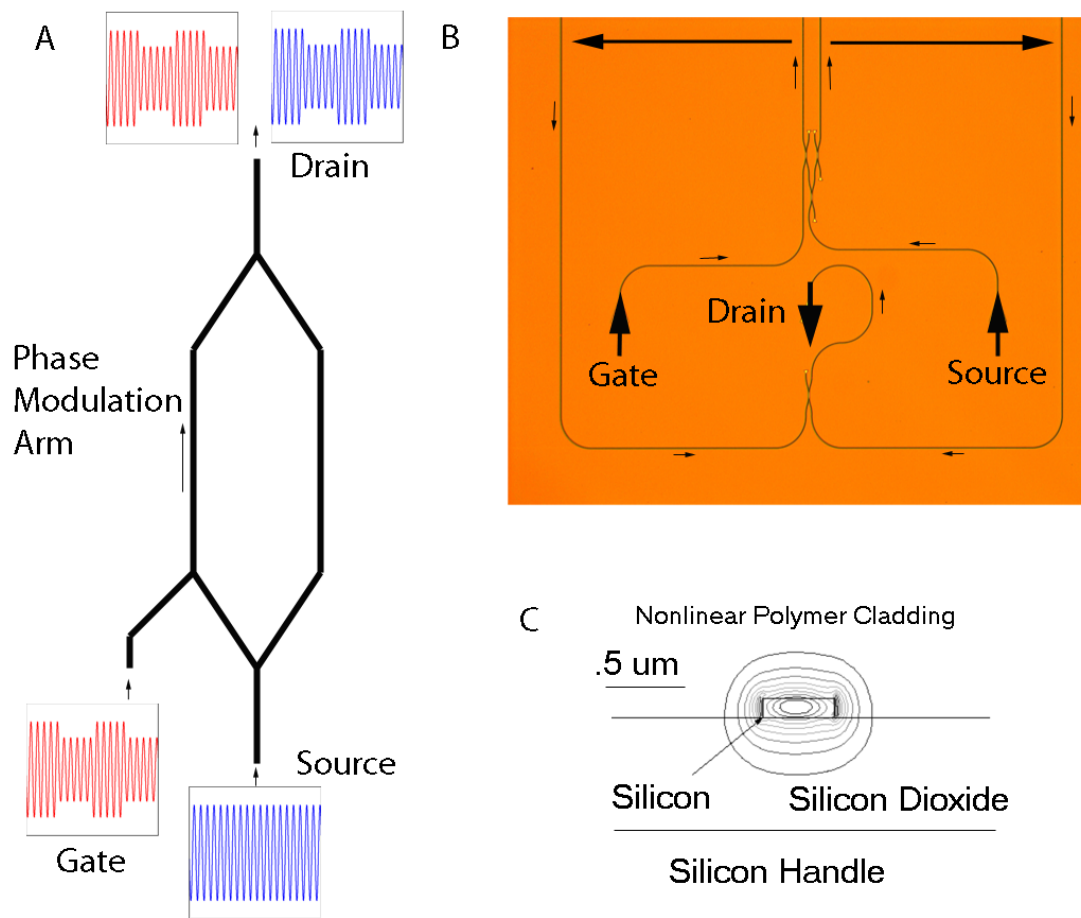


Figure 5.1. Panel A shows the operating diagram of a traveling wave MZM that introduces phase shifting in the signal path by the Kerr effect. Panel B shows a microscope photo of the actual device overlaid with port and flow labels. Panel C shows the mode pattern of polymer clad silicon waveguides used in 10% power contours.

The large chip area taken up by the long run-out waveguides can be improved by using spooled waveguide layout instead, made possible by the tight bend radius due to high optical confinement of our waveguide. A typical Mach-Zehnder device with greater than 1cm run-outs can easily be fit into a 0.5×0.5 mm chip estate, as shown in Figure 5.2.

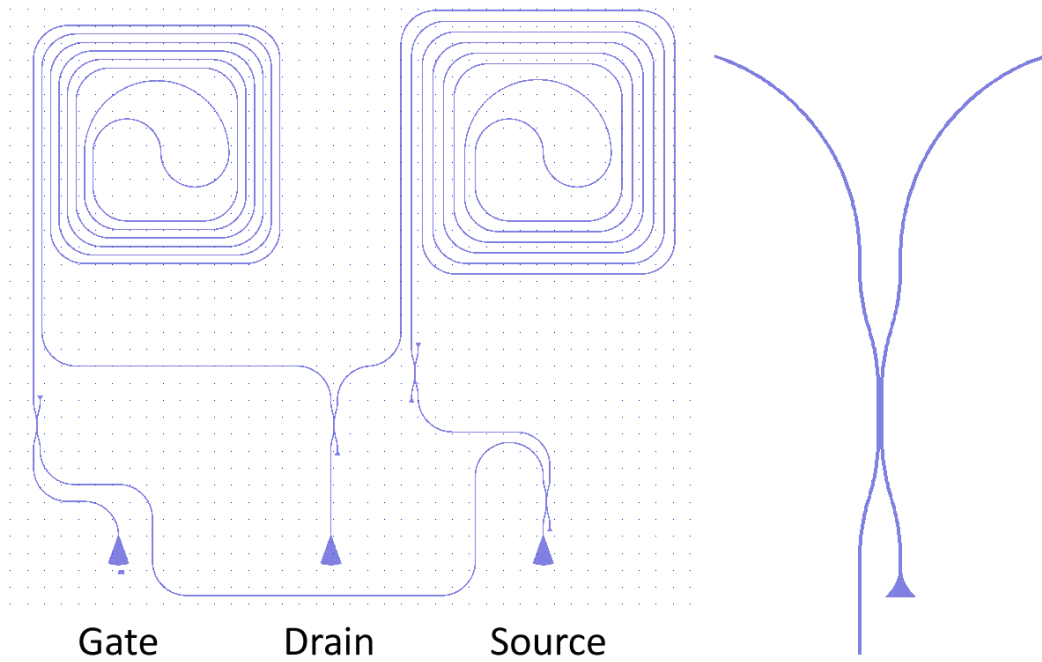


Figure 5.2. The left panel shows a typical spooled waveguide MZM, and the right panel shows an enlarged view of a 50/50 directional coupler.

The Mach-Zehnder device here is fabricated in a similar fashion as other SOI devices so far introduced in this dissertation, and the top polymer cladding is also spin coated and properly baked. The optical path lengths for the two arms are 1.2 and 1.24 cm respectively. This unbalanced design is done on purpose, so that the intrinsic phase shifts change for different wavelengths, and a desired operating point of intrinsic shift can be chosen at will during measurements. The resulting unmodulated transmission spectrum is shown in Figure 5.3 with repeating peaks and troughs.

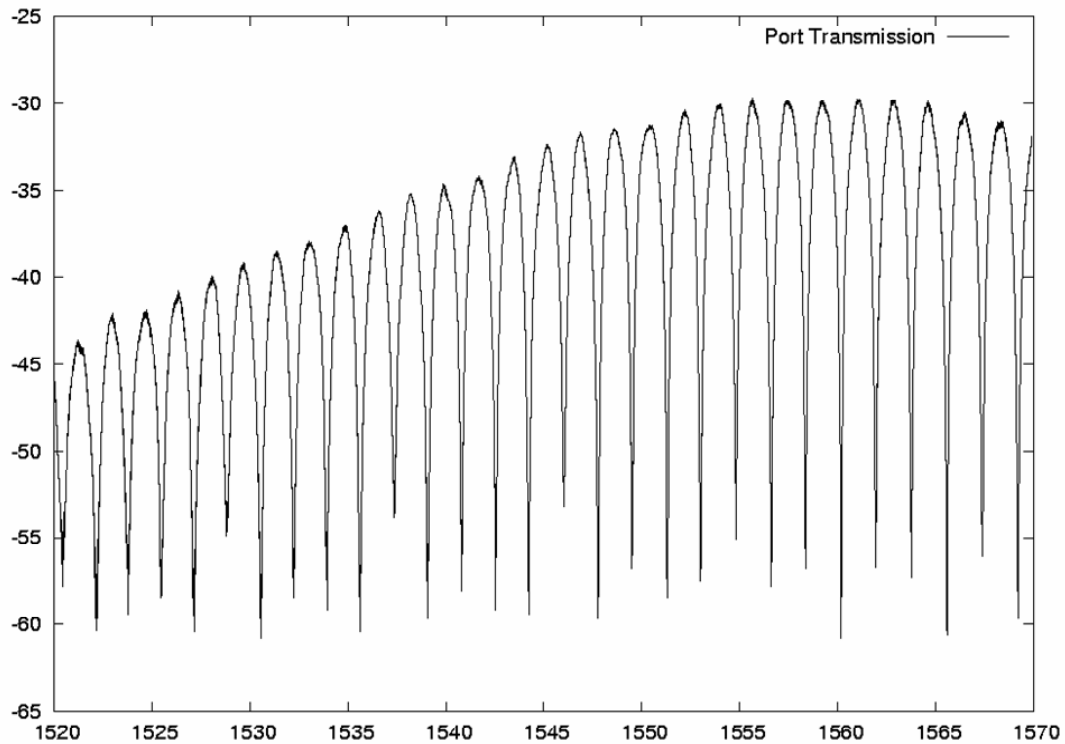


Figure 5.3. Transmission spectrum of a typical unbalanced Mach-Zehnder interferometer characterized by intrinsic phase shifts that vary with wavelength.

5.4 Testing and Data of All-optical Modulator

To verify and measure the intensity modulation process, two sets of experiments are performed. The most straightforward method is to send in a modulated gate signal together with an unmodulated source signal, and to observe the modulation on the source wavelength at the output drain port. The logical layout of this test setup is illustrated in Figure 5.4 below. After a standard initial optical screening of the devices to determine optical loss performance, a diode laser is used to generate a CW (continuous wave) seed

source signal, which is subsequently amplified by a polarization-maintaining EDFA from Calmar Optcom (Sunnyvale, CA) before being coupled into the source port of our device. An Agilent 8703B optical component analyzer is used to generate an RF modulated gate signal, which is amplified by a Keopsys EDFA and fed into the gate port through a polarization controller. The Agilent unit used is essentially a microwave VNA (vector network analyzer) equipped with an optical module for optical signal generation and measurement. The output of the Mach-Zehnder device from the drain port goes through a Newport Lambda Commander 9500C programmable C-band spectral filter (Newport Corporation, Irvine, CA) that can provide better than 30 dB out-of-band extinction. This step prevents the gate signal from reaching the final detection equipment, which is the optical input for the Agilent unit, a 20 GHz bandwidth photodiode. The Agilent optical component analyzer is specialized in measuring intensity modulation transfer from one electrical/optical port of a device to another. The measurement result reported is an optical S parameter in the unit of dBo (optical decibel), defined in equation (5.2), where $I(t)$ is the optical intensity measured by the photodetector, and N is the offset that would give a direct input-to-output through measurement 0 dB reading.

$$S(f) = 10 \log \left(\left| \int_0^T \exp(i2\pi ft) I(t) dt \right| \right) + N \quad (5.2)$$

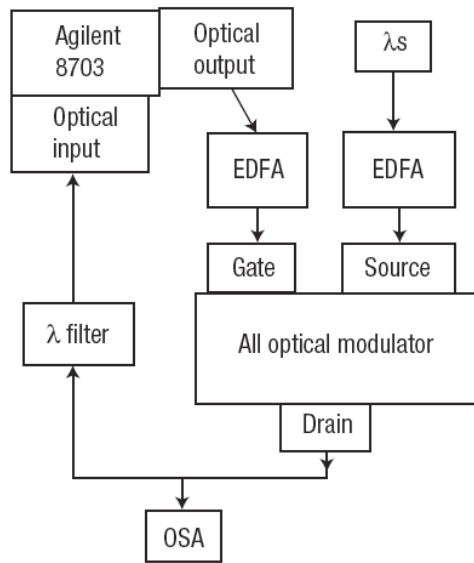


Figure 5.4. Logical diagram of the gigahertz modulation experiment.

Note that the drain output is also measured with an Anritsu OSA (optical spectrum analyzer) to show the modulation side peaks in the frequency domain as in panel B and C of Figure 5.5. However, it is the S parameter measurements shown in panel A that presents conclusive evidence of intensity modulation. Multiple control experiments were also performed, including turning gate or source signals off, coating the device with linear cladding material, and substituting with a device that only has a phase modulation arm without the Mach-Zehnder interferometer geometry. As we can see from Figure 5.5, a positive measurement produces optical S parameters that are 5 dB above noise floor and asymptotically approaches -37 dB. The stronger response at low frequencies is probably due to higher polymer χ^3 for these frequencies. Turning off source signals ensures that no measurable gate signal is leaking through the wavelength filter, and the fact that linear

polymer cladding also does not produce observable response rules out some other possibilities such as thermal and free carrier effects.

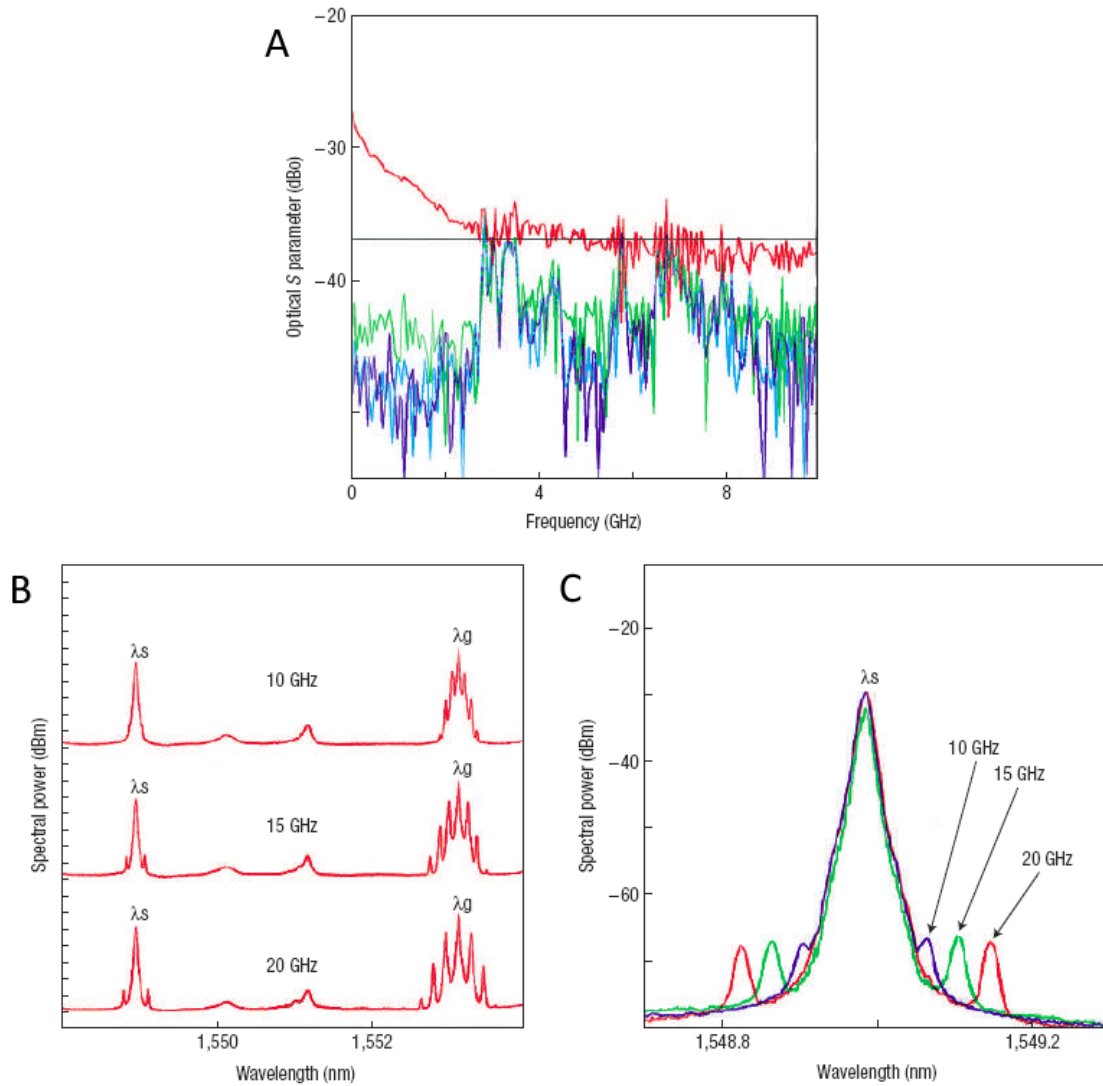


Figure 5.5. Panel A shows positive and negative results of measuring optical modulation transfer with optical S parameters. Panel B and C show the spectral contents of modulator outputs at various gigahertz-range modulation frequencies.

Even though one would wish to verify the performance of the system at higher speed into terahertz regime by simply running the above experiment with elevated modulation speed, there is no straightforward way to generate the required terahertz gate signal or to readily detect the output signal with a photodiode that has such a fast response. Therefore, an indirect experiment needs to be used to observe such modulation in the frequency domain, as illustrated in Figure 5.6. In this case, the gate signal comprises of sources of two closely spaced wavelengths, which result in a beating pattern with a relatively slower terahertz varying envelope. The rest of the setup is similar to the gigahertz experiment, and the output is routed directly to an OSA.

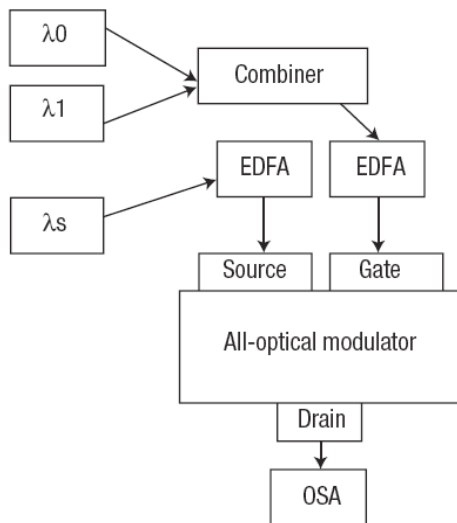


Figure 5.6. Logical diagram of the terahertz modulation experiment.

In Figure 5.7 below, the spectral measurements from three sets of experiment are shown with the two gate lasers spaced at 2.6, 0.6, and 0.25 THz respectively. In each case, difference frequency modulation side peaks are seen around the source signal, showing that the four-wave mixing process at terahertz speed is indeed occurring in these devices as

expected. Since our Mach-Zehnder device is intrinsically unbalanced, it is possible to vary the source wavelength to see different power throughput at the drain port. Note that in panel C of the figure, three different source frequencies with output power levels varying by more than 10 dBm are used. Had the side peaks been produced by pure four-wave mixing only, one would expect the side peaks to vary in height. However, the resulting modulation peaks are roughly of the *same* height, which is a distinct sign of proof that phase modulation is being converted to an amplitude modulation by the Mach-Zehnder structure employed. The same set of experiment is carried out from 60 GHz to 2.4 THz to produce the three-dimensional color graph as shown in Figure 5.8. The actual implementation of these tests is also limited by the bandwidth of fiber amplifiers as well as the on-chip grating couplers used, while it is estimated that the system can operate at an even higher speed beyond the maximum of 2.6 THz tested, until the phase mismatch due to waveguide dispersion starts to become a hurdle.

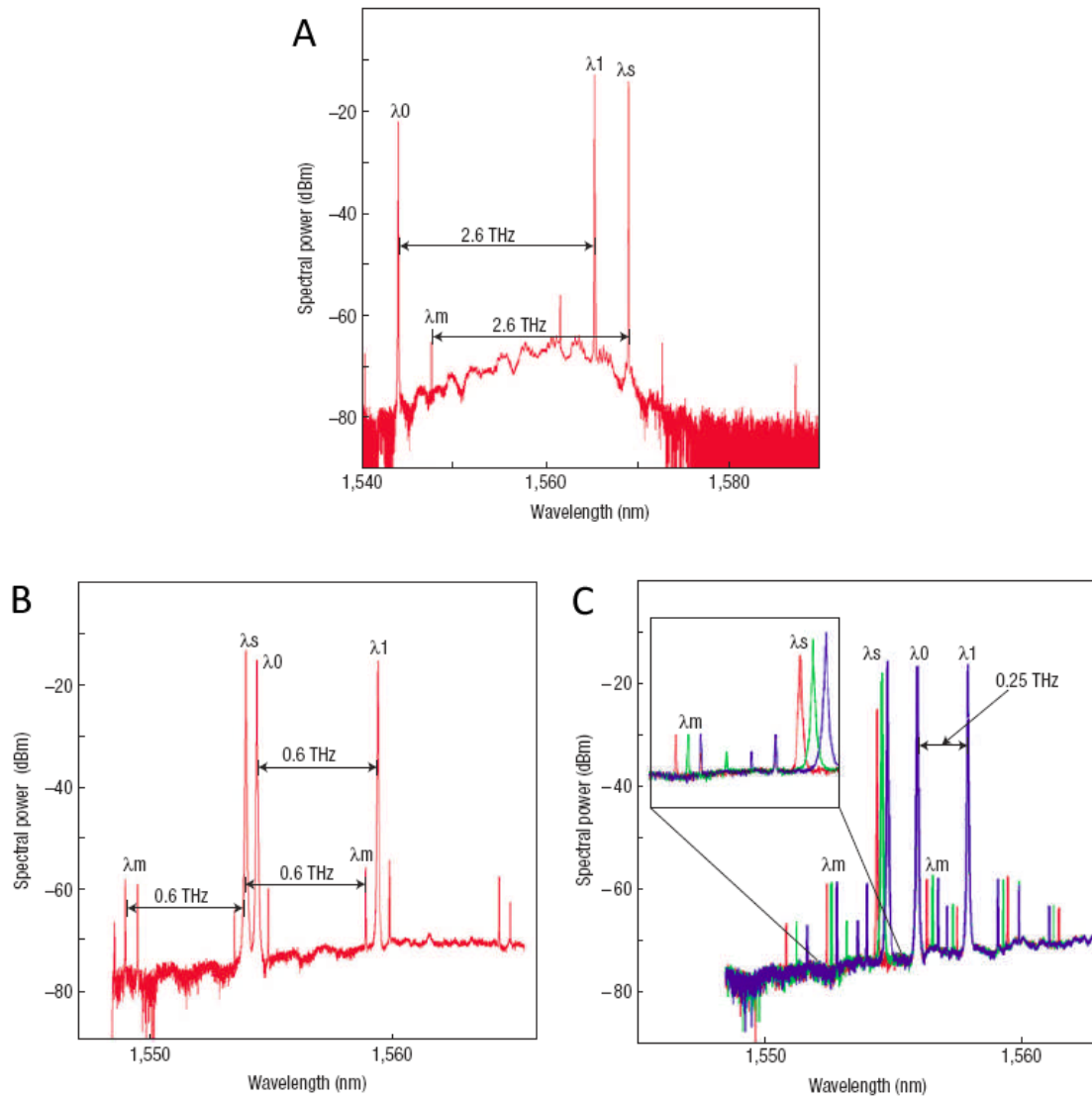


Figure 5.7. Panel A and B show the spectral contents of modulator outputs when it is driven by 2.6 and 0.6 THz difference frequency inputs. Panel C shows the output spectrums of the modulator driven by a 0.25 THz difference frequency input and three different source frequencies. The resulting modulation peaks maintain a constant level.

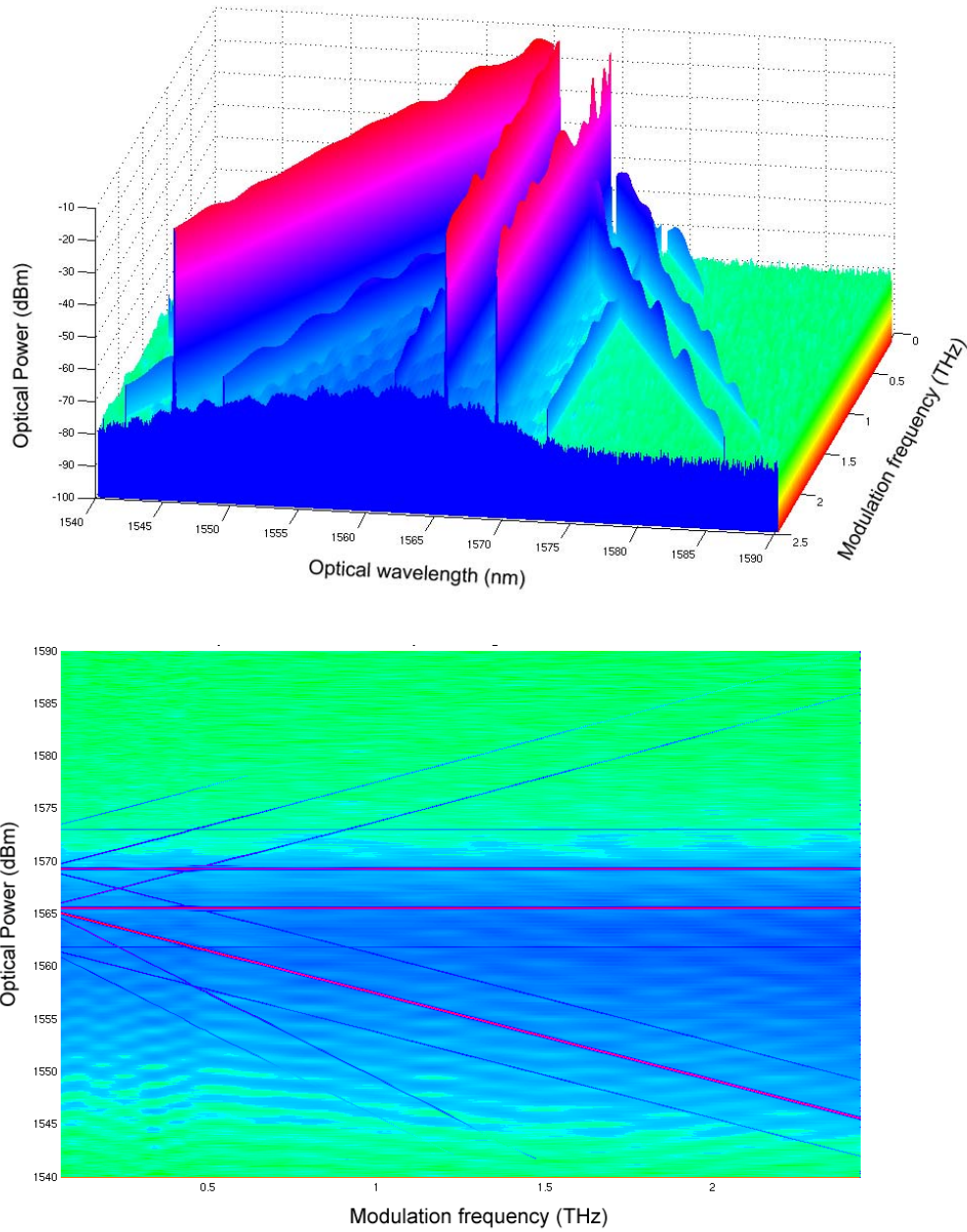


Figure 5.8. Top-down and three-dimensional diagrams illustrating the operation of an all-optical modulator at speeds from 60 GHz to 2.4 THz. The slight ripples and falloffs at high frequencies are due to efficiency changes in fiber amplifiers and couplers.

It can be shown, as detailed in [59], that the power ratio of four-wave mixing pumping signals vs. generated peaks can be expressed in terms of χ^3 . The effect of these gate signals on phase shifting the source signal on the nonlinear arm of our device can be approximated as the relationship in equation (5.3) below, where fr is the power ratio mentioned above.

$$\Delta\phi = 4\sqrt{fr} \quad (5.3)$$

For a typical ratio of -40 dB and with 14 dBm of actual gate power in the nonlinear segment of our device, a 0.04 radian of phase shifting is expected. This corresponds to a modulation extinction of 0.3 dB only, although it would be possible operate in a high-loss high-extinction region with 3 dB of extinction and 24 dB of insertion loss on this unbalanced MZM, had there been enough dynamic range. The optical S parameter and χ^3 implied are in close agreement with the gigahertz experiments and the four-wave mixing results described previously.

This set of experiments and results represents the effort of demonstrating all-optical nonlinear phenomena in miniaturized solid state devices and has shown promise by revealing a potential platform for developing more sophisticated building blocks that can be used in optical communication, logic, and computing.

BIBLIOGRAPHY

- [1] M. Lipson, "Guiding, modulating, and emitting light on silicon - Challenges and opportunities," *Journal of Lightwave Technology*, vol. 23, pp. 4222-4238, 2005.
- [2] H. Rong, R. Jones, A. Liu, O. Cohen, D. Hak, A. Fang, and M. Paniccia, "A continuous-wave Raman silicon laser," *Nature*, vol. 433, pp. 725-728, 2005.
- [3] A. Liu, R. Jones, L. Liao, D. Samara-Rubio, D. Rubin, O. Cohen, R. Nicolaescu, and M. Paniccia, "A high-speed silicon optical modulator based on a metal-oxide-semiconductor capacitor," *Nature*, vol. 427, pp. 615-618, 2004.
- [4] Luxtera.com, <http://www.luxtera.com/about-us.html>.
- [5] M. Paniccia and S. Koehl, "The silicon solution," *IEEE Spectrum*, vol. 10, 2005.
- [6] P. Rabiei, W. H. Steier, C. Zhang, and L. R. Dalton, "Polymer micro-ring filters and modulators," *Journal of Lightwave Technology*, vol. 20, pp. 1968-1975, 2002.
- [7] Lumerica.com, <http://www.lumerica.com/>.
- [8] R. Hull, "Properties of crystalline silicon," *Inspec emis Datareview Series*, vol. 20, 1999.
- [9] IBM, "IBM advances chip technology with breakthrough for making faster, more efficient semiconductors," *IBM press release*, 1998.
- [10] T. Baehr-Jones, M. Hochberg, C. Walker, and A. Scherer, "High-Q ring resonators in thin silicon-on-insulator," *Applied Physics Letters*, vol. 85, pp. 3346-3347, 2004.
- [11] M. Borselli, "High-Q microresonators as lasing elements for silicon photonics," Ph. D. dissertation, Caltech, 2006.

- [12] A. Yariv, "Universal relations for coupling of optical power between microresonators and dielectric waveguides," *Electronics Letters*, vol. 36, pp. 321-322, 2000.
- [13] A. Yariv, "Critical coupling and its control in optical waveguide-ring resonator systems," *IEEE Photonics Technology Letters*, vol. 14, pp. 483-485, 2002.
- [14] I. Moerman, P. P. Van Daele, and P. M. Demeester, "A review on fabrication technologies for the monolithic integration of tapers with III-V semiconductor devices," *IEEE Journal of Selected Topics in Quantum Electronics*, vol. 3, pp. 1308-1320, 1998.
- [15] V. R. Almeida, R. R. Panepucci, and M. Lipson, "Nanotaper for compact mode conversion," *Optics Letters*, vol. 28, pp. 1302-1304, 2003.
- [16] A. Mekis, A. Dodabalapur, R. E. Slusher, and J. D. Joannopoulos, "Two-dimensional photonic crystal couplers for unidirectional light output," *Optics Letters*, vol. 25, pp. 942-944, 2000.
- [17] T. W. Ang, G. T. Reed, A. Vonsovici, A. G. R. Evans, P. R. Routley, and M. R. Josey, "Effects of grating heights on highly efficient unibond SOI waveguide grating couplers," *IEEE Photonics Technology Letters*, vol. 12, pp. 59-61, 2000.
- [18] D. Taillaert, W. Bogaerts, P. Bienstman, T. F. Krauss, P. Van Daele, I. Moerman, S. Verstuyft, K. De Mesel, and R. Baets, "An out-of-plane grating coupler for efficient butt-coupling between compact planar waveguides and single-mode fibers," *IEEE Journal of Quantum Electronics*, vol. 38, pp. 949-955, 2002.

- [19] N. Eriksson, M. Hagberg, and A. Larsson, "Highly directional grating outcouplers with tailorable radiation characteristics," *IEEE Journal of Quantum Electronics*, vol. 32, pp. 1038-1047, 1996.
- [20] B. E. A. Saleh and M. C. Teich, "Fundamentals of Photonics," *Wiley*, 2007.
- [21] M. N. O. Sadiku, "Elements of Electromagnetics," *Oxford University Press*, 2001.
- [22] Y. R. Shen, "The Principles of Nonlinear Optics," *John Wiley & Sons*, 2003.
- [23] M. Dagenais, R. F. Leheny, and J. Crow, "Integrated Optoelectronics," *Academic Press*, 1995.
- [24] N. Bloembergen, P. S. Pershan, and L. R. Wilcox, "Microwave modulation of light in paramagnetic crystals," *Physical Review Letters*, vol. 120, pp. 2014-2023, 1960.
- [25] M. Hochberg, T. Baehr-Jones, G. Wang, J. Huang, P. Sullivan, L. Dalton, and A. Scherer, "Towards a millivolt optical modulator with nano-slot waveguides," *Optics Express*, vol. 15, pp. 8401-8410, 2007.
- [26] M. M. d. Lima, M. Beck, R. Hey, and P. V. Santos, "Compact Mach-Zehnder acousto-optic modulator," *Applied Physics Letters*, vol. 89, p. 3, 2006.
- [27] H. Fukano, T. Yamanaka, M. Tamura, and Y. Kondo, "Very-low-driving-voltage electroabsorption modulators operating at 40 Gb/s," *Journal of Lightwave Technology*, vol. 24, pp. 2219-2224, 2006.
- [28] M. T. Tinker and J. B. Lee, "Thermal and optical simulation of a photonic crystal light modulator based on the thermo-optic shift of the cut-off frequency," *Optics Express*, vol. 13, pp. 7174-7188, 2005.
- [29] R. A. Soref and B. R. Bennett, "Electrooptical effects in silicon," *IEEE Journal of Quantum Electronics*, vol. 23, pp. 123-129, 1987.

- [30] Q. Xu, B. Schmidt, S. Pradhan, and M. Lipson, "Micrometre-scale silicon electro-optic modulator," *Nature*, vol. 435, pp. 325-327, 2005.
- [31] A. Yariv, "Quantum Electronics (third edition)," *John Wiley & Sons*, 1989.
- [32] E. L. Wooten, K. M. Kissa, A. Yi-Yan, E. J. Murphy, D. A. Lafaw, P. F. Hallemeier, D. Maack, D. V. Attanasio, D. J. Fritz, G. J. McBrien, and D. E. Bossi, "A review of lithium niobate modulators for fiber-optic communications systems," *IEEE Journal of Selected Topics in Quantum Electronics*, vol. 6, pp. 69-82, 2000.
- [33] H. Ma, S. Liu, S. Suresh, L. Liu, S. Kang, M. Haller, T. Sassa, L. Dalton, and A. Jen, "Highly efficient and thermally stable electro-optical dendrimers for photonics," *Advanced Functional Materials*, vol. 12, pp. 565-574, 2002.
- [34] T. Kim, J. D. Luo, J. W. Kang, M. Haller, Y. Tian, L. Dalton, and A. Jen, "Molecular engineering of highly efficient and thermally stable nonlinear optical polymers for electro-optics," *Abstracts of Papers of the American Chemical Society*, vol. 228, p. U438, 2004.
- [35] H. Ma and A. K.-Y. Jen, "Functional Dendrimers for Nonlinear Optics," *Advanced Materials*, vol. 13, p. 1201, 2001.
- [36] Y. Enami, C. T. Derose, D. Mathine, C. Loychik, C. Greenlee, R. A. Norwood, R. D. Kim, J. Luo, Y. Tian, A. K. Y. Jen, and N. Peyghambarian, "Hybrid polymer/sol-gel waveguide modulators with exceptionally large electro-optic coefficients," *Nature Photonics*, vol. 6, pp. 180-185, 2007.
- [37] H. Tazawa, Y.-H. Kuo, I. Dunayevskiy, J. Luo, A. K.-Y. Jen, H. R. Fetterman, and W. H. Steier, "Ring resonator-based electrooptic polymer traveling-wave modulator," *Journal of Lightwave Technology*, vol. 24, pp. 3514-3519, 2006.

- [38] Q. Xu, V. Almeida, R. Panepucci, and M. Lipson, "Guiding and confining light in void nanostructures," *Optics Letters*, vol. 29, pp. 1209-1211, 2004.
- [39] Q. Xu, V. Almeida, R. Panepucci, and M. Lipson, "Experimental demonstration of guiding and confining light in nanometer-size low-refractive-index material," *Optics Letters*, vol. 29, pp. 1626-1628, 2004.
- [40] T. Baehr-Jones, M. Hochberg, G. Wang, R. Lawson, Y. Liao, P. A. Sullivan, L. Dalton, A. K.-Y. Jen, and A. Scherer, "Optical modulation and detection in slotted silicon waveguides," *Optics Express*, vol. 13, pp. 5216-5226, 2005.
- [41] C. Zhang, L. R. Dalton, M. C. Oh, H. Zhang, and W. H. Steier, "Low V- π electrooptic modulators from CLD-1: Chromophore design and synthesis, material processing, and characterization," *Chemistry of Materials*, vol. 13, pp. 3043-3050, 2001.
- [42] S. Graf, H. Sigg, and W. Bachtold, "High-frequency electrical pulse generation using optical rectification in bulk GaAs," *Applied Physics Letters*, vol. 76, pp. 2647-2649, 2000.
- [43] B. Bortnik, Y. Hung, H. Tazawa, B. J. Seo, J. D. Luo, A. K.-Y. Jen, W. H. Steier, and H. R. Fetterman, "Electrooptic polymer ring resonator modulation up to 165 GHz," *IEEE Journal of Selected Topics in Quantum Electronics*, vol. 13, pp. 104-110, 2007.
- [44] M. Hochberg, T. Baehr-Jones, C. Walker, J. Witzens, L. C. Gunn, and A. Scherer, "Segmented waveguides in thin silicon-on-insulator," *Journal of the Optical Society of America. B, Optical Physics*, vol. 22, pp. 1493-1497, 2005.

- [45] T. Baehr-Jones, M. Hochberg, C. Walker, and A. Scherer, "High-Q optical resonators in silicon-on-insulator-based slot waveguides," *Applied Physics Letters*, vol. 86, p. 081101, 2005.
- [46] M. Corp., "PMMA Resists," <http://www.microchem.com/products/pmma.htm>, 2007.
- [47] Y.-G. Zhao, W.-K. Lu, Y. Ma, S.-S. Kim, S. T. Ho, and T. J. Marks, "Polymer waveguides useful over a very wide wavelength range from the ultraviolet to infrared," *Applied Physics Letters*, vol. 77, pp. 2961-2963, 2000.
- [48] K. K. Lee, D. R. Lim, L. C. Kimerling, J. Shin, and F. Cerrina, "Fabrication of ultralow-loss Si/SiO₂ waveguides by roughness reduction," *Optics Letters*, vol. 26, pp. 1888-1890, 2001.
- [49] N.-N. Feng, R. Sun, L. C. Kimerling, and J. Michel, "Lossless strip-to-slot waveguide transformer," *Optics Letters*, vol. 32, pp. 1250-1252, 2007.
- [50] G. Wang, T. Baehr-Jones, M. Hochberg, and A. Scherer, "Design and fabrication of segmented, slotted waveguides for electro-optic modulation," *Applied Physics Letters*, vol. 91, p. 143109, 2007.
- [51] A. F. J. Levi, "Optical interconnects in systems," *Proceedings of the IEEE*, vol. 88, pp. 750-757, 2000.
- [52] G. I. Stegeman, E. M. Wright, N. Finlayson, R. Zanoni, and C. T. Seaton, "Third order nonlinear integrated optics," *Journal of Lightwave Technology*, vol. 6, pp. 953-970, 1988.
- [53] H. K. Tsang, C. S. Wong, T. K. Liang, I. E. Day, S. W. Roberts, A. Harpin, J. Drake, and M. Asghari, "Optical dispersion, two-photon absorption and self-phase

- modulation in silicon waveguides at 1.5 μm wavelength,” *Applied Physics Letters*, vol. 80, pp. 416-418, 2002.
- [54] M. Dinu, F. Quochi, and H. Garcia, “Third-order nonlinearities in silicon at telecom wavelengths,” *Applied Physics Letters*, vol. 82, pp. 2954-2956, 2003.
- [55] A. Yariv and P. Yeh, “Photonics: Optical Electronics in Modern Communications (sixth edition),” *Oxford University Press*, 2007.
- [56] T. Suhara and M. Fujimura, “Waveguide Nonlinear-Optic Devices,” *Springer Verlag*, 2003.
- [57] S. R. Marder, W. E. Torruellas, M. Blanchard-Desce, V. Ricci, G. I. Stegeman, S. Gilmour, J.-L. Brédas, J. Li, G. U. Bublitz, and S. G. Boxer, “Large molecular third-order optical nonlinearities in polarized carotenoids,” *Science*, vol. 276, pp. 1233-1236, 1997.
- [58] L. Brozozowski and E. H. Sargent, “Azobenzenes for photonic network applications: Third-order nonlinear optical properties,” *Journal of Materials Science: Materials in Electronics*, vol. 12, pp. 483-489, 2001.
- [59] M. Hochberg, T. Baehr-Jones, G. Wang, M. Shearn, K. Harvard, J. Luo, B. Chen, Z. Shi, R. Lawson, P. Sullivan, A. K. Y. Jen, L. Dalton, and A. Scherer, “Terahertz all-optical modulation in a silicon-polymer hybrid system,” *Nature Materials*, vol. 5, pp. 703-709, 2006.